High-power fiber-laser-pumped picosecond nonlinear optical sources from the near- to mid-infrared

Shahrzad Parsa

Universitat Politecnica de Catalunya,

Castelldefels, May 2018

Doctorate Program: Photonics

Duration: 2014-2018

Thesis advisor: Prof. Majid Ebrahim-Zadeh

Thesis co-advisor: Dr. Suddapalli Chaitanya Kumar

Thesis submitted in partial fulfillment of the requirements for the degree

of

Doctor of Philosophy of the Universitat Politecnica de Catalunya

May 2018

Dedicated to my loving parents, my brother,

and

my wonderful husband

Success should always call for showing greater kindness,

generosity and justice;

only people lost in the darkness treat it as

an occasion for greater greed.

-Cyrus the great (King of Persia, 600-530 BC)

Declaration

I hereby declare that the matter embodied in the thesis entitled, “High-power fiber-laser-pumped picosecond nonlinear optical sources from the near- to mid-infrared” is the result of investigations carried out by me at ICFO-The Institute of Photonic Sciences, Castelldefels, Barcelona, Spain under the supervision of Prof. Majid Ebrahim-Zadeh and Dr. Suddapalli Chaitanya Kumar, and that it has not been submitted elsewhere for the award of any degree or diploma.

In keeping with the general practice in reporting scientific observations, due acknowledgment has been made whenever the work described is based on the findings of other investigators.

_____

Shahrzad Parsa

Certificate

I hereby certify that the matter embodied in this thesis entitled, “High-power fiber-laser-pumped picosecond nonlinear optical sources from the near- to mid-infrared” has been carried out by Mrs. Shahrzad Parsa at ICFO-The Institute of Photonic Sciences, Castelldefels, Barcelona, Spain, under my supervision, and that it has not been submitted elsewhere for the award of any degree or diploma.

_____

Prof. Dr. Majid Ebrahim-Zadeh
(ICFO, Research Supervisor)

Dr. Suddapalli Chaitanya Kumar
(ICFO, Research Co-Supervisor)

Acknowledgements

First of all, I would like to express my gratitude to Prof. Majid Ebrahim-Zadeh, for providing me the opportunity to come to ICFO and to pursue my PhD studies in his group. Also, I thank Dr. Suddapalli Chaitanya Kumar, my co-advisor, who was actually more than a co-advisor, for all he did for me, helping me in the lab, giving new ideas and lightening up the path. I am so thankful of both of them to make me sure and more determined about what I really want to do and about what I really want to be in the future.

I would like to thank Kavita, my senior and my officemate. I started my PhD working with her in the lab which helped me to get to know the lab, the environment and their goals better.

I appreciate the presence of my colleagues/friends- Anuja, Jun, Callum, Hanyu, Sukeert, Ramaiah, Enrique, Tess and Biblop. I am so thankful to Pep, my very good friend, for being so kind and always ready to listen, and also for his generous help to translate the abstract of the thesis into Spanish.

I am so happy of having more nice friends who listen to me, share their experiences, encourage me and cheer me up- Maryam (Shahrokhvand), Zahra (Raissi), Mrs. Naderi (Prof. Dr, a very nice person), Zohreh (Khosravi), Fatemeh (Sammak), Kavitha (KKG), Rafael (Sibilio), Marja (my Dutch Granny), my anti-tanti-khale Marjan, and many others including M.Sc., and college friends for leaving me nice memories of the past.

I want to express my gratitude to Prof. Lluis Torner, director of ICFO-The Institute of Photonic Sciences, and his management team, for financial support during my PhD, and for making ICFO such a nice place.

I would also like to thank different units at ICFO such as administration, KTT, mechanical, electronic, IT and logistics for their help and organized coordination.

I am grateful to all my teachers and professors at the school and University for teaching me and sharing their experiences and knowledge. I would like to express my sincere gratitude to my supervisors during my master studies, Prof. Dr. Mahmood Soltanolkotabi

and Prof. Dr. Hamid-Reza Fallah, and my thesis advisor, Mr. Mohsen Ramezani, for their encouragement, trust and support which led me to the right path.

My everlasting gratitude goes to my family, my always caring, supportive and understanding parents, my mother Tahmineh and my father Morteza. I really don't know how to thank them, I am so thankful to them beyond words. Whatever I do, how much I try, I cannot really repay their inseparable and unconditional love and kindness for sure. I am more than grateful for having them in my life. I am more than grateful for their presence, for brightening my world, for everything and everything. I am so thankful for having my bright, clever, so talented and kind brother, my Shaheen jan. I am elder to him, but I have learnt a lot from him. I am so appreciative of my lovely dadashi jan for showing me how to be strong, hopeful and happy.

When I came to ICFO, I was so motivated, energetic and ambitious. During these four years here, many things have happened to me, some good and some not that nice, and many things have changed for me. But if I could travel in time, I wouldn't change anything, even a single one, for I believe what happened to me made the way for me to meet meinen wundervollen Mann, meinen Udo jan. Words fail me when I want to express my feeling towards him and to say how happy, how proud and how grateful I am for having him in my life. I am so and so thankful to him for being always with me, always ready to help me, always supporting me in every aspects and always encouraging me for moving forward. I am so thankful to him, my bright sun, for making my life warmer, grüner, brighter and more vernal. I would be eternally thankful to my parents-in-law, Dr. Udo Wilhelm Weigel and Mrs. Edith Irmgard Weigel for bringing up such a wonderful person.

And…

for having all these, for everything, I am so thankful to my God. Who gave me life, who never forsakes me, and who always takes care of me. Who gifted me such a wonderful family, my four beloved angels. I appreciate the presence of my God in my life, who helps me to be happy, to live in peace, and to be able of being so grateful.

Thank you God for giving me such a nice feeling, which I will not trade with the whole world.

Abstract

Ultrafast picosecond coherent sources in the near-to-mid-infrared (IR) spectral range are of great interest for a variety of applications such as pump-probe spectroscopy, remote sensing, photobiology and novel upconversion imaging techniques. Nonlinear optics, and in particular nonlinear frequency conversion techniques, offer an efficient and effective approach towards the realization of sources emitting such radiation, as nowadays, nonlinear frequency conversion technologies are recognised to be viable and reliable sources of laser radiation with broad wavelength tunability and power scalability, without the need of cryogenic cooling.

In this thesis, we have demonstrated high-power, high-repetition-rate picosecond sources based on nonlinear frequency conversion processes through optical parametric oscillators (OPOs) and difference-frequency-generation (DFG), in order to cover the near- to mid-IR wavelength region.

We have developed a stable, high-repetition-rate picosecond rapidly tunable OPO based on fan-out designed grating periods in PPKTP nonlinear crystal. The OPO is synchronously pumped by a mode-locked frequency-doubled Yb-fiber laser in the green at 532 nm, and can provide stable and high-power radiation which is rapidly tunable from 749-962 nm in the signal and from 1189-1838 nm in the idler, at room temperature.

Further, we have demonstrated what we believe to be the first tunable high-repetition-rate picosecond source based on OP-GaP crystal in the mid-IR. Using a single-pass DFG between a mode-locked Yb-fiber laser at 1064 nm and the tunable output from a picosecond MgO:sPPLT OPO synchronously pumped by the same laser, the source generated continuous tunable radiation across 3040-3132 nm in the mid-IR at the repetition rate of ~80 MHz, in good beam quality.

Additionally, we have also presented the first high-power, high-beam-quality, idler-resonant picosecond OPO based on a multi-grating MgO:PPLN crystal tunable across 2100-4000 nm in the mid-IR. The OPO provided as much as 3.5 W of mid-IR radiation with M^2 values to be better than 1.8 in both horizontal and vertical directions.

Resumen

Las fuentes coherentes de picosegundos ultrarrápidos en el rango espectral de infrarrojo cercano a infrarrojo medio (IR) son de gran interés para una amplia variedad de aplicaciones tales como pump-probe espectroscopia, la teledetección, la fotobiología y las nuevas técnicas de upconversion imaging. La óptica no lineal, y en particular las técnicas de conversión de frecuencia no lineal, ofrecen un enfoque eficiente y eficaz para la realización de fuentes que emiten tales radiaciones, ya que hoy en día, las fuentes basadas en la conversión de frecuencia no lineal son fuentes viables y fiables de emisión de radiaciones láser con amplia sintonía de longitud de onda y escalabilidad de potencia, sin necesidad de refrigeración criogénica.

En esta tesis, hemos demostrado fuentes de picosegundos de alta potencia y alta tasa de repetición basadas en procesos de conversión de frecuencia no lineales a través de osciladores ópticos paramétricos (OPO) y generación de frecuencias de diferencia (DFG) para cubrir la región de longitud de onda de IR cercano a IR medio del espectro electromagnético.

Hemos desarrollado una fuente de picosegundos estable, de alta tasa de repetición, rápidamente sintonizable, basado en un cristal PPKTP con períodos de rejilla diseñados en forma de abanico. El OPO, es bombeado sincrónicamente por un mode-locked láser de fibra de Yb, doblado en frecuencia para generar verde a 532 nm, que proporciona radiación estable y de alta potencia rápidamente sintonizable de 749-962 nm en el signal y de 1189-1838 nm en el idler, a temperatura ambiente.

Además, hemos demostrado lo que creemos que es la primera fuente de picosegundos sintonizable con alta tasa de repetición basada en el cristal OP-GaP en el IR medio. Usando una DFG de un solo *paso* entre un mode-locked láser de fibra de Yb a 1064 nm y la salida ajustable de un OPO de picosegundo basado en un cristal de MgO:sPPLT bombeado sincrónicamente por el mismo láser, la fuente generó radiación sintonizable de 3040-3132 nm en el medio-IR a la velocidad de repetición de ~80 MHz, con buena calidad de haz.

Además, también presentamos el primer OPO de picosegundos de alta potencia y buena calidad de haz, con resonancia del idler, basado en un cristal MgO:PPLN de rejilla múltiple sintonizable a lo largo de 2100-4000 nm en el IR medio. El OPO proporcionó hasta 3.5 W de radiación de IR medio con valores de M^2 mejores que 1.8 tanto en dirección horizontal como vertical.

Publications

Journal publications

1. S. Chaitanya Kumar, J. Canals Casals, **S. Parsa**, K. T. Zawilski, P. G. Schunemann, M. Ebrahim-Zadeh, "Yb-fiber-pumped mid-infrared picosecond optical parametric oscillator tunable across 6.2-6.7 μm," Appl. Phys. B-Lasers Opt. **124**, 100 (2018)

2. **S. Parsa**, S. Chaitanya Kumar, M. Ebrahim-Zadeh, "Picosecond idler-resonant mid-infrared optical parametric oscillator based on MgO:PPLN," Opt. Lett. (2018)-*In preparation.*

3. J. Canals Casals[†], **S. Parsa**[†], S. Chaitanya Kumar, K. Devi, P. G. Schunemann, M. Ebrahim-Zadeh, "Picosecond difference-frequency-generation in orientation-patterned gallium phosphide," Opt. Exp. **25**(16), 19595-19602 (2017).

   [†]Equal contribution.

4. S. Chaitanya Kumar, **S. Parsa**, and M. Ebrahim-Zadeh, "Fiber-laser-based, green-pumped, picosecond optical parametric oscillator using fan-out grating PPKTP," Opt. Lett. **41**(1), 52-55 (2016).

5. K. Devi, **S. Parsa**, M. Ebrahim-Zadeh, "Continuous-wave, single-pass, single-frequency second-harmonic-generation at 266 nm based on birefringent-multicrystal scheme," Opt. Exp. **24**(8), 8763-8775 (2016).

Conference and proceeding publications

1. **S. Parsa**, S. Chaitanya Kumar, K. Devi, M. Ebrahim-Zadeh, "High-Power, High-Beam-Quality, Idler-Resonant Mid-Infrared Picosecond Optical Parametric Oscillator," Mid-Infrared Coherent Sources, MICS'2018, Strasbourg, France, March 2018. Paper: MW2C.6

2. S. Chaitanya Kumar, J. Canals Casals, **S. Parsa**, K. T. Zawilski, P. G. Schunemann, M. Ebrahim-Zadeh, "Optimally Output-coupled, Deep-Infrared picosecond Optical Parametric Oscillator based on $CdSiP_2$," Mid-Infrared Coherent Sources, MICS'2018, Strasbourg, France, March 2018. Paper: MW1C.6

3. S. Chaitanya Kumar, J. Canals Casals, **S. Parsa**, K. T. Zawilski, P. G. Schunemann, M. Ebrahim-Zadeh, "High-repetition-rate picosecond deep-infrared optical parametric oscillator based on $CdSiP_2$" CLEO, San Jose, United States, May 2017. Paper: SM4M.4

4. J. Canals Casals, **S. Parsa**, S. Chaitanya Kumar, K. Devi, P. G. Schunemann, M. Ebrahim-Zadeh, "Mid-infrared picosecond difference-frequency-generation in orientation-patterned gallium phosphide" CLEO, San Jose, United States, May 2017. Paper: SW4M.2

5. S. Chaitanya Kumar, J. Canals Casals, **S. Parsa**, K. T. Zawilski, P. G. Schunemann, M. Ebrahim-Zadeh, "Yb-fiber-pumped high-repetition-rate picosecond deep-infrared optical parametric oscillator," CLEO/Europe-EQEC, Munich, Germany, June 2017. Paper: CD-P.27

6. S. Chaitanya Kumar, **S. Parsa**, M. Ebrahim-Zadeh, "Yb-fiber-green-pumped, widely tunable, room-temperature picosecond optical parametric

oscillator based on fan-out PPKTP," CLEO/Europe-EQEC, Munich, Germany, June 2017. Paper: CD-P.28

7. K, Devi, **S. Parsa**, M. Ebrahim-Zadeh, "Birefringent-multicrystal, single-pass, continuous-wave second-harmonic-generation in deep-ultraviolet," Proc. SPIE **9894**, 98940R (2016).

8. K, Devi, **S Parsa**, M. Ebrahim-Zadeh, "Stable, continuous-wave, birefringent-multicrystal, single-frequency deep-UV generation," CLEO, San Jose, USA, June 2016. Paper: JTu5A.62

9. S. Chaitanya Kumar, **S Parsa**, M. Ebrahim-Zadeh, "High-repetition-rate, green-pumped, picosecond optical parametric oscillator based on fan-out PPKTP," CLEO, San Jose, USA, June 2016. Paper: JTu5A.55

High-power fiber-laser-pumped picosecond nonlinear optical sources from the near- to mid-infrared

Contents

List of Figures

List of Tables

Chapter 1

Introduction

Laser, invented in 1960, is a source of coherent light based on population inversion and stimulated emission [1]. The extracted beam has unique properties. It is unidirectional, has high power and high intensity, and it is coherent in time and in space [2,3]. Having these properties, laser plays an important and undeniable role in science, technology and in people's daily life [4-6]. There are many practical applications such as spectroscopy, photochemistry and optical communication demanding high-power coherent beams with high beam quality and broad wavelength tunability [7]. However, the development of tunable lasers has been challenging since the laser transition in conventional lasers occurs between discrete energy states in the laser media resulting in a narrow linewidth output beam [8]. A tunable laser can be realized by using a laser medium with broadened energy levels [8,9], but still many regions of the electromagnetic spectrum, especially in the ultraviolet (UV), visible, near- to mid-infrared (IR) and terahertz (THz), remain inaccessible to lasers due to the unavailability of the suitable gain media. Figure 1.1 shows the wavelength coverage of some tunable lasers. While almost all the available laser sources are confined to wavelengths below 3 μm, the most practical and widely established laser with a tuning range of ~650-1100 nm is the Kerr-lens mode-locked Ti:sapphire laser, which is the workhorse of the near-IR region [10-12].

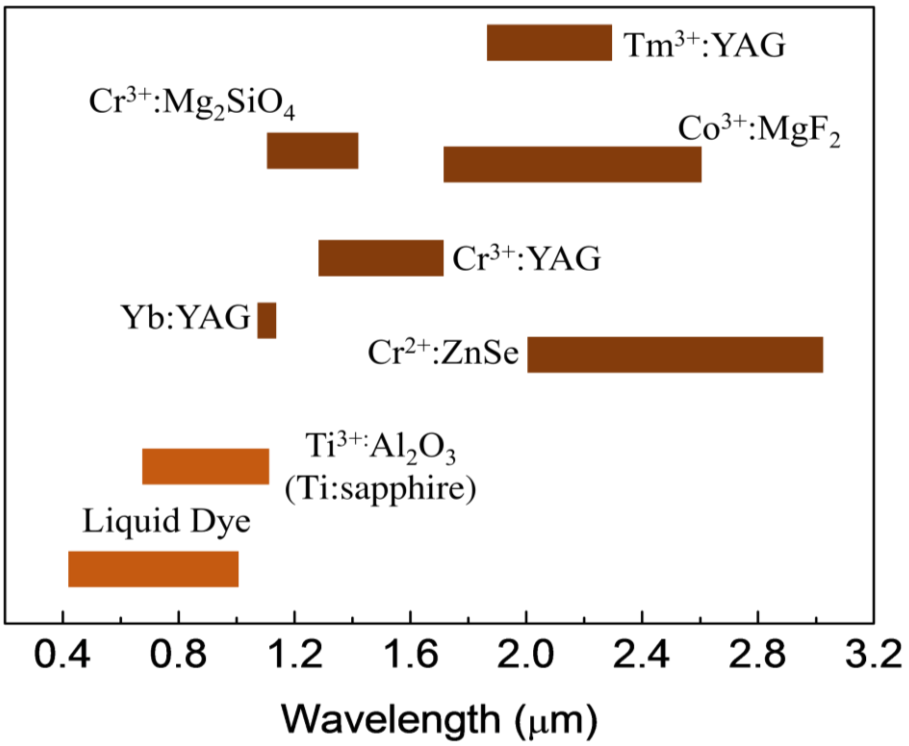

Fig. 1.1. Spectral coverage of conventional tunable lasers.

Nonlinear optics, and in particular frequency conversion processes, opened up new routes towards building novel sources emitting widely tunable coherent laser radiation in new spectral region and different temporal domains, from continuous-wave (cw) to ultrafast femtosecond time-scale. The coherent emission, which is obtained often from a single device, offers the same properties as the conventional laser sources. It also provides new capabilities, which are of great interest for a variety of applications such as spectroscopy, remote sensing and bioimaging [13,14].

The earliest observations of optical nonlinearity go back to more than three decades before the invention of the laser, by Kerr [15] and later by Raman [16], and the term *nonlinear optics* was introduced into optics in 1943 by E. Schrödinger as the study of the nonlinear response of materials to optical fields [17,18]. However, the realization of this nonlinear response to the incoming electromagnetic field requires very strong intensity, and so the real observation of coherent nonlinear optical effect happened only after the invention of laser when Franken reported the second-harmonic-generation (SHG) of

Ruby laser at 347.2 nm in the quartz crystal [19]. The investigations on the nonlinear optical processes have been proceeded by the first observation of sum-frequency-generation (SFG) by Bass in 1962 in triglycine sulfate [20].

In all the mentioned reports, the processes showed low conversion efficiency. In order to realize efficient nonlinear optical processes, *phase-matching* condition or the conservation of momentum needs to be satisfied, which means that a proper phase relationship should be maintained between the interacting beams along the propagation direction, as it was proposed separately by Giordmaine and Maker in 1962 [21,22]. However, the concept of phase-matching was proposed even before the invention of laser, in 1958 by Tien in the context of radio waves [23,24]. With the phase-matching condition satisfied, in 1963, Smith and Braslau reported the first demonstration of difference-frequency-generation (DFG) in KD_2PO_4 (KDP) [25]. Soon after, the theoretical studies on the nonlinear optical processes [26-28] bolded the importance of optical parametric generation (OPG) and amplification (OPA) as an important technique for the generation of tunable coherent radiation, and paved the way of realizing the first optical parametric oscillator (OPO) by Giordmaine and Miller in 1965 [29]. The reported OPO was tunable across 970 nm to 1150 nm and used the second-harmonic of Nd^{+3}:$CaWO_4$ laser at 532 nm, as pump source, and a 54-mm-long $LiNbO_3$ (LN) as a nonlinear optical crystal. A few years later, in 1968, the first cw OPO was demonstrated independently by Smith and Byer [30,31].

In an OPO, there are three waves interacting with each other. Conventionally, the incoming laser beam, which triggers a process, is called the *pump*, the generated beam with shorter wavelength is called the *signal* and that with longer wavelength is called the *idler*. An OPO can be setup in different cavity configurations and can provide oscillation for one, two, or for all the three interacting beams, accordingly, the system is named as a *singly-resonant oscillator* (SRO), *doubly-resonant oscillator* (DRO) or *triply-resonant oscillator* (TRO) [32]. These OPO configurations will be described in more detail in Chapter 2.

With the development of new nonlinear optical materials and laser pump sources offering improved spectral and spatial coherence, together with the major advancements in design innovation, pulsed OPOs enjoyed a long-waited renaissance over about 20 years [33-36]. Nowadays, there are numerous pulsed OPOs covering the spectral regions from the mid-IR [7,13] to the visible [37], and further down to the UV [38], by using appropriate nonlinear crystals such as LiB_3O_5 (LBO), β-BaB_2O_4 (BBO) and BiB_3O_6 (BIBO). However, studies and investigations on developing devices based on nonlinear optical processes to provide more efficient coherent sources with high and stable output power and good beam quality are still ongoing.

The research presented in this thesis deals with coherent pulsed sources based on DFG and OPOs in SRO configuration, which can cover the spectral region from near- to mid-IR. The approach of the research presented in this thesis is shown in Fig. 1.2. The fundamental pump source in all the presented experiments is an ytterbium (Yb)-fiber laser at 1064 nm with a pulse duration of ~20 ps at the repetition rate of ~80 MHz.

I. In the first experiment, we used an LBO nonlinear optical crystal to generate the second harmonic of the 1064 nm pump laser in order to be served as a pump source for a periodically-poled $KTiOPO_4$ (PPKTP)-based OPO to extract rapidly tunable near-IR wavelengths at room temperature.

II. In the second experiment, we generated tunable mid-infrared wavelengths from a new nonlinear optical crystal, orientation-patterned GaP (OP-GaP). We mixed the pump source at 1064 nm with the signal wavelengths in the near-IR extracted from a MgO-doped stoichiometric periodically-poled $LiTaO_3$ (MgO:sPPLT) OPO synchronously pumped by the same laser thorough a single-pass DFG process.

III. In the third experiment, we built up broadly tunable coherent radiation in the mid-IR with good beam quality, by building a 1064-nm-pumped idler-resonant OPO based on MgO-doped periodically-poled $LiNbO_3$ (MgO:PPLN) crystal.

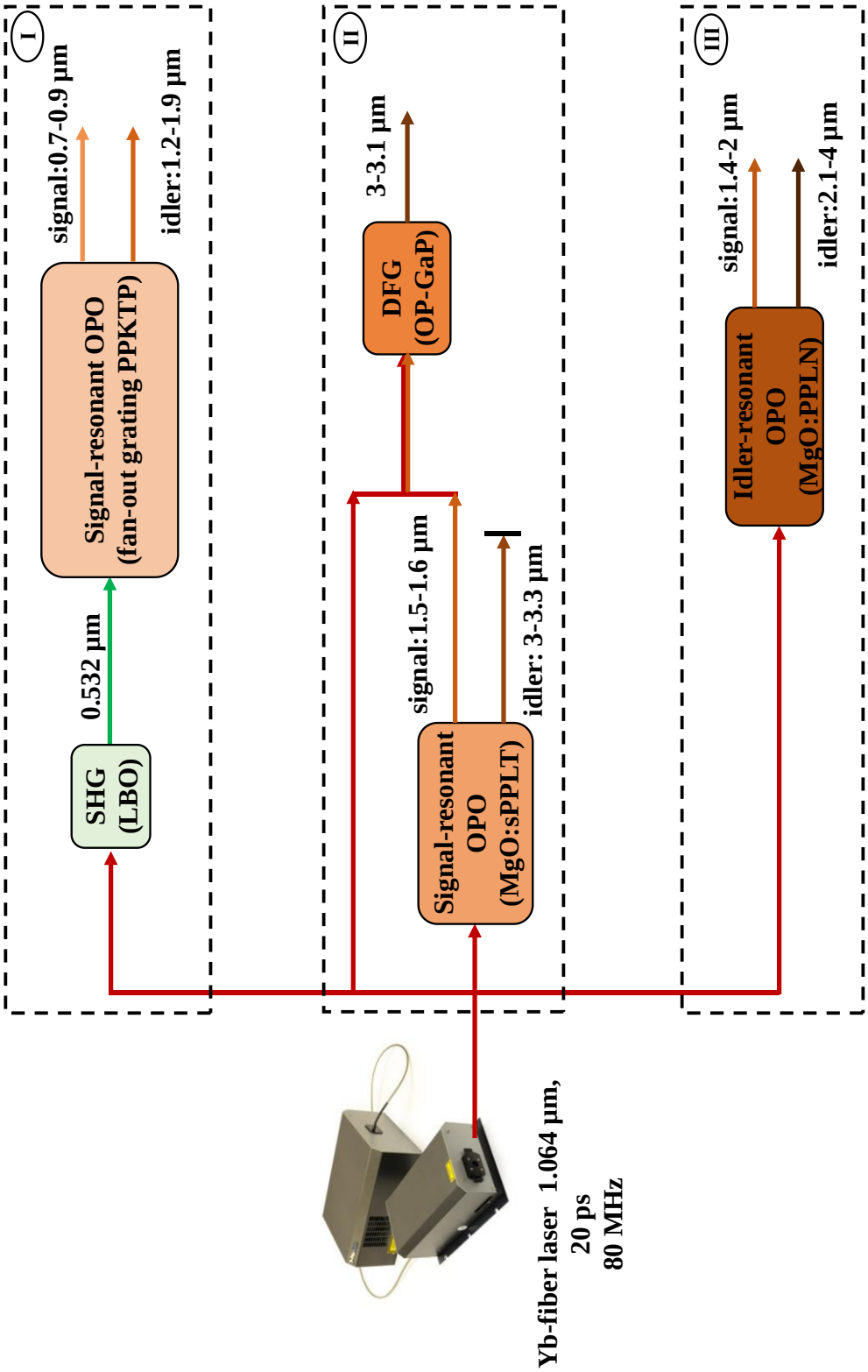

Fig 1.2. Approach of the thesis research work.

The thesis presented here is organized into 6 chapters.

In Chapter 2, we will introduce briefly the basics of nonlinear optics and various nonlinear optical phenomena including SHG, SFG, DFG and OPO. Since the successful operation of an OPO requires observing some design criteria, in the same chapter we will discuss those conditions together with the tuning capabilities of the OPO.

In Chapter 3, we present our experimental results on the first green-pumped, picosecond, high-repetition-rate OPO based on a PPKTP nonlinear crystal. The fan-out grating design for the crystal gives the possibility of tuning the extracted wavelengths rapidly while operating at room temperature. The results of power scaling, power stability and wavelength tuning properties are presented together with our studies on the optical absorption and optical behaviour of the nonlinear optical crystal when it is pumped by high-repetition-rate picosecond green beam.

In Chapter 4, we introduce a new nonlinear optical crystal, OP-GaP, and describe what we believe to be the first tunable high-repetition-rate picosecond mid-IR source based on single-pass DFG in OP-GaP by mixing a mode-locked Yb-fiber laser at 1064 nm and the tunable signal outputs from a picosecond MgO:sPPLT OPO, synchronously pumped by the same laser, in a 40-mm-long OP-GaP crystal with a single grating period of Λ=16 μm. The results of power scaling, power stability and wavelength tuning properties are also presented in the same chapter.

In Chapter 5, we present our experimental investigation on what believe to be the first picosecond idler-resonant OPO based on an MgO:PPLN crystal. The source is synchronously pumped by the Yb-fiber laser at 1064 nm and generates high-power mid-IR wavelengths with good beam quality. Our theoretical and experimental studies on the cavity-length detuning of the source are described in detail in this chapter together with our experimental results on power scaling, power stability and beam quality of the idler-resonant OPO.

In Chapter 6, we conclude the thesis with the future outlook.

References

1. T. H. Maiman, "Stimulated optical radiation in Ruby," Nature 187, 493-494 (1960).
2. A. E. Siegman, "Lasers," (University Science Books, 1986).
3. O. Svelto, "Principles of lasers," (Springer, Science+Business Media, 2010).
4. J. Wilson, J. F. B. Hawkes, "Lasers: Principles and Applications," (Prentice Hall, 1987).
5. L. Berthe, D. Courapied, S. El karnighi, P. Peyre, C. Gorny, Y. Rouchausse, "Study of laser interaction in water flow confinement at high-repetition-rate," J. Laser Appl. 29, 0420061-0420067 (2017).
6. W. Y. Khoder, R. Sroka, "Concept of a fiber guidance instrument for laser-assisted laparoscopic partial nephrectomy," Med. Laser Appl. 26, 176-182 (2011).
7. M. Ebrahim-Zadeh, I. T. Sorokina, "Mid-Infrared coherent sources and applications," (Springer, 2007).
8. W. Koechner, "Solid state lasers engineering," (Springer, Science+Business Media, Inc. 2006).
9. C. L. Tang, L. K. Cheng, "Fundamentals of optical parametric processes and oscillators in Laser science and technology series," (Vol-10, Harwood academic publishers, 1995).
10. D. E. Spence, P. N. Kean, W. Sibbett, "60-fsec pulse generation from a self-mode-locked Ti:sapphire laser," Opt. Lett. 16, 42-44 (1991).
11. M. T. Asaki, C. Huang, D. Garvey, J. Zhou, H. C. Kapteyn, M. M. Murnane, "Generation of 11-fs pulses from a self-mode-locked Ti:sapphire laser," Opt. Lett. 18, 977-979 (1993).
12. N. Sarukura,Y. Ishida,T. Yanagawa, H. Nakano, "All solid-state cw passively mode-locked Ti:sapphire laser using a coloured glass filter," App. Phys. Lett. 57, 229-230 (1990).
13. M. Ebrahim-Zadeh, "Mid-Infrared ultrafast and continuous-wave optical parametric oscillators," (in Solid-State Mid-Infrared Laser Sources, Springer-Verlag, 2003).
14. M. Ebrahim-Zadeh, M. H. Dunn, "Optical parametric oscillators," Handbook of optics, 2nd ed. (Optical Society of America, Washington, D.C.), Chapter. 22 (2000).
15. R. C. Gray, "The Rev. John Kerr, F.R.S. Inventor of the Kerr Cell," Nature, 136, 245-247 (1935).
16. C. V. Raman, K. S. Krishnan, "A new type of secondary radiation," Nature, 121, 501-502 (1928).

17. E. Schrödinger, "A new exact solution in non-linear optics," Proc. Royal Irish Academy 49 A, 59-66 (1943).
18. E. Schrödinger, "Nonlinear optics," Proc. Royal Irish Academy 47 A, 77-117 (1942).
19. P. A. Franken, A. E. Hill, C. W. Peters, G. Weinreich, "Generation of optical harmonics," Phys. Rev. Lett. 7, 118-119 (1961).
20. M. Bass, P. A. Franken, A. E. Hill, C. W. Peters, G. Weinreich, "Optical mixing," Phys. Rev. Lett. 8, 18-18 (1962).
21. J. A. Giordmaine, "Mixing of light beams in crystals," Phys. Rev. Lett. 8, 19-21 (1962).
22. P. D. Maker, R. W. Terhune, M. Nisenoff, C. M. Savage, "Effects of dispersion and focusing on the production of optical harmonics," Phys. Rev. Lett. 8, 21-22 (1962).
23. P. K. Tien, "Parametric amplification and frequency mixing in propagating circuits," J. Appl. Phys. 29, 1347-1357 (1958).
24. P. K. Tien, H. Suhl, "A traveling-wave ferromagnetic amplifier," Proc. IRE, 700-706 (1958).
25. A. W. Smith, N. Braslau, "Observation of an optical difference frequency," J. Appl. Phys. 34, 2105-2106 (1963).
26. R. H. Kingston, "Parametric amplification and oscillation at optical frequencies," Proc. IRE 50, 472-473 (1962).
27. N. M. Kroll, "Parametric amplification in spatially extended media and application to the design of tuneable oscillators at optical frequencies," Phys. Rev. 127, 1207-1211 (1962).
28. S. A. Akhmanov, R. V. Khokhlov, "Concerning one possibility of amplification of light waves," Zh. Eksperim. i Teor. Fiz. 16, 252-254 (1963).
29. J. A. Giordmaine, R. C. Miller, "Tunable coherent parametric oscillation in $LiNbO_3$ at optical frequencies," Phys. Rev. Lett.14, 973-976 (1965).
30. R. G. Smith, J. E. Geusic, H. J. Levinstein, S. Singh, L. G. Van Uitert, "Low-threshold optical parametric oscillator using $Ba_2NaNb_5O_{15}$," J. Appl. Phys. 39, 4030-4032 (1968).
31. R. L. Byer, M. K. Oshman, J. F. Young, S. E. Harris, "Visible cw parametric oscillator," App. Phys. Lett. 13, 109-111 (1968).
32. R. L. Sutherland, "Handbook of nonlinear optics," 2nd ed. (Marcel Dekker, Inc. 1996).
33. Y. X. Fan, R. C. Eckardt, R. L. Byer, R. K. Route, R. S. Feigelson, "$AgGaS_2$ infrared parametric oscillator," App. Phys. Lett. 45, 313-315 (1984).

34. M. J. Rosker, C. L. Tang, "Widely tunable optical parametric oscillator using urea," J. Opt. Soc. Am. B 2, 691-696 (1985).
35. L. K. Cheng, W. R. Bosenberg, C. L. Tang, "Broadly tunable optical parametric oscillation in β-BaB_2O_4," App. Phys. Lett. 53, 175-177 (1988).
36. M. Ebrahim-Zadeh, A. J. Henderson, M. H. Dunn, "An Excimer-pumped β-BaB_2O_4 optical parametric oscillator tunable from 354 nm to 2.370 μm," IEEE J. Quantum Electron. 26, 1241-1252, (1990).
37. M. Ghotbi, A. Esteban-Martin, M. Ebrahim-Zadeh, "BiB_3O_6 femtosecond optical parametric oscillator," Opt. Lett. 31, 3128-3130 (2006).
38. M. Ghotbi, A. Esteban-Martin, M. Ebrahim-Zadeh, "Tunable, high-repetition-rate, femtosecond pulse generation in the ultraviolet," Opt. Lett. 33, 345-347 (2008).

Chapter 2

Basic principles of nonlinear optics

2.1 The origin of optical nonlinearity

Optics is the study of the interaction of electromagnetic waves with the transparent dielectric material [1-3]. When a material is exposed to an electromagnetic beam, the positive charges within the material are displaced slightly in the direction of the electric field, and the negative charges are displaced minutely in the direction opposite to the electric field, and the system is thus polarized. The electromagnetic response of a material to the incoming electric field can be explained as the dependence of the induced polarization, P, which is a dipole moment[1] per unit volume, on the magnitude of the applied electric field [3-6]. When the magnitude of the input electric field is small, the induced polarization follows a linear dependence on the input field strength and is expressed as

$$P(t) = \varepsilon_0 \chi^{(1)} E(t) \tag{2.1}$$

In the above equation, P, denotes the polarization vector, ε_0 is the vacuum permittivity, E is the electric field vector of the incoming electromagnetic wave and $\chi^{(1)}$ is the linear susceptibility, which is a second-order tensor, depending on the frequency (ω) of the optical radiation [5,6]. This is a regime of *linear optics* or the optics of weak light in which the incident electromagnetic wave may get deflected or delayed, but the frequency

[1] Electric dipole moment vector is defined as $\Delta p = \int r dq$, in which r is a displacement vector and dq is an electric charge element in a volume v.

of the outgoing beam will be the same as the incoming electromagnetic wave, since the induced dipole moment oscillates with the same frequency as the incoming light.

On the other hand, when the electric field strength is comparable to the intra-atomic electric field[2], which is typically about 10^{11} V/cm [5,6], the response of the material to the incoming electric field is no longer linear. In this situation, the nonlinear optical response of the material is characterized by higher-order nonlinear susceptibilities and the polarization term is explained as power series in the applied electric field [5,7]

$$P(t) = \varepsilon_0[\chi^{(1)}E(t) + \chi^{(2)}E^2(t) + \chi^{(3)}E^3(t) + \cdots] \tag{2.2}$$

in which $\chi^{(m)}$, with m>1, is the m^{th}-order nonlinear optical susceptibility. This regime, where the incoming intense light induces additional dipole moment oscillations as it propagates inside a medium is called *nonlinear optics*. In this case, the induced dipole moment oscillates not only at the same frequency as the incoming beam, but also at higher and lower frequencies, which results in generating new wavelengths.

The response of a material to the stimulating optical field can be understood by using the sample of a classical system of a mass on a spring. If the system is pulled by a gentle force, the harmonic oscillation of the system can be seen and can be easily followed. On the other hand, if the applied force is strong, a nonlinear oscillation can be observed and the oscillation of the system is not harmonic anymore and it cannot be followed easily [8].

In Eq. (2.1), the first-order and linear polarization was defined. Similarly, the second-order nonlinear polarization can be expressed as

$$P^{(2)}(t) = \varepsilon_0\chi^{(2)}E^2(t) \tag{2.3}$$

and the third-order polarization as

$$P^{(3)}(t) = \varepsilon_0\chi^{(3)}E^3(t) \tag{2.4}$$

[2] The intra-atomic electric field is defined as $E_{at} = e/(4\pi\varepsilon_0 a_0^2)$, in which e is the charge of the electron, ε_0 is the vacuum permittivity, and $a_0 = 4\pi\varepsilon_0\hbar^2/(me^2)$ is the Bohr radius of the hydrogen atom. Here, $\hbar$ is Planck's constant divided by 2π, and m is the mass of the electron.

According to Eq. (2.3) and (2.4), and considering a large stimulating optical field in the order of intra-atomic electric field, one can estimate the magnitude of the second- and third-order nonlinear susceptibility to be ~10^{-12} m/V and ~10^{-24} m^2/V^2, respectively [5].

The second-order nonlinear optical susceptibility, $\chi^{(2)}$, describes second-order nonlinear optical phenomena such as second-harmonic-generation and difference-frequency-generation while, the third-order nonlinear optical susceptibility, $\chi^{(3)}$, is responsible for third-harmonic-generation, stimulated Raman scattering, phase conjugation and optical bistability [5].

The invention of laser paved the way of providing coherent sources with high intensities and hence advancing the field of nonlinear optics. Nowadays, nonlinear optics is a vast and important field in physics and has found much interest in science and technology [9-11].

The work presented in this thesis is based on the second-order nonlinear processes, so we restrict our brief introduction to the interactions involving second-order nonlinear optical susceptibility, meaning $\chi^{(2)}$. The description of other nonlinear optical interactions can be found in different well-known references [5,8-10].

2.2 Second-order nonlinear optical processes

As mentioned in Section 2.1, the second-order nonlinear polarization can be represented as

$$P^{NL}(t) = \varepsilon_0 \chi^{(2)} E^2(t) \tag{2.5}$$

where, $\chi^{(2)}$ is the second-order nonlinear susceptibility tensor of the third order, which has 27 elements. It is written as $\chi^{(2)}_{ijk}$, where the indices refer to the Cartesian components of the field and represent the optical polarization directions. It is to be noted that the second-order nonlinear susceptibility only exists in a medium without inversion symmetry. Inversion symmetry means that if the sign of the applied electric field, $E(t)$, is changed, the sign of the induced polarization must also change and accordingly the Eq. (2.5) becomes

$$-P^{NL}(t) = \varepsilon_0 \chi^{(2)}(-E)^2(t) \tag{2.6}$$

which implies

$$-P^{NL}(t) = \varepsilon_0 \chi^{(2)} E^2(t) \tag{2.7}$$

Comparing Eq. (2.6) and (2.7) results in the equality of $-P^{NL}(t)$ and $P^{NL}(t)$, meaning that $\chi^{(2)}$ should be zero. Therefore, second-order nonlinear optical effects cannot be induced in centrosymmetric materials and are only possible in non-centrosymmetric materials, while third-order nonlinear optical interactions can occur in both centrosymmetric and non-centrosymmetric media [5,7]. In table 2.1, we summarize the classification of crystal groups [5,12].

More commonly, the susceptibility is represented by a so called d-coefficient, which is given by [7]

$$d_{ijk} = \frac{1}{2}\chi^{(2)}_{ijk} \tag{2.8}$$

Using the above notation and the Kleinman symmetry[3] [13-15], the nonlinear susceptibility tensor can be contracted into a 3×6-elemnt matrix, thus the nonlinear polarization is given by

$$\begin{pmatrix} P_x(\omega_3) \\ P_y(\omega_3) \\ P_z(\omega_3) \end{pmatrix} = 2\varepsilon_0 K \begin{bmatrix} d_{11} & d_{12} & d_{13} & d_{14} & d_{15} & d_{16} \\ d_{21} & d_{22} & d_{23} & d_{24} & d_{25} & d_{26} \\ d_{31} & d_{32} & d_{33} & d_{34} & d_{35} & d_{36} \end{bmatrix} \times \begin{bmatrix} E_x(\omega_1)E_x(\omega_2) \\ E_y(\omega_1)E_y(\omega_2) \\ E_z(\omega_1)E_z(\omega_2) \\ E_y(\omega_1)E_z(\omega_2) + E_z(\omega_1)E_y(\omega_2) \\ E_x(\omega_1)E_z(\omega_2) + E_z(\omega_1)E_x(\omega_2) \\ E_x(\omega_1)E_y(\omega_2) + E_y(\omega_1)E_x(\omega_2) \end{bmatrix} \tag{2.9}$$

[3] Kleinmann symmetry says that when nonlinear interactions occur for frequencies far from any resonant frequency of the material, the nonlinear susceptibility is essentially independent of frequency and the indices of $\chi^{(2)}_{ijk}$ can be permuted without permuting the frequencies.

where *K* is the degeneracy factor, whose value depends on the conversion process.

If an optical field, consisting of two distinct frequency components, ω_1 and ω_2, and expressed as

$$E(t) = E_1(t)\exp(-i\omega_1 t) + E_2(t)\exp(-i\omega_2 t) + c.c \tag{2.10}$$

is incident upon a second-order nonlinear medium, the second-order nonlinear polarization, using Eq. (2.5) and (2.10), is given by

$$\begin{aligned} P^{(2)}(t) = \varepsilon_0\chi^2[E_1^2(t)\exp(-2i\omega_1 t) + E_2^2(t)\exp(-2i\omega_2 t)] \\ +2E_1E_2\exp(-i(\omega_1 + \omega_2)t) + 2E_1E_2^*\exp(-i(\omega_1 - \omega_2)t) + c.c] \\ +2\varepsilon_0\chi^{(2)}[E_1E_1^* + E_2E_2^*] \end{aligned} \tag{2.11}$$

The first two terms in Eq. (2.11) represent the second-harmonic-generation (SHG) process. The third and the forth terms express the sum-frequency-generation (SFG) and the difference-frequency-generation (DFG) process, respectively, and the last term is known as optical rectification (OR). It is to be noted that the degeneracy factor, *K*, in Eq. (2.9), takes the value of $^1/_2$ for degenerate cases of OR ($\omega_1 = \omega$, $\omega_2 = -\omega$) and SHG ($\omega_1 = \omega_2 = \omega$), and 1 for other conversion processes.

The physical meaning of these second-order nonlinear optical processes is illustrated in Fig. 2.1.

Optic Axis	**Crystal Category**	**Centro-Symmetry Point Group**		**Non-Centro-Symmetric Point Group**				
				Polar			Non-Polar	
Biaxial	Triclinic	$\bar{1}$		1			None	
	Monoclinic	2 or m		2	m		None	
	Orthorhombic	mmm		mm2			222	
Uniaxial	Tetragonal	4 or m	4 or mmm	4	4mm	$\bar{4}$	$\bar{4}$2m	422
	Trigonal	$\bar{3}$	$\bar{3}$m	3	3m	32		
	Hexagonal	6 or m	6 or mmm	6	6mm	$\bar{6}$	$\bar{6}$23	622
Optically Isotropic	Cubic	m3	m3m	None		432	$\bar{4}$3m	23

Table 2.1. Classification of crystal groups.

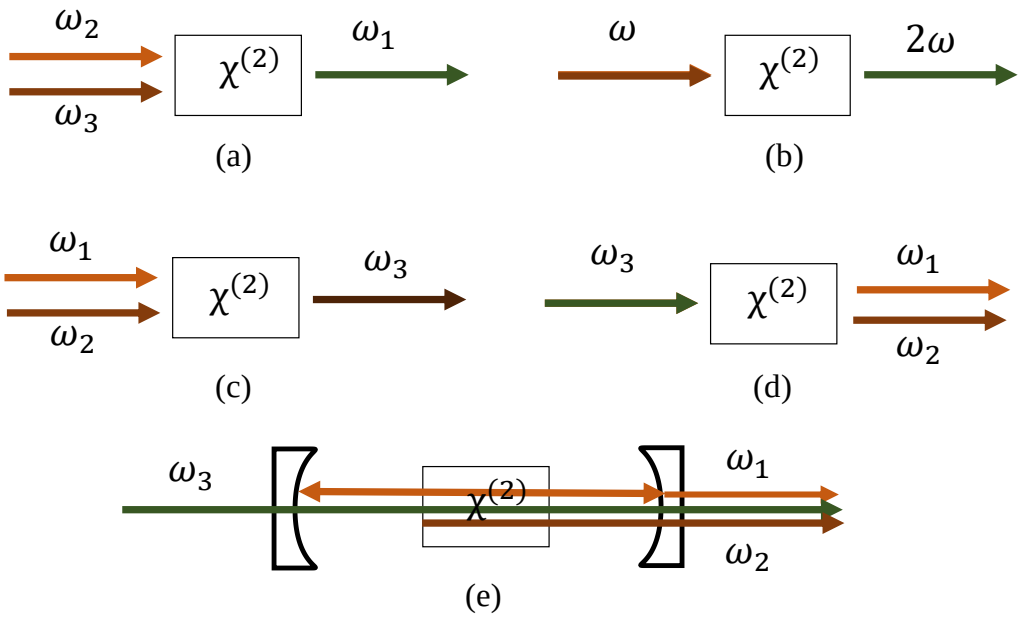

Fig. 2.1. Schematic diagram of the second-order nonlinear processes. (a) SFG, (b) SHG, (c) DFG, (d) OPG, (e) OPO.

In SFG process, Fig. 2.1(a), the energy of the two input photons, ω_2 and ω_3, which travel through the nonlinear optical medium, add together and result in one photon of higher energy, $\omega_1 = \omega_2 + \omega_3$. The SHG is the degenerate case of SFG process, where two low-energy photons at the same frequency, $\omega_2 = \omega_3 = \omega$, combine to generate one photon of energy twice that of the incoming photon energy, at frequency $\omega_1 = 2\omega$, as it is shown in Fig. 2.1(b). In the DFG process, two input photons at frequencies ω_1 and ω_2 are converted into one photon at a lower frequency of $\omega_3 = \omega_1 - \omega_2$, as shown in Fig. 2.1(c). This process also leads to the possibility of achieving parametric gain to realize optical parametric amplification (OPA). Figure 2.1(d) shows another type of process known as optical parametric generation (OPG), which starts with one input photon at frequency, ω_3, and generates two lower-energy photons at ω_1 and ω_2. The two generated photons are conventionally called *signal* (with the shorter wavelength) and *idler* (with the longer wavelength). An OPG in combination with an optical cavity to provide the oscillation for one, two, or all the three interacting beams in order to enhance the efficiency of the process, constitutes an optical parametric oscillator (OPO), Fig. 2.1(e).

In all of the mentioned frequency conversion processes, the energy of the photons participating in the frequency mixing process should be conserved as well as the relative phase between the interacting beams. The conservation of momentum or wave-vectors of the interacting beams, also known as a *phase-matching condition*, will be discussed later, in the Section 2.4.

2.3 The nonlinear wave equation and the coupled-wave equations for the second-order nonlinear optical processes

In the previous sections of this chapter, we have shown how nonlinearity in the response of a dielectric material to an intense incident electromagnetic field can induce polarization leading to the generation of new frequency components, which are not present in the incident radiation field. Maxwell's wave equations can describe the generation of these new components of the incoming field. For a charge-free, non-conducting and non-magnetic medium, Maxwell's equations can be written as

$$\nabla \cdot D = 0, \qquad \nabla \cdot B = 0$$
$$\nabla \times \mathrm{E} = -\frac{\partial B}{\partial t}, \qquad \nabla \times \mathrm{H} = \frac{\partial D}{\partial t} \tag{2.12}$$

where D is the electric displacement vector, defined as $D = \varepsilon_0 E + P$, and H is the magnetic field strength, related to the magnetic flux B by $B = \mu_0 H$, in which μ_0 is the permeability of free space.

In such a medium, the optical wave equation, which governs the propagation of electromagnetic radiation, can be represented by

$$\nabla^2 E - \frac{1}{c^2}\frac{\partial^2 E}{\partial t^2} = \mu_0 \frac{\partial^2 P}{\partial t^2} \tag{2.13}$$

where c is the speed of light in vacuum. Using Eq. (2.12), along with the relations $v = {}^{c}/_{n}$, $n^2 = 1 + \chi$, and $c = {}^{1}\Big/_{(\sqrt{\varepsilon_0 \mu_0})}$, Eq. (2.13) can be rewritten as

$$\nabla^2 E - \frac{1}{v^2}\frac{\partial^2 E}{\partial t^2} = \mu_0 \frac{\partial^2 P^{NL}}{\partial t^2} \tag{2.14}$$

where the term on the right-hand-side is the nonlinear source of radiation.

In a lossless nonlinear medium, the optical electric field at frequency ω_j, where j=1,2,3, represents the three interacting fields propagating in the z-direction, is given by

$$E_j(z,t) = E(z,\omega_j)\, exp\left(i\left(k_j z - \omega_j t\right)\right) + \ c.c \tag{2.15}$$

and the nonlinear source term is given by

$$P_j(z,t) = P(z,\omega_j)\exp\left(i\left(k_j z - \omega_j t\right)\right) + c.c \tag{2.16}$$

in which, $k_j = {}^{n_j(\omega_j)\omega_j}/_{c}$ is the wave-number and $n_j(\omega_j)$ is the refractive index at frequency ω_j. The refractive index is expressed as $n(\omega_j) = \sqrt{{}^{\varepsilon(\omega_j)}/_{\varepsilon_0}}$, where $\varepsilon(\omega_j)$ is the permittivity of the medium at frequency ω_j. Assuming the slowly-varying amplitude approximation [5,13], where the amplitudes of the fields vary slowly over a distance comparable to the wavelength under the condition of

$$\frac{d^2 E}{dz^2} \ll \left| k_j \frac{dE_j}{dz} \right| \tag{2.17}$$

the wave equations for interacting beams become

$$\frac{\partial E_1}{\partial z} = \frac{i\omega_1^2 d_{eff}}{k_1 c^2} E_3 E_2^* exp(i\Delta k z)$$

$$\frac{\partial E_2}{\partial z} = \frac{i\omega_2^2 d_{eff}}{k_2 c^2} E_3 E_1^* \, exp(i\Delta k z) \tag{2.18}$$

$$\frac{\partial E_3}{\partial z} = \frac{i\omega_3^2 d_{eff}}{k_3 c^2} E_1 E_2 exp(i\Delta k z)$$

where d_{eff} is the effective nonlinear coefficient and $\Delta k = k_1 - k_2 - k_3$ is the momentum or phase-mismatch between the interacting fields, both of them depend on

the optical properties of the medium, frequency of the involving waves, and propagation directions. These equations are called the *coupled amplitude equations*, where various frequency components are coupled by the nonlinear interaction and show the variation in the amplitude of one field due to its coupling to the other fields.

2.4 Phase-matching

For the attainment of efficient nonlinear optical process, the phase-matching condition, as well as the conservation of the energy, should be satisfied. The idea of matching the phases of the interacting beams was first proposed separately by Giordmaine [16] and Maker [17] in 1962. They showed that only under $\Delta k = 0$, with $k = 2\pi n_i/\lambda_i$, the nonlinear optical interaction will undergo macroscopic amplification as the interacting waves propagate through the nonlinear optical medium.

Due to the dispersion in the material, in general the optical waves with different wavelengths propagate with different phase velocities, so that $\Delta k \neq 0$. Under this condition, after travelling a short distance, which is called the coherence length, l_c, the relative phase of the interacting waves slips by 180º. This oscillation in the relative phase causes the interacting beams to interfere constructively and destructively as they travel through the nonlinear optical medium. Therefore, they exchange energy back and forth, which results in the oscillating generated fields along the propagation direction. In Fig. 2.2, is depicted the generated intensity in a second-order nonlinear optical process along a nonlinear medium for (a) perfectly phase-matched and (c) non-phase-matched cases. Figure 2.2(b) shows quasi-phase-matched case, which will be discussed in Section 2.4.2.

There are two important techniques to achieve phase-matching, *birefringent phase-matching* [16-18] and *quasi-phase-matching* [19], which will be explained in the following sections.

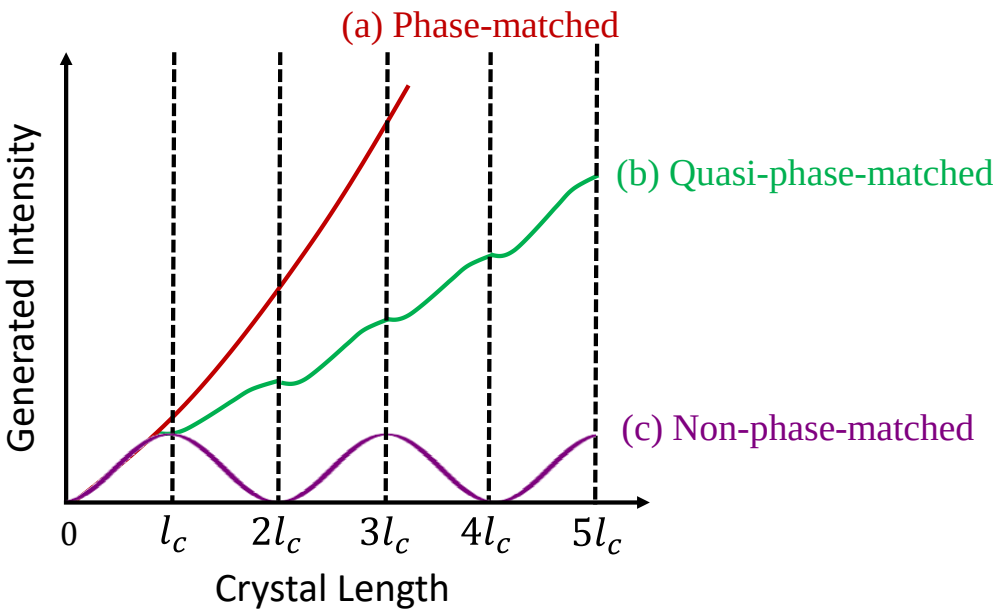

Fig. 2.2. Generated beam intensity as a function of propagation distance in a nonlinear crystal for the case of (a) perfectly phase-matched, (b) quasi-phase-matched, and (c) non-phase-matched second-order nonlinear optical process. l_c is the coherence length.

2.4.1 Birefringent phase-matching

As mentioned before, the problem of phase-mismatch arises from the fact that the fundamental and the generated beams propagate with different phase velocities, because of experiencing different refractive indices. The difference in refractive indices comes from the different wavelengths, it also can be due to some optical properties of the medium itself. In some optical materials, which are called birefringent materials, there is a polarization-dependent behaviour of the refractive indices. Depending on the number of optic axes, birefringent crystals can be divided into two categories, *uniaxial crystals* in which there is one optic axis, with $n_x = n_y \neq n_z$, and *biaxial crystals* in which there are two optic axes, with $n_x \neq n_y \neq n_z$ [13,20]. Nonlinear optical crystals such as β-BaB_2O_4 (BBO), $LiNbO_3$ (LN) and $CdSiP_2$ (CSP) are uniaxial [20,21], while BiB_3O_6 (BIBO), LiB_3O_5 (LBO) and $KTiOPO_4$ (KTP) are categorized as biaxial crystals [20].

If an incident beam experiences refractive index regardless of the direction of propagation in the medium, it is called an *ordinary* (*o*)-wave. In a uniaxial crystal, the electric vector

of an *o*-wave is perpendicular to the optic axis of the medium. If θ is defined as an angle between the propagation direction and the optic axis (z-axis), the refractive index of an *o*-polarized wave can be expressed as $n_o(\theta) = n_o$. An incident beam with orthogonal polarization to an *o*-polarized wave, with the electric vector parallel to the optics axis, experiences a varying refractive index with the propagation direction. This polarization corresponds to an *extraordinary* (*e*)-wave. The refractive index of an *e*-wave, which propagates at angle θ to the optic axis in a uniaxial crystal, is given by [13]

$$\frac{1}{n_e^2(\theta)} = \frac{\cos^2(\theta)}{n_o^2} + \frac{\sin^2(\theta)}{n_e^2} \tag{2.19}$$

where $n_o$and n_e are the principal refractive indices of the uniaxial crystal.

Uniaxial crystals are classified into two types, positive uniaxial for which $n_o < n_e$, and negative uniaxial for which $n_e < n_o$. LN, BBO and CSP are negative uniaxial crystals, while $ZnGaP_2$ (ZGP) is a positive uniaxial crystal [13,20]. The refractive index surfaces of positive and negative uniaxial crystals are illustrated in Fig. 2.3.

By using the concept of birefringence in the nonlinear optical material, phase-matching between interacting beams in a second-order nonlinear optical process can be achieved. When interacting waves of different frequencies are polarized differently, their corresponding phase velocities can be adjusted by using the birefringence properties of a nonlinear optical crystal. In this case, the refractive index difference due to dispersion is balanced by the refractive index difference due to birefringence. This technique is known as *birefringent phase-matching* (BPM). BPM can be realized in two types. If the input beams have the polarization orthogonal to the generated field, the phase-matching process is known as type-I, whereas type-II refers to the case where the incoming fields are polarized orthogonally.

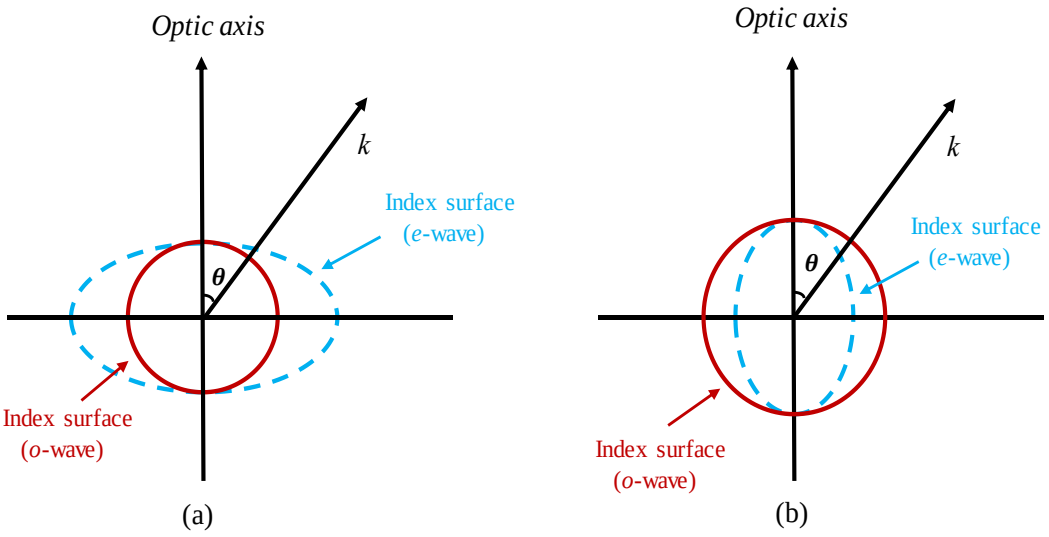

Fig. 2.3. Index ellipsoids for (a) a positive uniaxial crystal, and (b) a negative uniaxial crystal. k, represents a wave-vector. θ, is an angle between the propagation direction and the optic axis.

To understand the concept of BPM, we consider the case of SHG process in a positive uniaxial crystal. In this case, the phase-matching condition can be written as

$$2k_{\omega} - k_{2\omega} = 0 \tag{2.20}$$

$$\frac{4\pi n_{\omega}}{\lambda} = \frac{2\pi n_{2\omega}}{\lambda/2} \Rightarrow n_{\omega} = n_{2\omega}$$

Figure 2.4 shows the propagation direction at an angle, θ, where the extraordinary index for the fundamental wave at frequency, ω, is equal to the ordinary refractive index for the second-harmonic wave at frequency, 2ω, thus compensating the dispersion, and resulting in perfect type-I phase-matching ($ee \rightarrow o$).

In an anisotropic optical medium, the electric permittivity, as a tensor, is defined as

$$\begin{pmatrix} \varepsilon_{xx} & \varepsilon_{xy} & \varepsilon_{xz} \\ \varepsilon_{xy} & \varepsilon_{yy} & \varepsilon_{yz} \\ \varepsilon_{xz} & \varepsilon_{zy} & \varepsilon_{zz} \end{pmatrix} \tag{2.21}$$

Using the above equation together with the Eq. (2.12), one can see that in an anisotropic medium the direction of beam propagation or wave-vector (k) is different from the direction of energy flow, which is given by the Poynting vector, $S = E \times H$. This phenomenon is known as double-refraction, spatial walk-off, or Poynting vector walk-off. The walk-off reduces the spatial overlap between the interacting *o*- and *e*- polarized beams in the nonlinear optical crystal, and limits the interaction length of the nonlinear material. An effective crystal length in the presence of walk-off is defined as

$$l_a = \left(\frac{\sqrt{\pi}}{\rho}\right) w_o \tag{2.22}$$

where w_o is the waist radius of the input beam, and ρ is a spatial walk-off angle. The walk-off angle can be calculated from

$$\tan(\rho) = -\frac{1}{n_e(\theta)} . \frac{dn_e(\theta)}{d\theta} \tag{2.23}$$

where the minus sign indicates that the walk-off occurs in the direction where the refractive index would decrease. For a uniaxial crystal, the walk-off angle can be written as

$$\tan(\rho) = -\frac{1}{2} . |n_e(\theta)|^2 \left(\frac{1}{n_e^2} - \frac{1}{n_o^2}\right) \sin(2\theta) \tag{2.24}$$

As it is obvious from Eq. (2.24), spatial walk-off can be overcome if the nonlinear interaction occurs at an angle $\theta = 90°$. In this case, the interaction is held under *noncritical phase-matching* (NCPM), where the nonlinear crystal length becomes the effective interaction length of the nonlinear optical process. If $\theta \neq 90°$, the nonlinear interaction operates under what is called *critical phase-matching* (CPM).

Although for the first 25 years of the advent of coherent nonlinear optics, BPM was the mostly used technique for satisfying phase-matching [22], it is actually limited to those crystals which show birefringence. Using the BPM concept also limits the convenient choices of polarizations of the interacting beams and can hinder using the largest component of the nonlinear susceptibility tensor, and hence limiting the extraction efficiency.

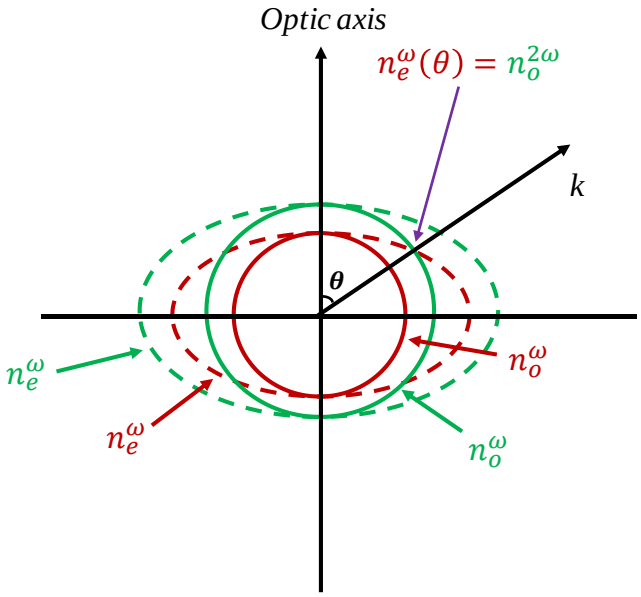

Fig. 2.4. Illustration of type-I birefringent phase-matching for SHG in a uniaxial crystal.

2.4.2 Quasi-phase-matching

As mentioned in Section 2.4.1, in BPM the difference in the phase velocity of the polarized waves is used to balance the difference in the refractive indices due to dispersion in the medium. An alternative approach to achieve the phase-matching condition in the nonlinear optical process is called *quasi-phase-matching* (QPM), first proposed by Armstrong in 1962 [23].

As introduced before, the coherence length, $l_c = {\pi}/{\Delta k}$, is a distance in the nonlinear optical medium over which the interacting beams remain in phase. The main idea of QPM is somehow to keep introducing such a coherence length to the interacting beams. In a nonlinear optical medium for each coherence length the phase difference of π is accumulated by the interaction and the optical nonlinear process reverses its direction. If a phase shift of π is added periodically every coherence length, the field intensity of the generated wave(s) will keep increasing. This periodic modification of the properties of the nonlinear optical medium can be achieved by several methods including periodic total internal reflection [24-26], periodic propagation over dispersive phase-slip regions, [27] periodic inversion of the sign of the second-order nonlinear coefficient [23], or by

inverting the crystallographic orientation, which corresponds to flipping the crystal orientation [28-30]. However, a common method for implementing the QPM is to reverse the sign of nonlinear coefficient through periodic poling of a ferroelectric medium such as LN [31,32], as shown in Fig. 2.5. In Fig. 2.2 is shown the concept of QPM technique for a second-order nonlinear process. As it is obvious, the build-up of an output intensity is slower than that in the case of perfect phase-matching. The nonlinear coefficient in the QPM process is given by

$$d = 2\frac{d_{eff}\sin(D\pi)}{(m\pi)} \tag{2.25}$$

where m is referred as the order of the QPM and D is the duty factor of the grating with $D = {}^{l}/_{\Lambda}$, where l is the grating length, and $\Lambda = 2l_c$ is the grating period. As it is clear, the nonlinear coefficient for a QPM process is lower than the nonlinear coefficient in a BPM. However, the QPM technique has several advantages, which make it more favourable for many frequency conversion processes. QPM process does not rely on birefringence, so any convenient choice of polarization can be applied, including the case in which all the interacting waves have parallel polarization, which is known as type-0 QPM, which is inaccessible to birefringent phase-matched interactions. The QPM technique is also applicable to isotropic media like GaAs and GaP, in which BPM is not available. This technique gives the largest component of the nonlinear susceptibility tensor in common ferroelectrics like LN, and thus enhances the efficiency of the process. It is always possible to use QPM for waves propagating along a crystal axis, which eliminates the Poynting vector walk-off and thus increasing the efficiency of the nonlinear optical interactions.

The advent and rapid evolution of lithographically controlled patterning, together with the development of crystal growth technology, paves the way for using QPM nonlinear optical crystals increasingly in different frequency conversion processes. Deploying different grating periods in a QPM crystal, tunable wavelengths can be achieved by using only one pumping wavelength and one nonlinear optical crystal. Besides, new QPM engineering, such as fan-out grating design, gives the possibility of fast wavelength tuning while operating at room temperature.

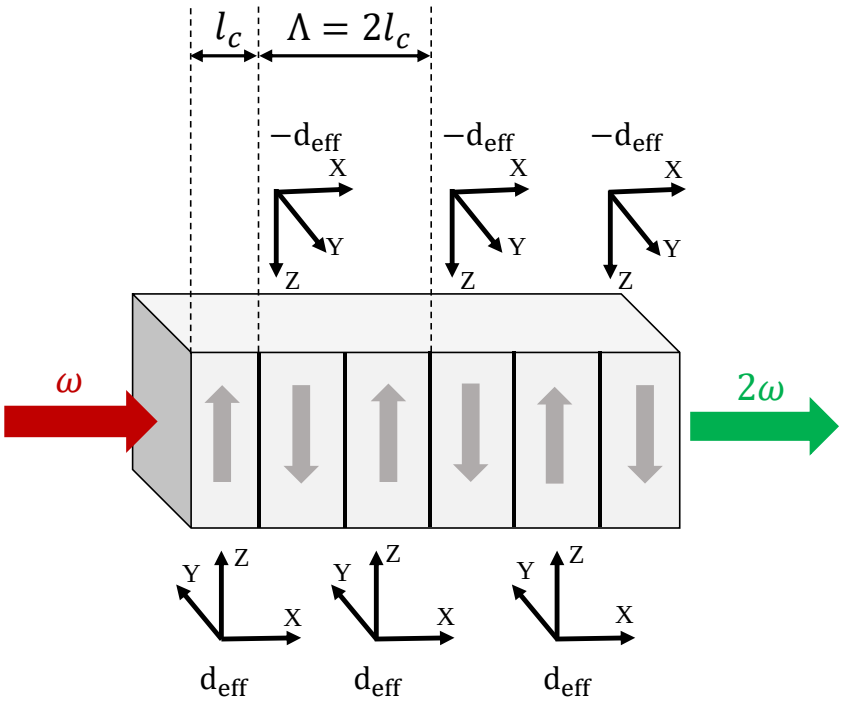

Fig. 2.5. Periodic inversion of the sign of the nonlinear coefficient by using a periodic poling in a QPM nonlinear crystal. l_c is the coherence length, Λ is the poling period. ω and 2ω are the frequencies of the incoming and the generated SH beam, respectively.

2.5 Optical parametric oscillators (OPOs)

An OPO consists of a second-order nonlinear optical crystal and a resonant cavity providing feedback, as shown in Fig. 2.1(e). Pumped at frequency, ω_P, an OPO produces parametric gain at both *signal* (ω_S) and *idler* (ω_I) frequencies satisfying both energy conservation and phase-matching,

$$\omega_P = \omega_S + \omega_I$$
$$k_P = k_S + k_I \tag{2.26}$$

If the feedback is provided at one (both or all) of the interacting beams and the gain exceeds a threshold value, an oscillator starts to work. An OPO in which either a signal or idler (but not both) can oscillate is called *singly-resonant oscillator* (SRO), Fig. 2.6(a). If the feedback is provided at both signal and idler, the device is then called *doubly-resonant* oscillator (DRO), and if the cavity permits all interacting beams to oscillate, it

is known as *triply-resonant oscillator* (TRO), as shown in Fig. 2.6(b) and Fig.2.6(c), respectively. The threshold intensity for DRO or TRO are lower than that for a SRO, so they are of highly interest in continuous-wave (cw) regime where lower pump intensity is available. However, SRO devices are more stable and provide single-frequency output [33,34].

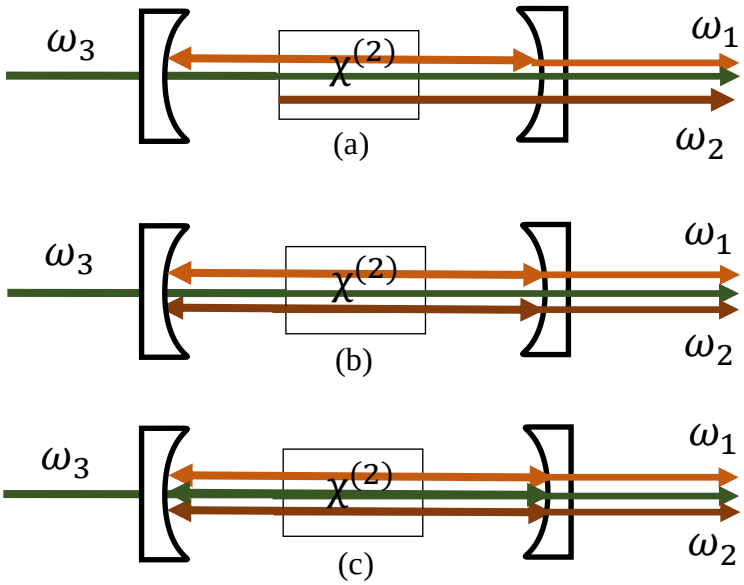

Fig. 2.6. Various OPO resonance configurations. (a) *singly-resonant oscillator* (SRO), (b) *doubly-resonant oscillator* (DRO), (c) *triply-resonant oscillator* (TRO).

Like lasers, OPOs have an optical resonator and a threshold, which is needed to be overcome. However, there are major differences between a laser and an OPO. The gain in an OPO is instantaneous, which means that the gain is only available in the presence of pump, but in a laser the emission is provided by the induced population inversion through energy storage. The instantaneous nature of the nonlinear gain enables an OPO to provide output beams in all the temporal regimes from the cw to ultrafast femtosecond time-scales by appropriate choice of pump source. However, in conventional laser systems the pulse duration of the emitted optical wave is limited by the lifetime of laser transition, which is related to a laser gain properties [33-38]. Moreover, in a laser the tunability of an output wavelength depends on the bandwidth of the electronic transitions, whereas in an OPO the wavelength tunability is obtained through phase-matching

conditions together with the energy conservation laws [33-38]. By using fiber laser as a pump source, OPOs can be configured in compact architectures and can provide high output power and efficiency, while they operate at or above room temperature without the need for cryogenic cooling.

Following the demonstration of the first OPO by Giordmaine and Miller in 1965 [39], studies on realizing tunable coherent sources in different time-scales with higher efficiency proceeded rapidly. As such, nowadays OPOs are recognized as viable and practical coherent sources, which are flexible alternatives to laser sources for a wide range of applications.

2.5.1 Parametric gain and amplification

Once the phase-matching condition is satisfied for the nonlinear optical process, signal and idler beams are generated from parametric noise and are amplified during their propagations through the nonlinear optical medium. The single-pass parametric gain in the nonlinear crystal is given by [11,13]

$$G_S(l) = \frac{I_S(l)}{I_S(0)} - 1 = \Gamma^2 l^2 \frac{sinh^2(\Gamma^2 l^2 - (\Delta kl/2)^2)^{\frac{1}{2}}}{[\Gamma^2 l^2 - (\Delta kl/2)^2]} \tag{2.27}$$

where I_S is the resonated beam intensity defined as $nc\varepsilon_0 \times (E_S E_S^*/2)$, l is the interaction length, and Δk is the phase-mismatch. Considering I_P as the pump beam intensity, the gain factor, Γ, is defined as [11,13]

$$\Gamma^2 = \frac{8\pi^2 d_{eff}^2}{c\varepsilon_0 n_P n_S n_I \lambda_S \lambda_I} I_P \tag{2.28}$$

in which n_P, n_S and n_I are the refractive indices of the pump, signal, and idler at wavelengths λ_P, λ_S and λ_I, respectively, c is the speed of light, and ε_0 is the electric permittivity of free space.

Under perfect phase-matching, when $\Delta k = 0$, Eq. (2.27) reduces to

$$G_S(l) = sinh^2(\Gamma l) \tag{2.29}$$

For low gains, $\Gamma l \ll 1$, the single-pass parametric gain reduces to $(\Gamma l)^2$ and in the case of high gain, $\Gamma l \gg 1$, it increases exponentially with $2\Gamma l$ as $G_S(l) = 1/4 \exp(2\Gamma l)$.

2.5.2 OPOs design issues

There are several issues should be considered while designing an OPO. The first principle is to maximize the parametric gain through suitable choice of nonlinear optical crystal. Other considerations are selecting appropriate pumping system, satisfying phase-matching conditions and cavity design, each of which plays an important role in order to develop efficient OPO sources.

2.5.2.1 Nonlinear material

There are several important parameters, which have to be taken into consideration when selecting a nonlinear crystal for developing an efficient OPO. First of all, the nonlinear optical crystal should be non-centrosymmetric with broad transparency range. It should be phase-matchable by using at least one of the mentioned phase-matching methods in Section 2.4. The crystal should have high nonlinear optical susceptibility and high laser damage threshold. The crystal should be also available in high quality with economic cost. The nonlinear figure-of-merit, defined as

$$FOM = {d_{eff}}\Big/{(\sqrt{n_P n_S n_I})} \tag{2.30}$$

is another important factor containing the physical parameters completely dependent upon the material, which can boost the efficiency of the nonlinear optical process since the gain parameter is proportional to $(FOM)^2$, according to Eq. (2.28).

Large phase-matching bandwidth of the nonlinear optical material with the length, $l_{crystal}$, is also desirable. The phase-matching bandwidth, defined as

$$\left| -\frac{\pi}{2} < \frac{\Delta k l_{crystal}}{2} < \frac{\pi}{2} \right| \tag{2.31}$$

shows the efficient energy transfer among the interacting waves.

Once the nonlinear material is chosen, its dispersion properties govern various parameters such as spectral ($\Delta\lambda$), angular ($\Delta\theta$) and temperature (ΔT) acceptance bandwidths as they indicate the maximum allowable pump linewidth, angular divergence, and variation in temperature for efficient parametric generation, respectively [11]. The pump spectral acceptance bandwidth can be calculated from the expansion of Δk for the central pump wavelength, λ_P, by using the Taylor-series expansion as [11,40]

$$\Delta k = (\Delta k)_{\lambda=\lambda_P} + \left(\frac{\partial \Delta k}{\partial \lambda}\right)_{\lambda=\lambda_P} . (\Delta\lambda) + \frac{1}{2}\left(\frac{\partial^2 \Delta k}{\partial \lambda^2}\right)_{\lambda=\lambda_P} . (\Delta\lambda)^2 + \cdots \qquad (2.32)$$

The first-term on the right-hand-side of Eq. (2.32) can be made zero by choosing an appropriate conditions leading to have phase-matching at λ_p [13]. In this situation, the spectral bandwidth of the pump that contributes to the efficient generation of signal and idler is limited by the second term, which is also referred to as the group velocity mismatch (GVM). The concept of GVM will be described in detail in Section 2.5.2.3. The pump spectral acceptance bandwidth for a signal-resonant OPO, with a nonlinear crystal with the length, $l_{crystal}$, is given by

$$\Delta\lambda_P \cdot l_{crystal} = 2.78 \times \frac{\lambda_P^2}{2\pi} \times [n_P - n_I - \lambda_P \frac{\partial n_P}{\partial \lambda_P} + \lambda_I \frac{\partial n_I}{\partial \lambda_I}]^{-1} \qquad (2.33)$$

In some crystals, such as LN, due to strong interplay between the dispersion properties of interacting waves, the GVM term takes very small values in certain spectral regions [41]. In this case, the pump spectral acceptance bandwidth is determined by the third term in the expansion of Δk from Eq. (2.32),

$$\Delta\lambda = 2\sqrt{\frac{5.57}{l_{crystal}}} \cdot [(\frac{\partial^2 \Delta k}{\partial \lambda^2})_{\lambda=\lambda_P}]^{-1/2} \qquad (2.34)$$

In a similar way, one can calculate the temperature acceptance bandwidth, $\Delta T. l_{crystal}$, by considering a negligible thermal expansion of the nonlinear optical medium. Temperature acceptance bandwidth measures the sensitivity of the phase-matching, thus the parametric gain, to the changes in the crystal temperature, and is expressed as

$$\Delta T \cdot l_{crystal} = \frac{2.78}{2\pi} \times [\lambda_P \frac{\partial n_P}{\partial T} - \lambda_S \frac{\partial n_S}{\partial T} - \lambda_I \frac{\partial n_I}{\partial T}]^{-1}] \qquad (2.35)$$

The spectral acceptance bandwidth for a 50-mm-long MgO-doped periodically-poled LN (MgO:PPLN) crystal pumped by 1064 nm Ytterbium-fiber (Yb-fiber) laser is shown in Fig. 2.7(a). Using the Sellmeier equation of [50], the spectral acceptance bandwidths is calculated to be $\Delta\lambda \sim 11.38$ nm. In Fig. 2.7(b), is shown the temperature acceptance bandwidth for a 532 nm-pumped periodically-poled KTP (PPKTP)-based OPO. By using a relevant Sellmeier equation of [51], the temperature acceptance bandwidth for a 10-mm-long PPKTP crystal is calculated to be $\Delta T \sim 5.42$°C.

As it is clear from Eq. (2.33) and (2.35), the acceptance bandwidth is inversely proportional to the crystal length, $l_{crystal}$. This implies that shorter crystal lengths can tolerate larger deviations. For the attainment of maximum parametric gain and minimum OPO threshold, the use of nonlinear materials with large spectral, angular, and temperature acceptance bandwidths is advantageous.

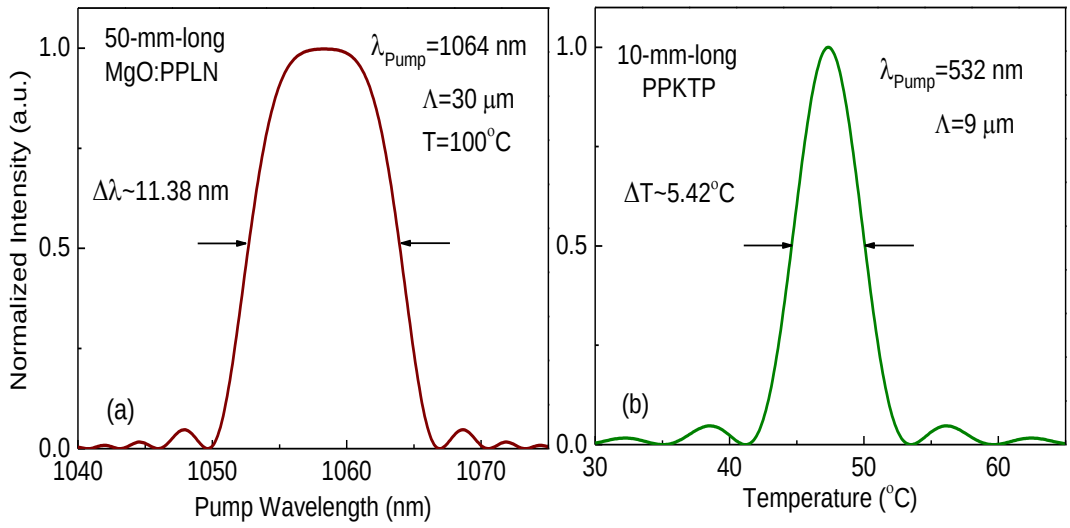

Fig. 2.7. (a) Normalized parametric gain as a function of pump wavelength for a 1064-nm-pumped 50-mm-long MgO:PPLN OPO, (b) temperature acceptance bandwidth for a 10-mm-long PPKTP-based OPO pumped by 532 nm.

2.5.2.2 Pump source

Since in the nonlinear optical process no pump energy is stored, the pump laser wavelength should lie within the transparency range of the nonlinear medium. The pump source must also have sufficient peak intensity (I_P) and low beam divergence to achieve the optimum focussing.

2.5.2.3 Dispersion characteristic of the nonlinear optical medium

I. Group velocity mismatch

In second-order frequency conversion processes three waves interact with each other while propagating through the nonlinear medium. Due to dispersion of the material, these different waves propagate at different group velocities and so the interacting beams may separate from each other after propagating some distance in the medium. This can result in the reduced effective interaction length and thus decreasing the efficiency of the process. Group velocity mismatch (GVM) between the interacting beams is a parameter that can evaluate this effect. The group velocity of the laser pulses propagating in a nonlinear optical medium is defined as [42]

$$v_g = \frac{d\omega}{dk} = \frac{c}{n - \lambda(\frac{dn}{d\lambda})} \tag{2.36}$$

where ω is an angular frequency of the electromagnetic beam with the wave-vector of k, c is the speed of light in vacuum, n is the refractive index of the nonlinear medium, and λ is the central wavelength of the laser beam. Then, GVM between λ_i and λ_j is defined as

$$GVM = \frac{1}{v_{gi}} - \frac{1}{v_{gj}} \tag{2.37}$$

where v_{gi} and v_{gj} are the group velocities of the two interacting waves at λ_i and λ_j.
The effective interacting length, l_{eff}, for wave i and wave j, considering they have the same pulse duration, τ, can be calculated as [43]

$$l_{eff} = \frac{\tau}{|GVM|} \tag{2.38}$$

II. Group velocity dispersion

Dispersion in the nonlinear optical material can reduce the effective interacting length. It can also affect the temporal width of the interacting beams. Group velocity dispersion (GVD) is an important temporal parameter, which can estimate the degree of pulse broadening and thus help to design the compensation configuration to achieve ultrashort pulses. GVD is calculated as the derivative of the inverse of group velocity of light in a material with respect to angular frequency, ω, as

$$GVD = \frac{\partial}{\partial \omega}\left(\frac{1}{v_g}\right) = \frac{\partial^2 k}{\partial \omega^2} = \frac{\lambda^3}{2\pi c^2}\frac{\partial^2 n}{\partial \lambda^2} \tag{2.39}$$

In Fig. 2.8 is shown the calculated GVD for the generated signal and idler from a 1064-nm-pumped MgO:PPLN OPO, using a relevant temperature-dependant Sellmeier equation of [50]. Normal (positive) dispersion, defined as a case in which GVD has positive values, implies that the group velocity increases with increasing wavelength, while anomalous (negative) dispersion occurs when GVD has negative values. The group velocities for the signal and idler from the mentioned OPO are plotted in Fig. 2.9. According to Fig. 2.8 and 2.9, for the signal wavelength from ~1400 nm to ~1862 nm, as the group velocity increases with increasing wavelengths, there is a normal dispersion and the GVD takes the positive values. However, from ~1862 nm to ~1910 nm, the group velocity takes smaller values and at ~1912 nm it changes the trend and the material shows negative dispersion. While for the idler wavelengths from ~2128 nm to ~4423 nm, MgO:PPLN crystal shows negative dispersion.

2.5.2.4 Cavity design

In order to construct an efficient OPO, appropriate design for the cavity is as important as selecting the appropriate nonlinear optical crystal and the pump source. A cavity for an OPO can be designed in different schemes, as presented in Fig. 2.10. The linear cavity (a), V-cavity (b), and X-cavity (c) are standing-wave cavities, while the ring cavity (d) is a travelling-wave cavity. A ring cavity is the most difficult configuration among the introduced schemes, since it has more difficult aligning process. However, in a ring cavity, for the single-pass of the resonating wave(s) through the crystal for every round-

trip, the losses due to material absorption and crystal coatings decreases, which results in the reduction of the threshold pump power. On the other hand, standing-wave cavities offer the possibility of double-pass pumping to reduce the threshold in SROs. It is also easier to introduce optics inside the standing-wave cavity or to remove them, without the need for realignment the system.

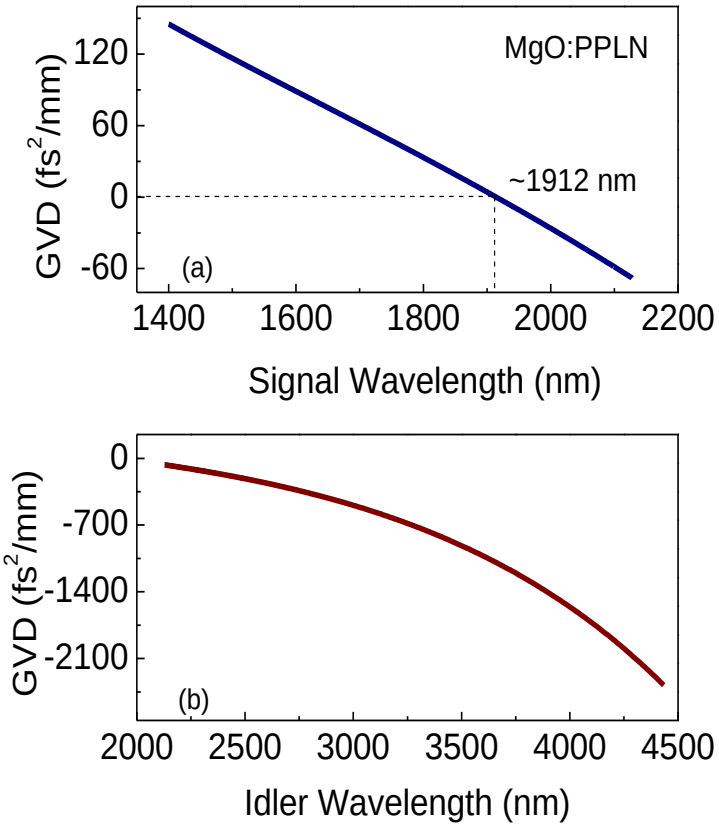

Fig. 2.8. Group velocity dispersion for (a) signal and (b) idler wavelengths generated from a 1064-nm-pumped OPO based on MgO:PPLN.

In order to provide optimum performance of an OPO, optimum overlap between the pump and the resonating beam(s) should be provided. Fulfilling this, the confocal parameter of the pump beam, b_p, should be equal to that of the resonating beam. The confocal parameter, which is twice the Rayleigh range, is defined as $b_P = (2\pi n w^2)/\lambda_P$ inside the cavity, and thus $b_S \sim b_P$ with n the refractive index of the nonlinear optical crystal, w the beam waist, and λ_P the pump wavelength. Here, we consider the signal wavelength is resonating inside the cavity, and thus $b_S \sim b_P$.

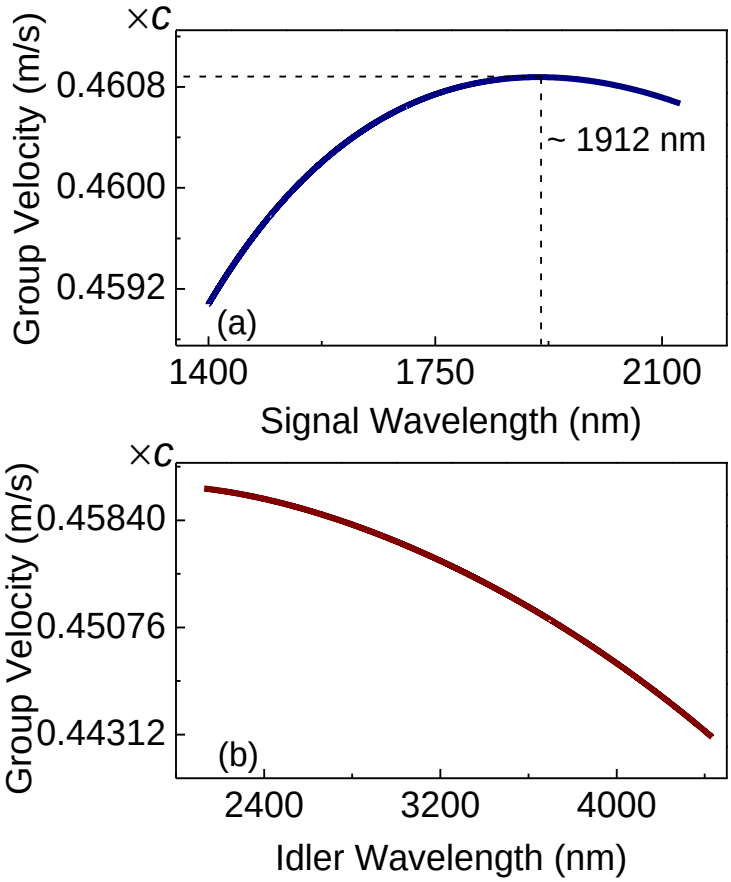

Fig. 2.9. Group velocity of (a) signal and (b) idler generated from a MgO:PPLN-based OPO pumped by 1064 nm. *c* is the speed of light.

Using the Gaussian beam transformation matrices [38,43], the signal beam waist can be calculated at any position inside the cavity. Considering a Gaussian beam propagates along z-direction, the beam waist, $w(z)$, and the radius of curvature of the beam, $R(z)$, are given by

$$w(z) = w_o^2\left(1 + \left(\frac{z}{z_o}\right)^2\right)$$
$$R(z) = z\left(1 + \left(\frac{z_o}{z}\right)^2\right) \tag{2.40}$$

in which w_o is the minimum beam waist at $z = 0$ and z_o is the Rayleigh range. Gaussian beam at a distance z can be expressed by using a complex beam parameter, given as

$$q(z) = z + iz \tag{2.41}$$

$$\frac{1}{q(z)} = \frac{1}{R(z)} - i\frac{\lambda}{n\pi w^2}$$

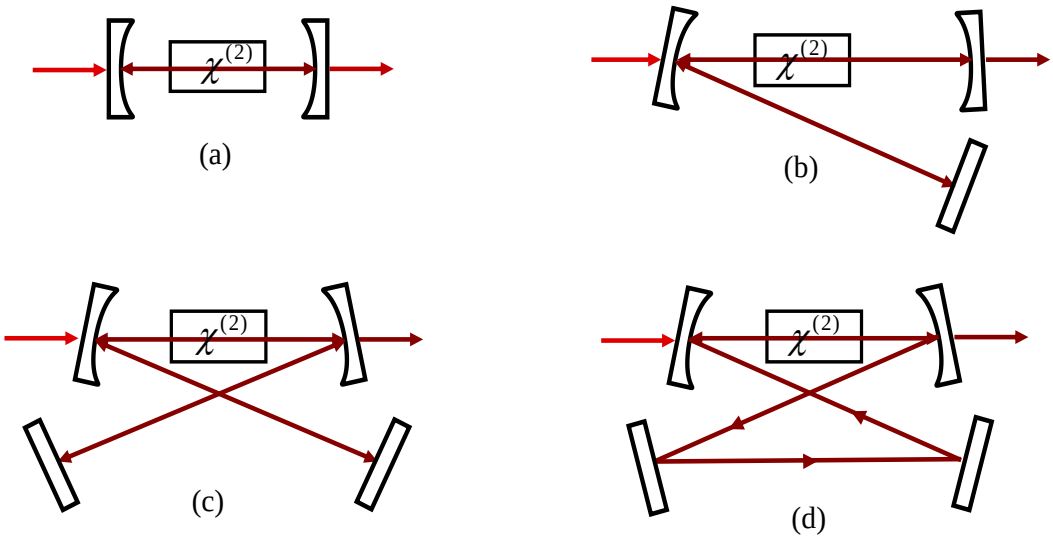

Fig. 2.10. Various cavity designs (a) linear cavity, (b) V-cavity, (c) X-cavity, (d) ring cavity.

Since the Gaussian beam remains Gaussian while propagating through passive optical elements, by using ABCD matrix, the complex beam parameter, q_1, can be related to its corresponding values after travelling a distance, *d*

$$q_2 = \frac{Aq_1 + B}{Cq_1 + D} \tag{2.42}$$

The general form of the ABCD matrix is

$$M = \begin{pmatrix} A & B \\ C & D \end{pmatrix} \tag{2.43}$$

where *A*, *B*, *C*, *D* are the ray matrix elements. A ray matrix analysis offers a convenient way of describing and tracing the propagation through various optical elements such as lenses, nonlinear crystals, and mirrors by using the corresponding transformation matrices. Some useful transformation matrices are listed in Table 2.2 [38,43]. The overall ABCD matrix can then be obtained by multiplication of all the individual transformation matrices in the beam path, such that the order in which the matrices appear in the product is opposite to the order in which the corresponding optical elements are exposed by light. Using the ABCD matrices and considering the condition for the stability of the cavity, meaning $-1 \leq (A+B)/2 \leq 1$, one can calculate the beam waist radius along the propagation inside the cavity starting from centre of the nonlinear crystal, to design a stable cavity. The typical cavity design for a ring and a V-cavity configuration are shown in Fig. 2.11(a) and (b), respectively, from which various design parameters such as the distance between the cavity mirrors and the optimum position of the crystal can be estimated.

Another important factor which should be considered in ultrafast OPOs is to synchronize the pump and the resonant beam inside the cavity by matching the cavity length with the repetition rate of the laser pump source. This ensures that the resonant pulses inside the cavity experience gain due to the presence of the pump pulse in each round-trip. For example, for an 80 MHz repetition rate ultrafast OPO, the standing-wave cavity length should by $c/(2 \times 80 \times 10^6) = 1.87$ m, while the travelling-wave cavity length is given by $c/(80 \times 10^6) = 3.75$ m, in which c is the speed of light. Therefore, the physical length of a standing-wave cavity is half that of the round-trip cavity length and the physical length of a travelling-wave cavity is equal to the round-trip cavity length.

2.5.3. Wavelength tuning

As it was mentioned earlier, one of the main advantages of an OPO over a conventional laser source is its wavelength tunability. According to the equation

$$\frac{2\pi n_P}{\lambda_P} - \frac{2\pi n_S}{\lambda_S} - \frac{2\pi n_I}{\lambda_I} = 0 \tag{2.44}$$

the tunability of an OPO can be achieved by changing any of the physical parameters of the system, which can affect the refractive index of a nonlinear medium, while maintaining the phase-matching condition of the nonlinear optical process.

Propagation through a medium with a refractive index of n	$\begin{pmatrix} 1 & d \\ 0 & 1 \end{pmatrix}$
Thin lens of focal length, f	$\begin{pmatrix} 0 & 1 \\ \frac{-1}{f} & 0 \end{pmatrix}$
Curved mirror with effective radius of curvature, R (normal incidence)	$\begin{pmatrix} 0 & 1 \\ \frac{-2}{R} & 0 \end{pmatrix}$
Refraction at a flat surface separating two media of index, n_1 & n_2	$\begin{pmatrix} 1 & 0 \\ 0 & \frac{n_1}{n_2} \end{pmatrix}$

Table 2.2. Ray matrices.

Changing the angle of the incident pump beam relative to the optic axis of the medium, or changing the temperature of the nonlinear optical crystal by mounting it in an oven, can tune the extracted wavelengths from an OPO source. Using a tunable pump source can also produce tunable output wavelengths. For quasi-phase-matched crystals, changing the grating periods can be used for tuning the emitted wavelengths, which is known as grating tuning. Besides the above traditional methods, in the ultrafast regime, the wavelength tunability can also be achieved by varying the cavity length of the OPO [45-49].

The work presented in this thesis uses grating tuning as well as the temperature tuning. In Chapter 5, we will also present the results of our investigation on a cavity-length tuning for a 1064-nm-pumped idler-resonant OPO based on MgO:PPLN.

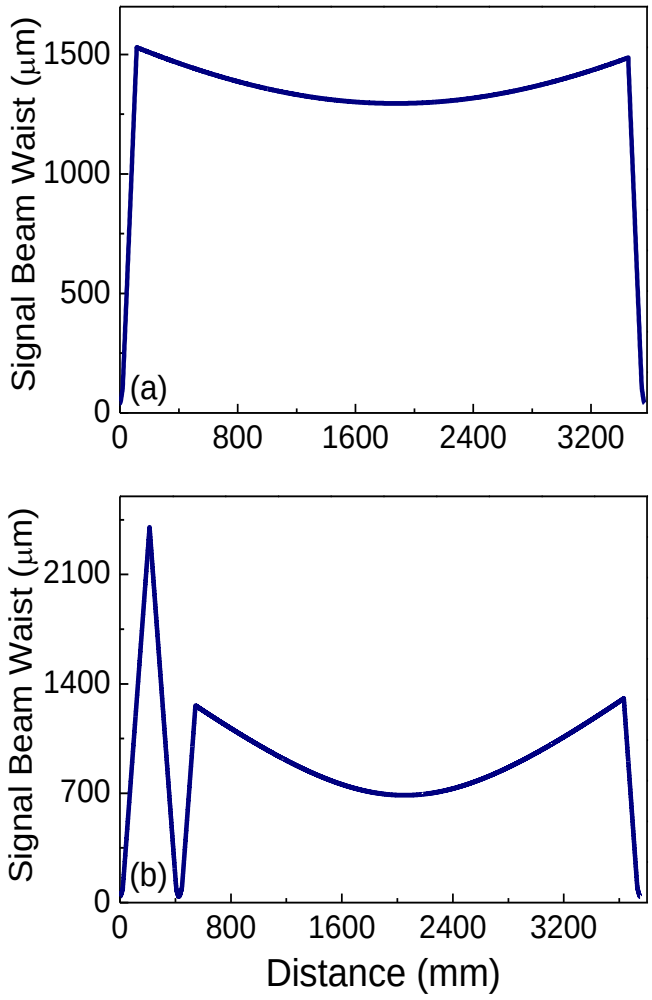

Fig. 2.11. Signal beam waist along a typical (a) ring cavity and (b) V-cavity.

A typical tuning curve for a 532-nm-pumped MgO-doped stoichiometric periodically-poled $LiTaO_3$ (MgO:sPPLT) OPO, calculated from the relevant Sellmeier equation of [52], is presented in Fig. 2.12. As it is shown in Fig. 2.12(a), changing the grating period of a MgO:sPPLT nonlinear crystal from Λ=7.88 μm to 8.61 μm, while operating at T =100ºC, the green-pumped OPO can produce tunable signal wavelengths from 800 nm to 1064 nm together with the corresponding idler wavelengths tunable from 1064 nm to 1588 nm. The same OPO, can also provide tunable output from 870 nm to 1056 nm in signal and from 1072 nm to 1369 nm in idler, by changing the temperature of the nonlinear crystal from 57.5ºC to, 194.5ºC while using a grating period of Λ=7.97 μm.

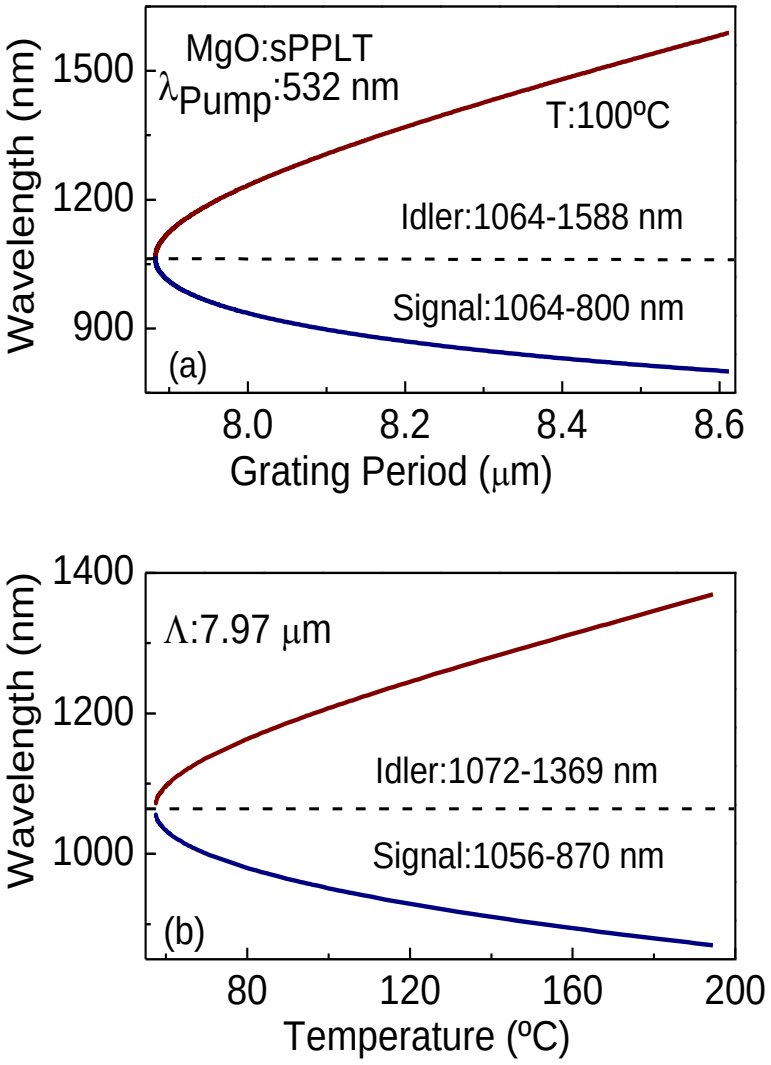

Fig. 2.12 (a) Grating tuning, and (b) temperature tuning curves for the generated signal and idler wavelengths from a 532-nm-pumped MgO:sPPLT OPO.

References

1. O. Svelto, “Principles of lasers,” (Springer, Science+Business Media, 2010).
2. E. Hecht, “Optics”, (Adison Wesley, 2002).
3. J. R. Reitz, F. J. Milford, W. Christy, “Foundation of electromagnetic theory,” (Adison Wesley, 1979).
4. J. D. Jackson, “Classical electrodynamics,” (John Wiley and sons, 1962).
5. R. W. Boyd, “Nonlinear optics,” (Academic press, 2007).
6. A. Scott, “Encyclopedia of nonlinear science,” (Taylor & Francis books, 2005).
7. Y. R. Shen, “The principle of nonlinear optics,” (Wiley, 2003).
8. G. R. Fowls, G. L. Cassiday, “Analytical mechanics,” (Brooks/Cole, 2005).
9. Y. Fainman, J. Ma, S. H. Lee, “Non-linear optical materials and applications,” Mater. Sci. Eng. R Rep. 9, 53-139 (1993).
10. K. Rottwitt, P. Tidemand-Lichtenberg, “Nonlinear optics: principles and applications,” (PRC press, 2014).
11. M. Ebrahim-Zadeh, M. H. Dunn, “Optical parametric oscillators,” Handbook of optics, 2nd ed, (Optical Society of America, Washington, D.C.), Chapter. 22 (2000).
12. C. Kittel, “Introduction to solid-state physics,” (John Wiley and sons, 2005).
13. R. L. Sutherland, “Handbook of nonlinear optics,” 2nd ed, (Marcel Dekker, Inc.1996).
14. R.W. Munn, C. N. Ironside, “Nonlinear optical materials,” (CRC Press 1993).
15. D. A. Kleinman, “Nonlinear dielectric polarization in optical media,” Phys. Rev. 126, 1977-1979 (1962).
16. J. A. Giodmaine, “Mixing of light beams in crystals,” Phys. Rev. Lett. 8, 19-20 (1962).
17. P. D. Maker, R. W. Terhune, M. Nissenoff, C. M. Savage, “Effects of dispersion and focusing on the production of optical harmonics,” Phys. Rev. Lett. 8, 21-22 (1962).
18. K. Devi, S. Parsa, M. Ebrahim-Zadeh, “Continuous-wave, single-pass, single-frequency second-harmonic-generation at 266 nm based on birefringent-multicrystal scheme,” Opt. Exp. 24, 8763-8775 (2016).
19. K. Devi, S. Chaitanya Kumar, M. Ebrahim-Zadeh, “Phase-modulation-mode-locked continuous-wave MgO:PPLN optical parametric oscillator,” IEEE Photon. J. 7, 1-9 (2015).

20. V. G. Dmitriev, G. G. Gurzadyan, D. N. Nikogosyan, "Handbook of nonlinear optical crystals," 3rd ed. (Springer 1999).
21. D. E. Zelmon, E. A. Hanning, P. G. Schunemann, "Refractive-index measurements and Sellmeier coefficients for zinc germanium phosphide from 2 to 9 μm with implications for phase matching in optical frequency-conversion devices," J. Opt. Soc. Am. B 18, 1307-1310 (2001).
22. D. S. Hum, M. M. Fejer, "Quasi-phase-matching," C. R. Physique, 8, 180-198 (2006).
23. J. A. Armstrong, N. Bloemberger, J. Ducuing, P. S. Pershan, "Interactions between light waves in a nonlinear dielectric," Phys. Rev. 127, 1918-1939 (1962).
24. G. D. Boyd, C. K. N. Patel, "Enhancement of optical second-harmonic-generation (SHG) by reflection phase-matching in ZnS and GaAs," Appl. Phys. Lett. 8, 313-315 (1966).
25. R. Haidar, "Fractional quasi-phase-matching by Fresnel birefringence," Appl. Phys. Lett. 88, 211102 (2006).
26. H. Komine, W. H. Long, J. W. Tully, E. A. Stappaerts, "Quasi-phase-matched second-harmonic generation by use of a total-internal-reflection phase shift in gallium arsenide and zinc selenide plates," Opt. Lett. 23, 661-663 (1998).
27. V. Pasiskevicius, G. Strömqvist, F. Laurell, C. Canalias, "Quasi-phase matched nonlinear media: Progress towards nonlinear optical engineering," Opt. Mater. 34, 513-523 (2012).
28. K. Kieleck, M. Eichhorn, A. Hirth, D. Faye, E. Lallier, "20-50 kHz mid-infrared OP-GaAs OPO," Proc. Conf. Lasers & Electro-Optics (CLEO), 2008. Paper CTull1.
29. P. G. Schunemann, S. D. Setzler, D. F. Bliss, D. Weyburne, "2.05-μm-laser pumped orientation-patterned gallium arsenide (OP-GaAs) OPO," Proc. Conf. Lasers & Electro-Optics (CLEO), 2005. Paper CThQ4.
30. V. Tassev, M. Snure, R. Peterson, K. L. Schepler, R. Bedford , M. Mann, S. Vangala, W. Goodhue, A. Lin, J. Harris, M. Fejer, P. Schunemann, "Progress in orientation-patterned GaP for next-generation nonlinear optical devices," Proc. of SPIE. 8604, 86040V-1 (2013).
31. M. M. Fejer, G. A. Magel, D. H. Jundt, R. L. Byer, "Quasi-phase-matched second-harmonic-generation: Tuning and tolerances," IEEE J. Quantum Electron. 28, 2631-2654 (1992).

32. S. Matsumoto, E. J. Lim, H. M. Hertz, M. M. Fejer, "Quasi-phase-matched second-harmonic-generation of blue light in electrically periodically-poled lithium tantalate waveguides," Electronics Lett. 27, 2040-2042 (1991).
33. K. Devi, S. Chaitanya Kumar, M. Ebrahim-Zadeh, "Directly phase modulation-mode-locked doubly-resonant optical parametric oscillator," Opt. Exp. 21, 23365-23375 (2013).
34. A. Esteban-Martin, G. K. Samanta, K. Devi, S. C. Kumar, M. Ebrahim-Zadeh, "Frequency-modulation mode-locked optical parametric oscillator," Opt. Lett. 37, 115-117 (2012).
35. J. Cao, D. Shen, Y. Zheng, Y. Feng, Y. Kong, W. Wan, "Femtosecond OPO based on MgO:PPLN synchronously pumped by a 532 nm fiber laser," Laser. Phys. 27, 055402 (2017).
36. S. Chaitanya Kumar, S. Parsa, M. Ebrahim-Zadeh, "Fiber-laser-based, green-pumped, picosecond optical parametric oscillator using fan-out grating PPKTP" Opt. Lett. 41, 52-55 (2016).
37. A. V. Smith, D. J. Armstrong, "Nanosecond optical parametric oscillator with 90° image rotation: design and performance," J. Opt. Soc. Am. B 19, 1801-1814 (2002).
38. W. Koechner, "Solid state lasers engineering," (Springer Science+Business Media, Inc. 2006).
39. J. A. Giordmaine, R. C. Miller, "Tunable coherent parametric oscillation in $LiNbO_3$ at optical frequencies," Phys. Rev. Lett. 14, 973-976 (1965).
40. M. Ebrahim-Zadeh, A. J. Henderson, M. H. Dunn, "An Excimer-pumped β-BaB_2O_4 optical parametric oscillator tunable from 354 nm to 2.37 μm," IEEE J. Quantum Electron. 26, 1241-1252 (1990).
41. D. Brida, C. Manzoni, G. Cirmi, M. Marangoni, S. De Silvestri, G. Cerullo, "Generation of broadband mid-infrared pulses from an optical parametric amplifier," Opt. Exp. 15, 15035-15040 (2007).
42. R.W. Munn, C. N. Ironside, "Nonlinear optical materials," (CRC Press, 1993).
43. A. M.Weiner, "Ultrafast optics," (Wiley series in pure and applied optics, 2009).
44. N. Hodson, H. Weber, "Laser resonators and beam propagations, fundamentals, advanced concepts and applications," (Springer Science+Business Media, Inc. 2005.).
45. J. Cao, D. Shen, Y. Zheng, Y. Feng, Y. Kong, W. Wan, "Femtosecond OPO based on MgO:PPLN synchronously pumped by a 532 nm fiber laser," Laser Phys. 27, 1-5, (2017).

46. C. McGowan, D. T. Reid, Z. E. Penman, M. Ebrahim-Zadeh, W. Sibbet, D. H. Jundt, "Femptosecond Optical parametric oscillator based on periodically poled lithium niobate," J. Opt. Soc. Am. B 15, 694-701, (1998).
47. J. Chung, E. Siegman, "Singly-resonant continuous-wave mode-locked $KTiOPO_4$ optical parametric oscillator pumped by a Nd:YAG laser," J. Opt. Soc. Am. B 10, 2201-2210 (1993).
48. S. Chaitanya Kumar, K. T. Zawilski, P. G. Schunemann, M. Ebrahim-Zadeh, "High-repetition-rate, deep-infrared picosecond optical parametric oscillator base don $CdSiP_2$," Opt. Lett. 42, 3606-3609 (2017).
49. S. Chaitanya Kumar, M. Ebrahim-Zadeh, "Fiber-laser-based green-pumped picosecond MgO:sPPLT optical parametric oscillator," Opt. Lett. 38, 5349-5352 (2013).
50. O. Paul, A. Quaosig, T. Bauer, M. Nittmann, J. Bartschke, G. Anstett, J. A. L'Huillier, "Temperature-dependant Sellmeier equation in the MIR for the extraordinary refractive index of 5% MgO doped congruent $LiNbO_3$," Appl. Phys. B 86, 111-115 (2007).
51. K. Fradkin, A. Arie, A. Skliar, G. Rosenman, "Tunable mid-infrared source by difference frequency generation in bulk periodically poled $KTiOPO_4$," Appl. Phys. Lett. 75, 914-916 (1999).
52. A. Bruner, D. Eger, M. B. Oron, P. Blau, M. Katz, S. Ruschin, "Temperature-dependent Sellmeier equation for the refractive index of stoichiometric lithium tantalite," Opt. Lett. 28, 194-196 (2003).

Chapter 3

Rapidly tunable picosecond optical parametric oscillator for the near-infrared

This chapter constitutes the following publication:

Fiber-laser-based, green-pumped, picosecond optical parametric oscillator using fan-out grating PPKTP

S. Chaitanya Kumar, **S. Parsa**, and M. Ebrahim-Zadeh,

Optics Letters **41**(1), 52-55 (2016)

(TOP-10 downloaded articles, OSA's re-cap of the year's most downloaded, 2016)

3.1 Motivation

Tunable coherent ultrashort pulses in the near-infrared (NIR) spectral region are widely used in coherent anti-Stokes Raman scattering (CARS) spectroscopy and microscopy [1-4]. Also, many optical devices for telecommunication widely benefit from tunable coherent NIR sources [5]. Dye lasers together with some solid-state lasers, such as chromium lasers, can generate coherent emissions in ~700 nm to 2000 nm, but their wavelength tunability is limited [6], Fig. 1.1. Although Ti:sapphire laser, with exceptionally wide tuning range from 650-1100 nm, has been used as a commercially available workhorse for the NIR region [7-9], more economic and compact alternatives, which can cover the desired wavelength spectra in the NIR were always pursued.

In order to cover NIR spectral region with coherent wavelengths, optical parametric oscillators (OPOs) are ideal choices as they can generate widely tunable, stable and synchronized output beams with high conversion efficiencies. Such OPOs are typically pumped in the green, depending on second-harmonic-generation (SHG) of mode-locked Neodymium (Nd)-based solid-state or Ytterbium-fiber (Yb-fiber) lasers [10].

Previously, green-pumped OPOs have relied on birefringent nonlinear optical crystals in order to generate tunable wavelengths in the NIR spectral region. Using a 30-mm-long, noncritical phase-matched Brewster-angled LiB_3O_5 (LBO) crystal, a picosecond temperature-tuned OPO across 740-930 nm in the signal and 1240-1890 nm in the idler at the repetition rate of 80 MHz was demonstrated [11]. The highest signal output power from a picosecond green-pumped OPO based on a 30-mm-long noncritical phase-matched LBO crystal was reported to be ~22 ps signal pulses of ~1.6 W, tunable across 744-930 nm, with a total output power conversion efficiency of 60% [12].

In the mentioned reports, either limited tuning range or low output power due to the moderate values of the effective nonlinearity of the used crystals was achieved through the parametric process. The advent of quasi-phase-matched (QPM) nonlinear materials, which offer high nonlinearity and long interaction lengths, has paved the way of approaching higher output powers along with broader tunability. Picosecond pulses at 80 MHz, tunable in the 890-1320 nm, were generated from a synchronously-pumped OPO based on a 10.8-mm-long periodically-poled KTP (PPKTP) crystal with a single grating period of Λ=8.99 μm [13]. Picosecond OPO based on a MgO-doped periodically-poled $LiNbO_3$ (MgO:PPLN) crystal with five gratings ranging in period from Λ=6.7 μm to 7.1 μm, kept in an oven at T=200^{o}C, and pumped by 20 ps green pulses at the repetition rate of 230 MHz, was also reported [14]. The source produced ~165 mW (signal at 840 nm) and ~107 mW (idler at 1420 nm) for a pump average power of ~1 W and it was tunable from ~800 nm to 900 nm in the signal and from 1280 nm to 1540 nm in the idler. However, the results from this work indicated that MgO:PPLN is not a suitable nonlinear material for visible pumping, since the crystal was physically damaged after about 30 minutes of operation, while pumping at 2 W. Using a 30-mm-long MgO-doped stoichiometric periodically-poled $LiTaO_3$ (MgO:sPPLT) with a single grating period of

Λ=7.97 μm as a nonlinear crystal, a 532-nm-pumped OPO was reported, generating stable, high-power and high-repetition-rate signal and idler wavelengths tunable across 874-1008 nm and 1126-1359 nm, respectively [15].

Although all these sources can provide high average power, the ability to power scale green-pumped picosecond OPOs together with rapid tuning has been challenging. While power scaling in OPOs depends on the available pump power and optimization of the output coupling, rapid tuning relies on the properties of the nonlinear material itself. As in all the mentioned studies, wavelength tuning has been achieved either by varying the temperature of the nonlinear medium, which is a relatively slow process, or by only changing the grating periods of the nonlinear crystal, which results in discontinuous wavelength tuning, or through rotating the birefringent crystal, which is limited by the aperture of the nonlinear crystal. Hence, it is worthwhile to investigate various QPM nonlinear materials with advanced grating design in combination with compact fiber-based pump lasers to develop high-power, fast and broadly tunable OPOs in the NIR wavelength region [16]. A fan-out grating designed nonlinear optical crystal opens up new ways to realize such sources and can broaden the spectral coverage especially for those nonlinear materials which cannot be temperature-tuned [17].

In this chapter, we demonstrate a stable, high-repetition-rate picosecond OPO based on a fan-out designed grating periods in PPKTP crystal. The fan-out grating of the PPKTP crystal provides rapid grating tuning by only translating the nonlinear crystal across the pump beam, while operating close to room temperature. The OPO, which is synchronously pumped by a mode-locked frequency-doubled Yb-fiber laser in the green at 532 nm, can provide continuous tuning over 749-962 nm in the signal together with the corresponding idler wavelengths tuning across 1189-1838 nm, resulting in a total signal plus idler wavelength coverage of 862 nm by grating tuning at room temperature. A maximum average power of 572 mW at 749 nm in the signal and 306 mW at 1341 nm in the idler have been achieved. The extracted signal at 765 nm and idler at 1747 nm exhibit excellent passive power stability better than 0.47%rms and 0.8%rms, respectively, over 1 hour with good beam quality in TEM_{00} mode profile. The output signal pulses have a Gaussian temporal duration of 13.7 ps, with a FWHM spectral

bandwidth of ~3.2 nm at ~80 MHz repetition rate. We also present the results of our investigations on the power scaling limitations of the OPO due to the material properties of PPKTP.

To the best of our knowledge, this is the first report on a picosecond OPO based on a PPKTP crystal using a fan-out grating design.

3.2 Experimental setup

The schematic of the experimental setup is shown in Fig. 3.1(a). The primary pump source is a mode-locked Yb-fiber laser (Fianium, FP1060-20) delivering up to ~20 W of average power in 20 ps pulses at 80 MHz repetition rate. The source operates at a central wavelength of 1064 nm and has a double-peak spectrum with a full-width at half-maximum (FWHM) spectral bandwidth of 1.4 nm. A Faraday isolator at the output end of the fiber protects the laser from any back-reflections. The output power from the laser is adjusted by using a combination of a half-wave plate and a polarizing beam-splitter cube. A second half-wave plate is used to obtain the required polarization for phase-matching during the frequency conversion process in the nonlinear crystal.

The pump for the OPO is achieved through single-pass SHG in a 30-mm-long LBO crystal with an aperture of 3×4 mm^2. The LBO crystal is cut at θ=90° and ϕ=0° for type-I ($oo \rightarrow e$) noncritical phase-matching in the optical *x*-*y* plane. The end faces of the LBO crystal are antireflection (AR)-coated (R<0.1%) at 1064 and 532 nm. The crystal is mounted in an oven with the temperature stability of ±0.1°C at the phase-matching temperature of 148.2°C. The fundamental beam is focused at the centre of the crystal to a waist radius of w_o~34 μm ($1/e^2$-intensity), corresponding to a focusing parameter of ξ~2.74 [20], to provide a SH output at 532 nm. The picosecond green source provides up to 9 W of average power at 532 nm in ~16.2 ps pulses at ~80 MHz repetition rate, with a FWHM spectral bandwidth of 0.6 nm [19]. It exhibits passive output power stability better than 0.5%rms over 16 hours in TEM_{00} spatial mode with beam pointing stability better than 12 mrad over 1 hour.

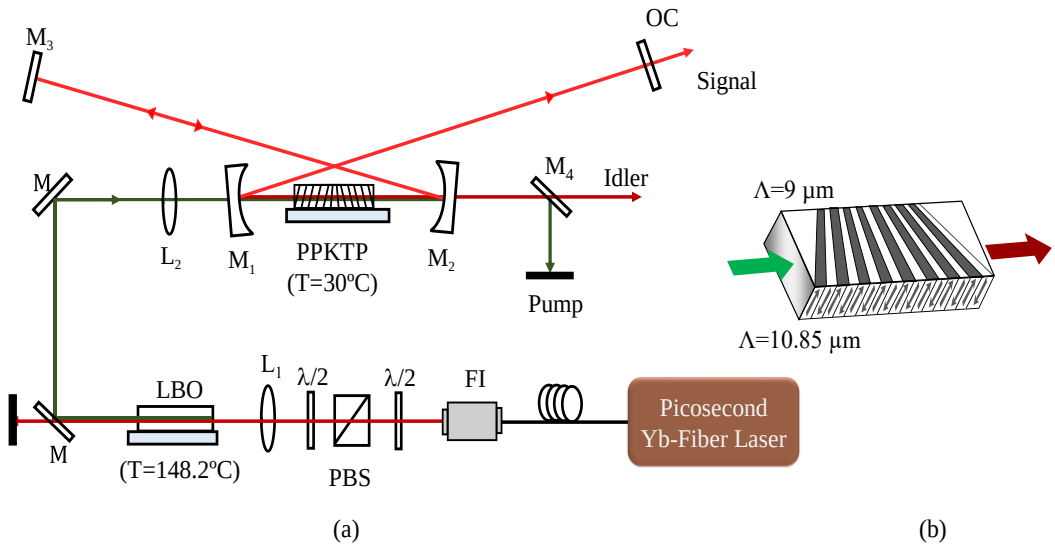

Fig. 3.1. (a) Schematic of the experimental setup for the green-pumped PPKTP OPO. FI, Faraday isolator; λ/2, half-wave plate; PBS, polarizing beam-splitter; L, lens; M, mirror; OC, output coupler. (b) Exaggerated view of the fan-out pattern on the PPKTP crystal with Λ=9-10.85 μm.

The nonlinear crystal for the OPO is a 30-mm-long, 1-mm thick, and 11-mm-wide aperture PPKTP crystal with grating periods ranging from Λ=9 μm to 10.85 μm across the 11-mm-width in a fan-out grating design. The crystal end faces are AR-coated for high transmission at 532 nm, R<0.5% for 720-990 nm and R<5% over 1130-2040 nm. The nonlinear material is housed in an oven with adjustable temperature from room temperature to 200°C with the stability of ±0.1°C for type-0 ($ee \rightarrow e$) phase-matching. The schematic of the fan-out pattern on the PPKTP nonlinear optical crystal is shown in Fig. 3.1(b).

The OPO is configured in a standing-wave X-cavity with two plano-concave mirrors, M_1-M_2 (r=150 mm), a plane mirror, M_3, and a plane output coupler (OC). All mirrors are highly transmitting for the pump (T>98%) at 532 nm and the idler wavelengths (T>95%) over 1100-2100 nm and highly reflecting (R>99%) for the signal over 700-1000 nm, which ensure singly-resonant signal oscillation. A plane OC with varying transmission of T~31%-40% over 750-965 nm is used to partially extract the signal power from the OPO. A dichroic mirror, M_4, separates the generated idler from the transmitted pump after M_2. The total optical length of the OPO cavity is ~3.75 m, corresponding to a

repetition rate of ~80 MHz, ensuring synchronization of the resonant signal with the pump laser repetition rate.

3.3 Design and optimization of the cavity

In order to optimize the performance of the OPO, we used a focusing parameter [18],

$$\xi = \frac{l_{crystal}}{b_P} \tag{3.1}$$

in which $l_{crystal}$ is the length of the nonlinear medium, and b_P is the confocal parameter of the pump, defined as

$$b_P = k_P w_{oP}^2 \tag{3.2}$$

with the pump wave-vector, $k_P = (2\pi n_P)/\lambda_P$. In Eq. 3.2, n_P is the refractive index of the material at the pump wavelength of 532 nm, λ_P is a wavelength of the pump source, and w_{oP} is the beam waist radius of the pump at the centre of the nonlinear optical crystal.

In this experiment, the pump beam is confocally focused to a waist radius of w_{oP}~63 μm, corresponding to a focusing parameter of ξ~0.33, at the centre of the nonlinear crystal. The cavity design ensures optimum overlap between the pump and the resonant signal at the centre of the PPKTP crystal, $b_P = b_S$, which results in a signal waist radius at λ_S= 915 nm to be w_{oS}~83.8 μm.

Another important parameter, which should be considered in order to have an efficient OPO source is the spectral acceptance bandwidth of the nonlinear optical crystal for the pump wavelength. In Fig 3.2(a) is shown a normalized parametric gain as a function of the pump wavelengths for a 30-mm-long PPKTP using the relevant Sellemier equation [20], which represents a parametric gain bandwidth of 0.04 nm. The small spectral acceptance bandwidth of the crystal compared to the FWHM spectral bandwidth of 0.6 nm for the green pump is a limiting factor for achieving efficient NIR OPO source. On the other hand, we calculated the group velocity mismatch (GVM) between the pump and resonant signal, with the results shown in Fig 3.2(b). In the present experiment, ~16 ps pump pulses can support a crystal lengths up to 24 mm. The long effective length together

with a moderately high PPKTP effective nonlinearity, d_{eff}~10 pm/V, can compensate for the small parametric gain bandwidth and then result in an efficient NIR output.

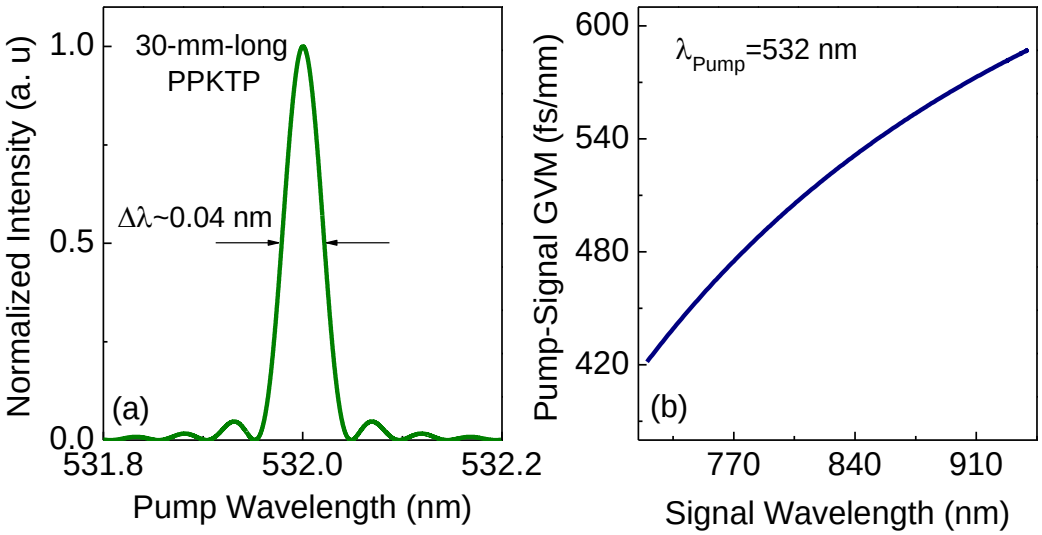

Fig. 3.2. (a) Parametric gain bandwidth for a 30-mm-long PPKTP crystal. (b) Group velocity mismatch between the pump at 532 nm and the resonant signal inside a high-repetition-rate picosecond PPKTP-based OPO as a function of the signal wavelengths.

3.3 Results and discussion

3.3.1 Transmission measurements

PPKTP is a ferroelectric nonlinear optical material, which has a transparency range from ~350 nm to ~4500 nm with an effective nonlinearity of d_{eff} ~10 pm/V, and small thermal conductivity of ~3 W. $m^{-1}.K^{-1}$. PPKTP has high absorption in the green, due to some impurities and defects leading to a linear absorption [21]. The high absorption also is attributed to specific bandgap properties of the crystal, which makes it susceptible of two-photon absorption (TPA).

In order to investigate the behaviour of the PPKTP crystal when pumped by high-repetition-rate picosecond pulses at 532 nm, and to study the possible roles of linear absorption and TPA, we performed transmission measurements for the 30-mm-long crystal at the temperature of 30°C.

The green pump beam was arranged in an extraordinary polarization for these measurements, as required for the phase-matching in the OPO. Initially, we focused the beam to a waist radius of w_o~40 μm at the centre of the PPKTP crystal. The variation of the transmission as a function of the input green intensity and the corresponding average power is shown in Fig. 3.3(a). As the input green average power is increased from the minimum up to 2 W, corresponding to an input intensity of ~30 MW/cm^2, we observe a drop in the transmission from 95.4% to 81.2%, considering the 0.5% AR-coating losses at 532 nm on both faces of the nonlinear crystal. This is an evident sign of nonlinear behaviour inside the crystal. Using a simple two-photon absorption model, we fitted the experimentally measured data from which we obtained a linear absorption coefficient, α=0.01 cm^{-1}, and a TPA coefficient to be β=1.67 cm/GW. The obtained value for TPA coefficient is significantly different from those reported earlier, ~0.1 cm/GW [22,23], which can be attributed to the use of high-repetition-rate pulses at high average power in this study. Further, we relaxed the green beam waist to w_o~63 μm at the centre of the PPKTP crystal and performed the similar measurements, with the results shown in Fig. 3.3(b). However, in this case, we were not able to increase the input average green power beyond 2.4 W, at which we observed a bulk damage in the PPKTP crystal. Although this damage was not catastrophic, we were not able to use the crystal at this position any longer. Since in this case, the damage occurred at an input green intensity of ~15 MW/cm^2, which is only 50% of the intensity used in the previous case in Fig. 3.3(a) with the green beam waist of w_o~40 μm, we can conclude that the cause of the damage is related to the average power and not to the intensity. The results also confirm that unlike continuous-wave regime (cw), where high cw powers in the green can be generated by a PPKTP nonlinear crystal and only the intrinsic linear absorption especially in the green, itself, limits the amount of extracted power [24,25], in the case of high-repetition-rate picosecond operation power scaling of the material is limited by the optical damage and the dominant role of TPA. As such, to avoid any further damage to the crystal, we limited the input average green power to a maximum of ~1.6 W for pumping the OPO.

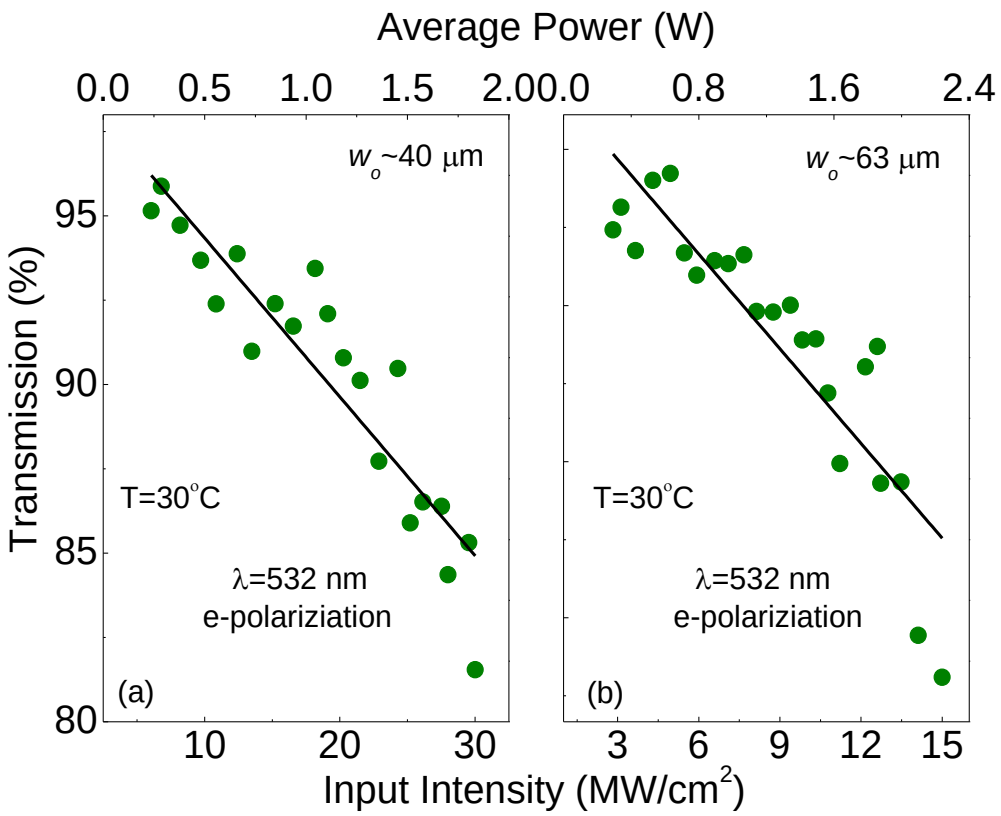

Fig. 3.3. (a) Variation of the transmission of the 30-mm-long PPKTP pumped by a 532 nm green beam at the beam radius of (a) ~40 μm, and (b) ~63 μm, as a function of average input pump power and the corresponding intensity.

3.3.2 Wavelength tuning

In order to characterize the picosecond PPKTP-based OPO, we initially investigated the wavelength tuning performance by changing the temperature of the crystal for a fixed grating period at low input power. For a grating period of Λ=9.09 μm by changing the temperature of the PPKTP crystal from 30°C to 140°C, we were able to tune the OPO from 883 nm to 950 nm in the signal wavelength with the absolute tuning rate of ~0.6 nm/°C together with the corresponding idler wavelengths tuning from 1209 nm to 1338 nm, as it is shown in Fig. 3.4(a). The solid circles are the experimental data, while the solid and dashed curves correspond to the theoretical calculations using two different Sellemier equations [20,26]. The signal wavelengths were measured by using a spectrometer, while the idler wavelengths were calculated from energy conservation. As

it is evident from Fig. 3.4(a), better agreement between the experimental data and the calculations was found by using the Sellemier equation from Ref. [20], which is presented as

$$n^2 = A + \frac{B}{1 - (C/\lambda^2)} + \frac{D}{1 - (E/\lambda^2)} - F\lambda^2 \qquad (3.3)$$

where λ is a wavelength given in microns and the parameters, *A*-*D*, are as below

A	2.12725
B	1.18431
C	5.14852×10^{-2} (μm^2)
D	0.6603
E	100.00507 (μm^2)
F	9.68956×10^{-3} (μm^{-2})

The temperature-dependent refractive index, by using Eq. (3.3), is given by

$$n(t) = n + \left((a\lambda^{-3}) + (b\lambda^{-2}) + \frac{c}{\lambda} + 2.1151\right) \times (t - t_0)10^{-5} \qquad (3.4)$$

with

a	0.3896 (μm^3/^{o}C)
b	1.3332 (μm^2/^{o}C)
c	2.2762 (μm/^{o}C)
t_0	25 (^{o}C)

We also performed grating period tuning for the OPO by translating the PPKTP crystal across the pump beam while operating at room temperature. We were able to continuously tune the OPO over 749-962 nm in the signal together with the idler wavelengths across 1189-1838 nm, as shown in Fig. 3.4(b). The dashed curves, which represent the theoretical calculations by using the Sellemier equation of Ref. [20], show excellent agreement with the experimental data, which are represented in solid circles. As it is clear from Fig. 3.4(b), faster tunability with the absolute rate of ~151.4 nm/μm has been achieved by changing the grating periods of the PPKTP crystal while operating at a fixed temperature.

3.3.3 Signal and idler power scaling

We further characterized the OPO by performing the power scaling measurements for the output. At a fixed temperature of 30^{o}C and for an output coupler of ~26%, we extracted as much as 556 mW of average signal power at 765 nm together with 185 mW of idler at 1747 nm, for an input pump power of ~1.6 W. The results in Fig. 3.5(a) show that the source can provide up to ~741 mW of overall average power corresponding to ~46% overall extraction efficiency. The slope efficiencies for the signal and idler power were estimated to be ~44% and 15%, respectively. In this case, the threshold for the OPO was measured to be ~340 mW and the maximum pump depletion of ~69.7% was recorded.

In a separate experiment, we performed the same measurement for the signal wavelength at 915 nm and the corresponding idler at 1271 nm, with the identical output coupling of ~26%. Figure 3.5(b) represents the experimental data for this measurement. At this wavelength, with the maximum input power of 1.55 W, as much as 505 mW of signal power together with 307 mW of idler power were extracted from the OPO, corresponding to 52% of overall extraction efficiency. The estimated slope efficiencies were 40% and 25% for the signal and the idler, respectively, and the measured threshold pump power was ~280 mW, while more than 60% of pump depletion was recorded.

Since no saturation was observed in these cases, there is a possibility of further power scaling. However, the usable maximum pump power is currently limited by the material quality, as explained in Section 3.3.1.

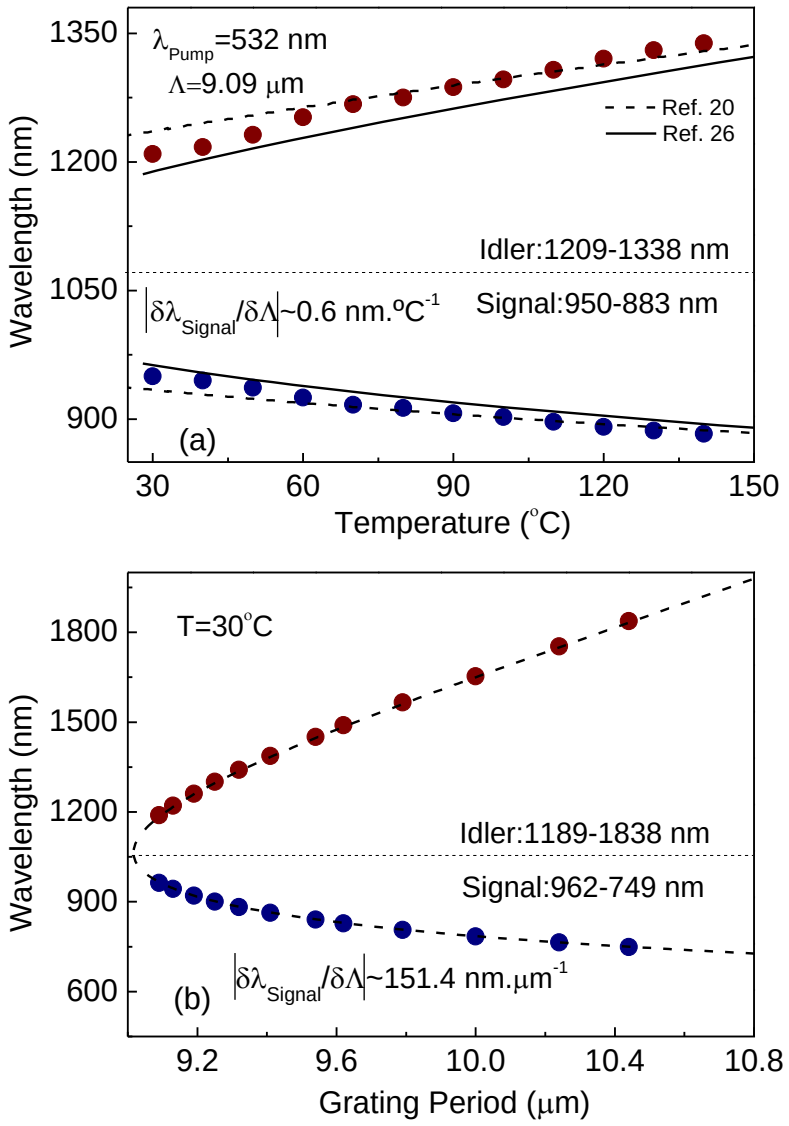

Fig. 3.4. (a) Temperature tuning for Λ=9.09 μm, and (b) grating tuning tuning curves at the fixed temperature of 30 ºC, for a green-pumped picosecond PPKTP OPO.

3.3.4 Extracted signal and idler power across the tuning range

The simultaneously measured signal and idler average power together with the overall extraction efficiency and the pump depletion across the wavelength tuning range of the PPKTP-based OPO were also recorded. For a fixed input pump power of ~1.5 W, and using an OC with a varying transmission of T~31%-40% across the signal tuning range, we were able to extract an average signal power ranging from 544 mW at 750 nm to 456

mW at 965 nm, with a maximum signal average power of 572 mW at 749 nm, as shown in Fig. 3.6. Also shown in Fig. 3.6 is the OPO can provide an overall extraction efficiency up to 53% at a signal wavelength of 900 nm, while remaining >39% across the tuning range. Also shown in the inset of Fig. 3.6 is the transmission of the OC across the signal tuning range, varying from 31% at 750 nm to ~40% at 963 nm.

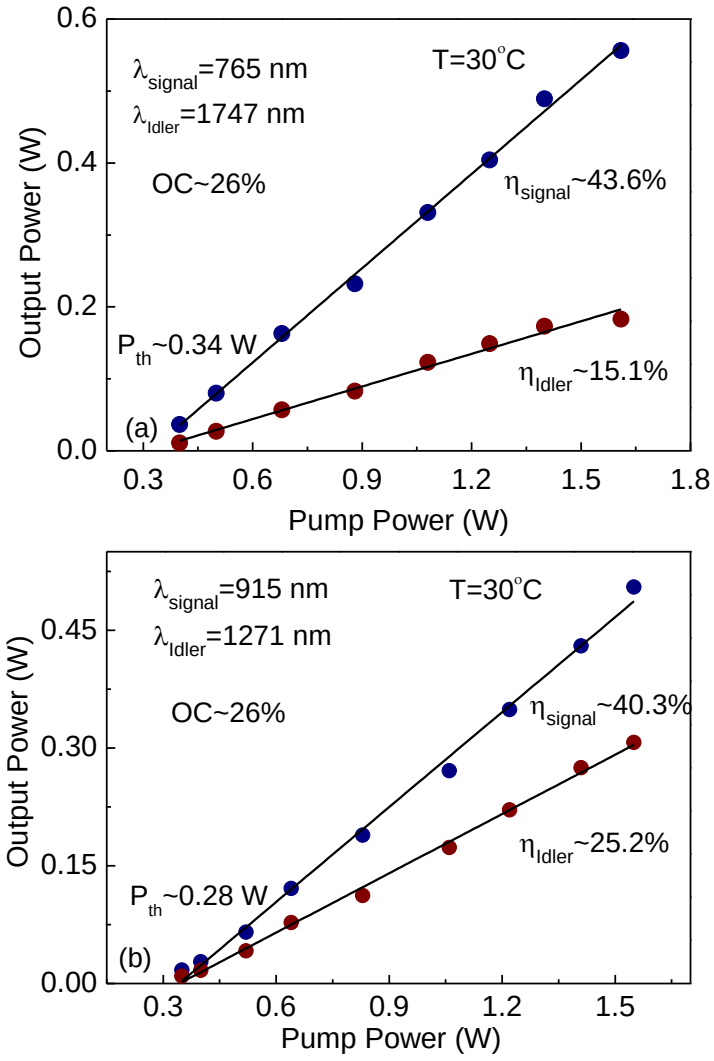

Fig. 3.5. (a) Power scaling measurement for the signal wavelength of 765 nm and the corresponding idler. (b) Extracted signal (915 nm) and idler (1271 nm) average power as a function of the input power.

In Fig. 3.7 is shown the corresponding idler power varying from 250 mW at 1189 nm to 113 mW at 1838 nm with a maximum idler average power of ~306 mW at 1341 nm. According to Fig. 3.7, maximum pump depletion of >86% is recorded at the generated idler wavelength of 1341 nm, and maintains >48% over the entire tuning range.

It should be noted that the data presented here are not corrected for any AR coating or transmission losses of the crystal and mirror coatings.

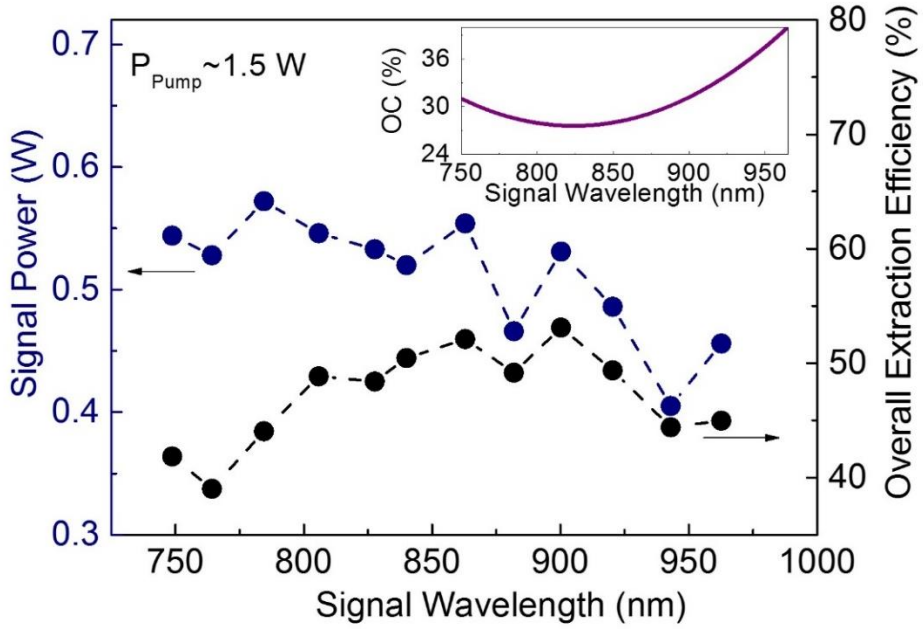

Fig. 3.6. Signal power and the overall extraction efficiency across the signal tuning range. Inset: Transmission of the OC across the signal tuning range.

3.3.5 Power stability and beam quality

In order to characterize the long-term stability of the extracted powers, we simultaneously recorded the maximum signal and idler powers at the wavelengths of 765 nm and 1747 nm, respectively. The results presented in Fig. 3.8 show that the OPO can generate signal and idler wavelengths with passive power stability better than 0.47%rms and 0.8%rms, respectively, over a period of 1 hour while the pump power stability better than 0.8%rms was recorded over the same period of measurement.

The far-field energy distribution of the extracted signal beam at 750 nm together with the corresponding idler beam profile at 1830 nm is shown in Fig. 3.9. The signal beam profile was taken by using a silicon-based CMOS camera and the idler beam profile was recorded using a pyroelectric camera. Both beams were confirmed to exhibit TEM_{00} spatial profiles with single-peak Gaussian distributions at maximum output power.

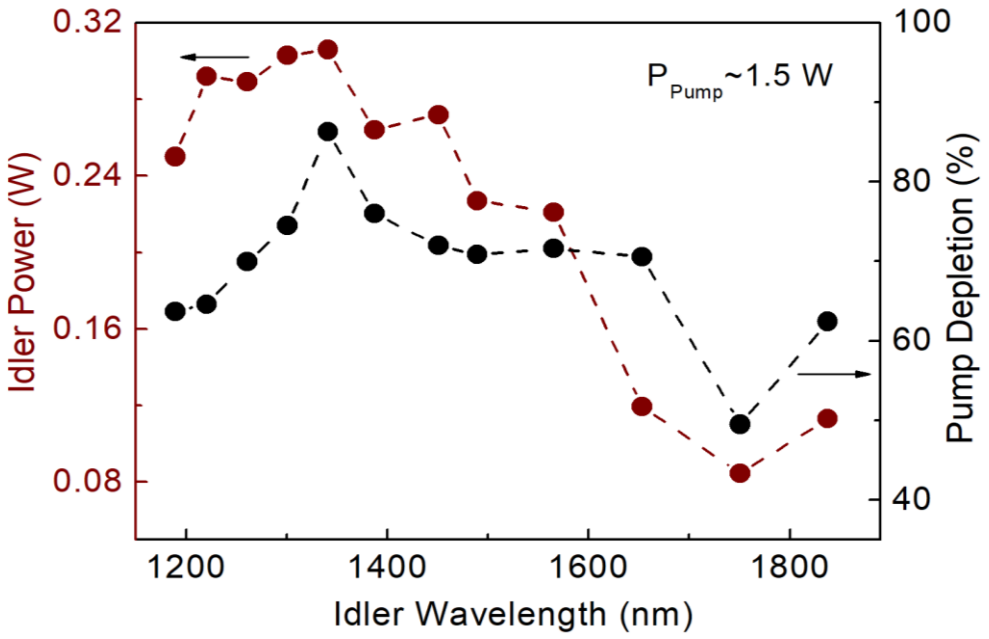

Fig. 3.7. Idler power and pump depletion across the idler tuning range.

3.3.6 Signal wavelengths temporal and spectral characterization

Further, we performed spectral and temporal characterization of the signal pulses extracted from the picosecond PPKTP green-pumped OPO at maximum output power. The long-term stability of the signal spectrum, while operating at a central wavelength of 765 nm, shown in Fig. 3.10(a). The signal exhibits high spectral stability with a small double-peak feature in the spectrum, as presented in the inset of Fig. 3.11. The corresponding FWHM signal bandwidth is stable to better than 2.3%rms over 1 hour at about 3.4 nm, as shown in Fig. 3.10(b).

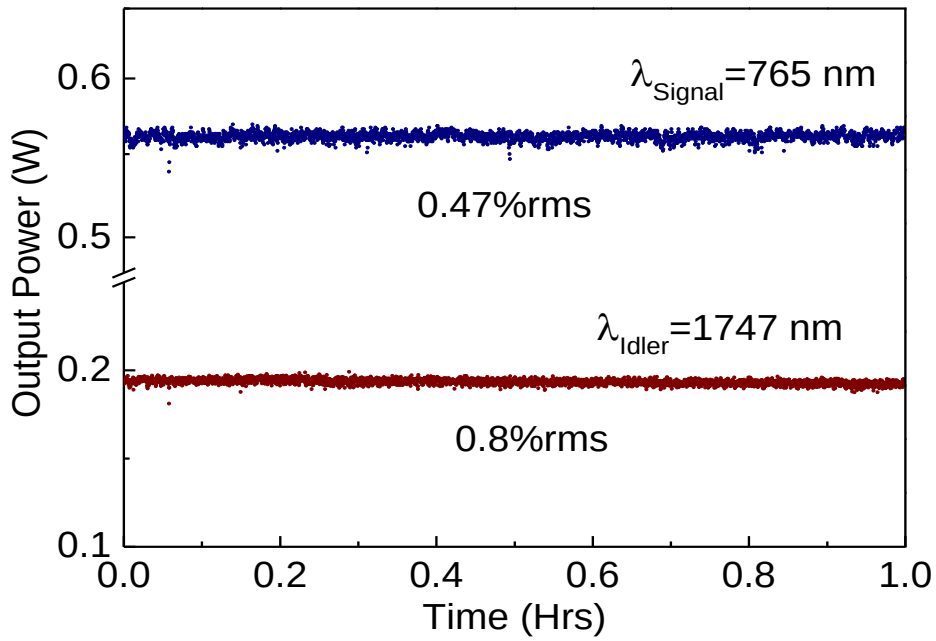

Fig. 3.8. Power stability measurements for the extracted signal and idler wavelengths at 765 nm and 1747 nm, respectively, over 1 hour.

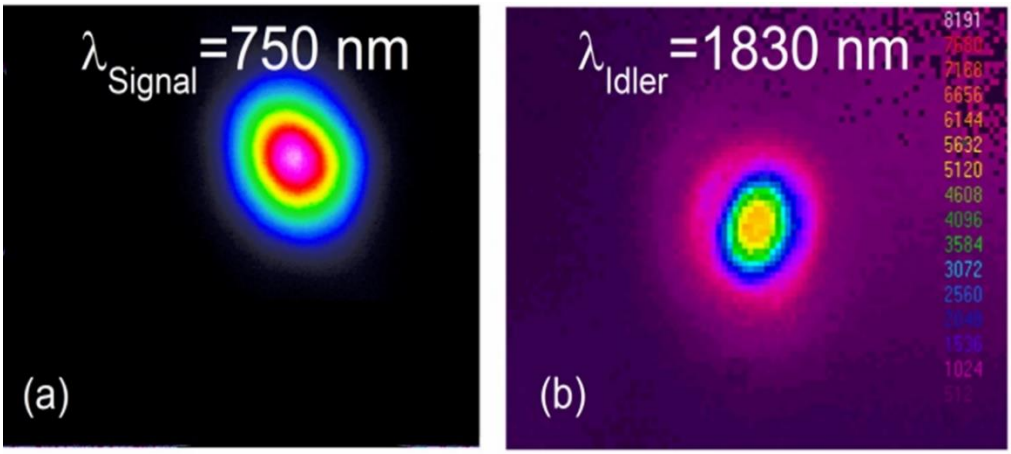

Fig. 3.9. Far-field energy distribution of the extracted (a) signal at 750 nm, and (b) the corresponding idler at 1830 nm.

Temporal characterization of the signal pulses from the OPO was performed by using a home-made autocorrelation based on a two-photon detector. Figure 3.11 shows a typical interferometric autocorrelation trace, resulting in a FWHM pulse width of 19.4 ps, corresponding to a Gaussian pulse duration of 13.7 ps. The corresponding spectrum with

a FWHM bandwidth of 3.2 nm centred at 765 nm is shown in the inset of Fig. 3.11. These measurements result in a time-bandwidth product of $\Delta\tau\Delta\vartheta$~24 in the absence of dispersion compensation compared to a time-bandwidth product of $\Delta\tau\Delta\vartheta$~10.3 of the pump. Implementing intracavity dispersion compensation could further improve the time-bandwidth product of the generated output pulses from the OPO.

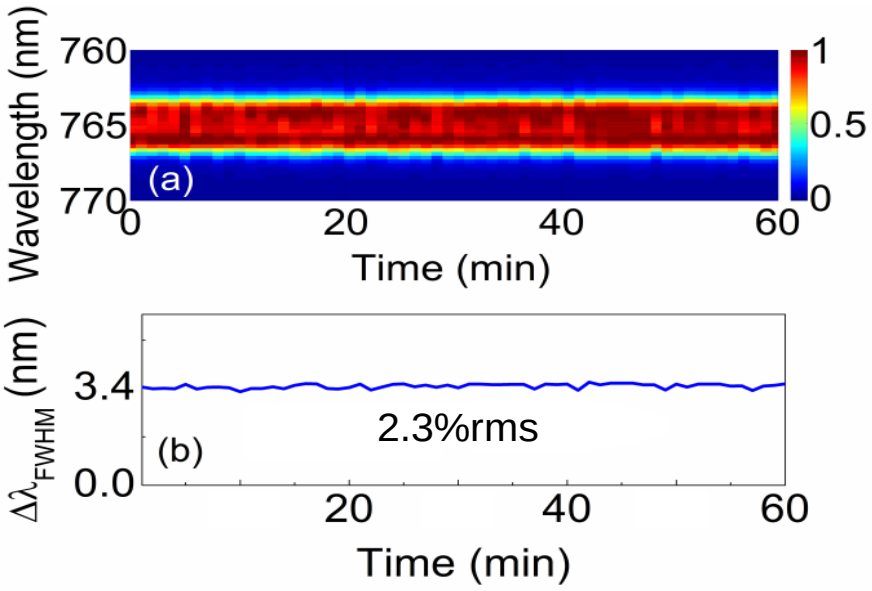

Fig. 3.10 (a) Long-term signal spectral stability at 765 nm, and (b) the corresponding FWHM signal bandwidth stability over 1 hour.

3.4 Conclusion

In this chapter, we have described a compact picosecond singly-resonant OPO based on PPKTP crystal, synchronously pumped by a 80 MHz pulses at 532 nm. The fan-out structured grating period of this crystal offers rapid tunability for the extracted signals and idler wavelengths in the NIR spectral region close to the room temperature. The generated signal and idler wavelengths are continuously tunable across 749-962 nm and 1189-1838 nm, respectively. The maximum signal power of 572 mW was achieved at the signal wavelength of 749 nm, while the OPO was pumped at ~1.5 W. The source provides an overall extracted efficiency >41% and the pump depletion >48% over the entire tuning range. The extracted signal at the wavelength of 765 nm shows passive power stability better than 0.47%rms compared to 0.8%rms of the green pump power stability over 1

hour of measurement. In the absence of dispersion control, the signal pulses extracted from the OPO have a Gaussian temporal duration of 13.7 ps measured at 765 nm with a FWHM bandwidth of 3.2 nm, resulting in a time-bandwidth product of $\Delta\tau\Delta\vartheta$~24. The signal FWHM bandwidth stability measurement at 765 nm over 1 hour shows the stability better than 2.3%rms.

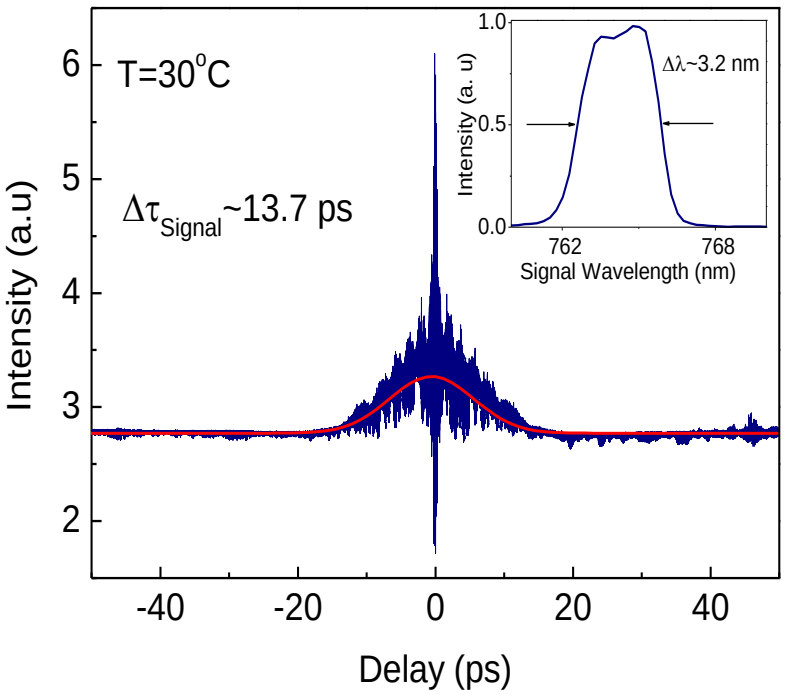

Fig. 3.11. Autocorrelation trace of the extracted signal pulses at 765 nm. Inset: Corresponding signal spectrum.

Measurements of the green pump transmission in the PPKTP crystal have been performed, placing a limitation on the power scaling of the OPO beyond 2.4 W of average pump power due to bulk damage in the material with the damage mechanism identified as being dependent on the average power. The overall extraction efficiency of the present device could potentially be improved by optimizing the output coupling at the current pumping level [27].

The results confirm that the described compact synchronously-pumped OPO is a viable and reliable source of emitting high-power, stable, fast and continuously tunable

picosecond radiation in the NIR spectral region, which is very useful in advanced microscopy and spectroscopy.

References

1. C. Cleff, J. Epping, P. Gross, C. Fallnich, "Femtosecond OPO based on LBO pumped by a frequency-doubled Yb-fiber laser-amplifier system for CARS spectroscopy," Appl. Phys. B: Lasers Opt. 103, 795-800 (2011).
2. C. L. Evans, E. O. Potma, M. Puoris'haag, D. Côté, C. P. Lin, X. S. Xie, "Chemical imaging of tissue in vivo with video-rate coherent anti-Stokes Raman scattering microscopy," Proc. Natl. Acad. Sci. U.S.A. 102, 16807-16812 (2005).
3. A. Zumbusch, G.R. Holtom, X.S. Xie, "Three-Dimensional Vibrational Imaging by Coherent Anti-Stokes Raman Scattering," Phys. Rev. Lett. 82, 4142-4145 (1999).
4. C. W. Freudiger, W. Min, B. G. Saar, S. Lu, G.R. Holtom, C. He, J. C. Tsai, J. X. Kang, X. S. Xie, "Label-Free Biomedical Imaging with High Sensitivity by Stimulated Raman Scattering Microscopy," Science 322, 1857-1860 (2008).
5. T. Sueta, T. Okoshi, "Ultrafast and Ultra-parallel Optoelectronics," (Wiley, New York, 1995).
6. W. Koechner, "Solid state lasers engineering," (Springer Science+Business Media, Inc. 2006).
7. J. X. Cheng, X. Su. Xie, "Coherent Anti-Stokes Raman Scattering Microscopy: Instrumentation, Theory, and Applications," J. Phy. Chem. B 108, 827-840 (2004).
8. G. W. H. Wurpel, J. M. Schins, M. Müller, "Chemical specificity in three-dimensional imaging with multiplex coherent anti-Stokes Raman scattering microscopy," Opt. Lett. 27, 1093-1095 (2002).
9. J. X. Cheng, A. Volkmer, L. D. Book, X. S.Y Xie, "Multiplex Coherent Anti-Stokes Raman Scattering Microspectroscopy and Study of Lipid Vesicles," J. Phys. Chem. B 106, 8493-8498 (2002).
10. S. Chaitanya Kumar, M. Ebrahim-Zadeh, "High-power, fiber-pumped picosecond green source based on BiB_3O_6," Laser. Phys. 24, 025401 (2014).
11. M. Jurna, J. P. Korterik, H. L. Offerhaus, "Noncritical phase-matched lithium triborate optical parametric oscillator for high resolution coherent anti-Stokes Raman scattering spectroscopy and microscopy," Appl. Phys. Lett. 89, 2511161-2511163 (2006).

12. T. W. Tukker, C. Otto, J. Greve, “Design, optimization, and characterization of a narrow-bandwidth optical parametric oscillator,” J. Opt. Soc. B 16, 90-95 (1999).
13. F. Ganikhanov, S. Carrasco, X. S. Xie, M. Katz, W. Seitz, D. Kopf, “Broadly tunable dual-wavelength light source for coherent anti-Stokes Raman scattering microscopy,” Opt. Lett. 31, 1292-1294 (2006).
14. F. Kienle, D. Lin, S. Alam, H. S. S. Hung, C. B. E. Gawith, H. E. Major, D. J. Richardson, D. P. Shepherd, “Green-pumped, picosecond MgO:PPLN optical parametric oscillator,” J. Opt. Soc. B 29, 144-152 (2012).
15. S. Chaitanya Kumar, M. Ebrahim-Zadeh, “Fiber-laser-based green-pumped picosecond MgO:sPPLT optical parametric oscillator,” Opt. Lett. 38, 5349-5352 (2013).
16. V. Pruneri, J. Webjörn, P. St. J. Russell, D. C. Hanna, “532 nm pumped optical parametric oscillator in bulk periodically-poled lithium niobate,” Appl. Phys. Lett. 67, 2126 (1995).
17. P. E. Powers, T J. Kulp, S. E. Bisson, “Continuous tuning of a continuous-wave periodically-poled lithium niobate optical parametric oscillator by use of a fan-out grating design,” Opt. Lett. 23, 159-161 (1998).
18. G. D. Boyd, D. A. Kleinman, “Parametric Interaction of Focused Gaussian Light Beams,” J. Appl. Phys. 39, 3597-3639 (1968).
19. S. Chaitanya Kumar, E. Sanchez Bautista, M. Ebrahim-Zadeh, “Stable, high-power, Yb-fiber-based, picosecond ultraviolet generation at 355 nm using BiB_3O_6,” Opt. Lett. 40, 403-406 (2015).
20. K. Fradkin, A. Arie, A. Skliar, G. Rosenman, “Tunable mid-infrared source by difference frequency generation in bulk periodically-poled $KTiOPO_4$,” Appl. Phys. Lett. 75, 914-916 (1999).
21. J. D. Bierlein, H. Vanherzeele, “Potassium titanyl phosphate: properties and new applications,” J. Opt. Soc. B 6, 622-633 (1989).
22. H. Li, F. Zhou, X. Zhang, W. Ji, “Bound electric Kerr effect and self-focusing induced damage in second-harmonic-generation crystals,” Opt. Commun. 144, 75-81 (1997).

23. R. DeSalvo, A. A. Said, D. J. Hagan, E. W. van Sryland, M. Sheik-Bahae, "Infrared to ultraviolet measurements of two-photon absorption and n_2 in wide bandgap solids," IEEE J. Quantum Elect. 32, 1324-1332 (1996).
24. G. K. Samanta, S. Chaitanya Kumar, M. Mathew, C. Canalias, V. Pasiskevicius, F. Laurell, M. Ebrahim-Zadeh, "High-power, continuous-wave, second-harmonic generation at 532 nm in periodically-poled $KTiOPO_4$," Opt. Lett. 33, 2955-2957 (2008).
25. S. Chaitanya Kumar, G. K. Smanta, M. Ebrahim-Zadeh, "High-power, single-frequency, continuous-wave second-harmonic-generation of ytterbium fiber laser in PPKTP and MgO:sPPLT," Opt. Exp. 17, 13711-13726 (2009).
26. K. Kato, E. Takaoka, "Sellmeier and thermo-optics dispersion formulas for KTP", Appl. Opt. 41, 5040-5044 (2002).
27. S. Chaitanya Kumar, A. Esteban-Martin, M. Ebrahim-Zadeh, "Interferometric output coupling of ring optical oscillators," Opt. Lett. 36, 1068-1070 (2011).

Chapter 4

High-repetition-rate mid-infrared picosecond source based on OP-GaP

This chapter constitutes the following publication:

Picosecond difference-frequency-generation in orientation-patterned gallium phosphide

J. Canals Casals [†], **S. Parsa**[†], S. Chaitanya Kumar, K. Devi, P. G. Schunemann, M. Ebrahim-Zadeh

Optics Express **25**(16), 19595-19602 (2017)

†*Equal contribution*

4.1 Motivation

The mid-infrared (mid-IR) region of the electromagnetic spectrum, defined as the wavelengths longer than ~2 μm up to terahertz (THz), has strong absorption fingerprints of numerous molecules, many toxic agents, soil, water and air pollutant, and components of human breath [1]. This makes coherent mid-IR radiations of great interest for a variety of applications such as spectroscopy, breath analysis, photobiology, and novel upconversion imaging techniques [2-5]. Nonlinear frequency conversion processes such as optical parametric oscillators (OPOs) and difference-frequency-generation (DFG)

using appropriate nonlinear materials can generate continuously tunable mid-IR wavelengths, covering the spectral range which are inaccessible by conventional lasers in different time-scale from continuous-wave (cw) to femtosecond in less complex design and with reasonable cost [6-10]. Oxide-based nonlinear optical crystals such as MgO:PPLN, MgO:sPPLT and PPKTP are widely available to generate mid-IR radiation, when they are pumped by commercially available 1-μm laser systems. However, they can cover mid-IR spectral range up to ~4 μm, beyond which they show strong absorption [11,12]. Nonlinear optical semiconductors, such as ZGP and orientation-patterned GaAs (OP-GaAs) offer broader transparency range together with higher nonlinearity, but the unavailability of matured pump laser technology near 2 μm precludes the direct deployment of well-established Nd-based solid-state lasers or Yb-fiber lasers at ~1 μm, since these crystals show strong two-photon absorption below 2 μm [13-16]. Accordingly, nonlinear optical materials with high nonlinearity and broader transparency range into the deep-IR with short-wavelength cutoff extending below 1 μm are widely sought after [17]. $CdSiP_2$ (CSP) is a new birefringent nonlinear crystal which can generate tunable radiations across 6-8 μm when pumped at 1 μm under noncritical phase-matching [6,9,17]. Orientation-patterned GaP (OP-GaP) is a more recently developed quasi-phase-matched (QPM) semiconductor with a broad transparency range from 0.8 μm to ~12 μm, high effective nonlinear coefficient of d_{eff}~45 pm/V, and high thermal conductivity of ~110 $W.m^{-1}.K^{-1}$ [17,18]. The mentioned properties of this new QPM crystal, together with its large bandgap, which enables pumping at 1 μm, make OP-GaP a highly attractive material for the development of nonlinear optical sources from the mid- to deep-IR [17,18].

The first report on parametric oscillation in the OP-GaP was a 2-μm nanosecond OPO in a doubly-resonant (DRO) configuration [19]. The source produced 20 kHz pulses at 3.5 μm (signal) and 5.1 μm (idler) with the maximum total output power of 350 mW for an average input pump power of ~6 W. A nanosecond DRO pumped at 1.064 μm operating at 10 kHz was also reported [20]. The OPO generated temperature-tuned wavelengths from 1.36-1.39 μm in the signal together with tunable radiation across 4.6-4.88 μm in the idler. Pumped at ~1 W, 4 mW of idler at 4.62 μm and 15 mW of signal at 1.32 μm was extracted from the source. Our group also demonstrated tunable DFG in a 40-mm-long

OP-GaP by mixing the input pulses from a nanosecond Nd:YAG laser and the signal beam from a nanosecond MgO:PPLN OPO driven by the same laser at 80 kHz repetition rate [8]. For a signal average power of 1 W and pump power of 5 W, the source generated maximum mid-IR output power of ~14 mW at 2.72 μm. Recently, our group also demonstrated a nanosecond optical parametric generation (OPG) in a 40-mm-long OP-GaP crystal pumped by a 1.064 μm Nd:YAG laser at 25 kHz repetition rate. The source provided tunable radiation across 1.72-1.85 μm in the signal, together with the tunable idlers across 2.5-2.8 μm, with a maximum total average power of ~18 mW [21]. A femtosecond OPO synchronously pumped at 1.04 μm, operating at 100 MHz, was also reported [22]. Using a multi-grating OP-GaP crystal, the source provided spectral coverage in the 5-12 μm wavelength range with average powers in a few to tens of milli watts. In the cw regime, single-pass DFG based on OP-GaP using the pump wavelength of 1.064 μm and signal wavelengths at 1.55 μm was reported, generating up to 152 mW of fixed mid-IR wavelength at 3.4 μm for the pump power of 47 W and signal power of 24 W [23]. Using a 24.6-mm-long OP-GaP, a cw DFG power of 65 μW at a fixed wavelength of 5.85 μm was generated by using a 10 W of pump power at 1.06 μm and ~40 W of signal power at 1.3 μm [24].

Since OP-GaP crystal is in its early stage of development, in order to improve the quality of the material to have more efficient mid-IR parametric sources, study and evaluation of its optical behaviour and performance in different frequency conversion processes across the transparency range of the crystal in different time-scales is critical.

In this chapter, we describe what we believe to be the first tunable high-repetition-rate picosecond mid-IR source based on OP-GaP using a single-pass DFG between a mode-locked Yb-fiber laser at 1.064 μm and the tunable signal output from a picosecond MgO:sPPLT OPO synchronously pumped by the same laser. Using a 40-mm-long OP-GaP crystal with the single grating period of Λ=16 μm, the source provides continuous tunable radiation across 3.04-3.13 μm in the mid-IR at the repetition rate of ~80 MHz. For a maximum pump power of 5 W at 1.064 μm and 0.9 W of signal at 1.64 μm, and at a phase-matching temperature of 153.5ºC in the OP-GaP crystal, we were able to generate

up to 57 mW of DFG average output power at 3.04 μm with a slope efficiency of 1.7%, with passive power stability better than 3.2%rms over 1 hour, in good beam quality.

4.2 Properties of OP-GaP crystal

OP-GaP is a recently introduced QPM nonlinear material and is the first orientation-patterned semiconductor crystal which can generate meaningful amount of mid-IR power in nearly 15 years [25]. It has a high nonlinear coefficient of d_{14}~70.6 pm⁄V and high thermal conductivity of ~110 $W.m^{-1}.K^{-1}$, with a broad transparency range starting in the visible part of the electromagnetic spectrum facilitating the alignment in the optical setup [17,18]. OP-GaP has a large room-temperature indirect bandgap of ~2.6 eV, which shows negligible two-photon absorption at 1 μm [26] and thus can be pumped by the well-stablished Nd-based solid-state laser or Yb-fiber laser technology for efficient frequency conversion into the mid-IR [8,19-24].

GaP has a zinc blende, cubic, non-centrosymmetric crystallographic structure, and therefore it does not exhibit birefringence and cannot typically participate in phase-matched second-order interactions. The phase-matching feature for this crystal is provided by inverting the crystallographic orientation, which corresponds to flipping the crystal orientation [18,23,29,30].

In Fig 4.1 is shown the absorption coefficients of some well-known infrared crystal as a function of wavelength. As is clear, OP-GaP shows very small absorption at 1 μm, α~0.17 cm^{-1}, which enables the deployment of the well-established 1-μm laser pump technology, as mentioned before. Some optical, thermal and mechanical properties of OP-GaP compared with some widely available infrared crystals are listed in Table 4.1, showing the superiority of OP-GaP over well-established mid-IR nonlinear crystals such as MgO:PPLN, ZGP, and CSP.

Figure 4.2(a) shows the wavelength tunability of some OP-GaP-based OPOs pumped at different wavelengths of 1000 nm, 1510 nm, and 2100 nm. Pumping at 1000 nm, the OPO can generate tunable mid-IR idlers across 2300-9000 nm by changing the grating periods of the crystal from Λ=15.5 μm to 31.5 μm, while operating at room temperature. The tuning can also be performed by changing the temperature of the OP-GaP, since its

refractive index shows a small thermal dependence. Thermal sensitivity of the refractive index of OP-GaP is given by the temperature-dependent Sellmeier equation [20],

$$n^2 = A + \frac{(B + CF)(\lambda)^2}{\lambda^2 - (D + EF)^2} + (H + GF)(\lambda)^2 \tag{4.1}$$

where

A	2.78649
B	6.32098
C	1.02×10^{-6} ($^oC^{-1}$)
D	0.29903 (μm)
E	5.92×10^{-8} (μm.$^oC^{-1}$)
H	-0.00307 (μm^{-2})
G	9.18×10^{-9} (μm^{-2}.$^oC^{-1}$)
T_0	22.9 (^oC)
F	$(T-T_0)(T+T_0+546.3)$ (^oC)

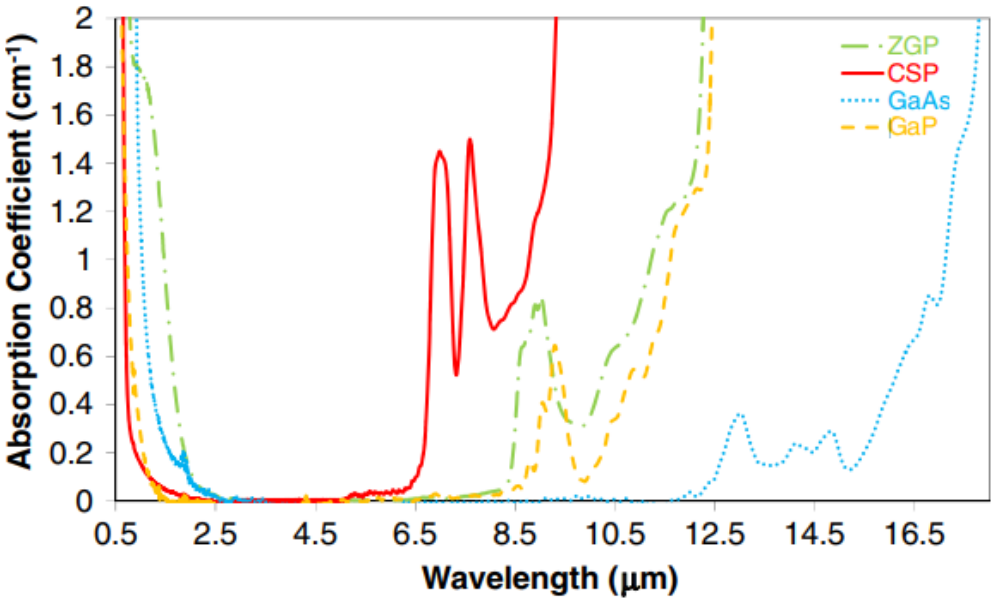

Fig. 4.1. Typical absorption spectra for ZGP, CSP, GaAs, and GaP [17].

Nonlinear optical crystal	MgO:PPLN	MgO:sPPLT	$ZnGeP_2$	OP-GaAs	$CdSiP_2$	OP-GaP
Transparency range (μm)	0.3-5	0.28-5.5	2-12	1.1-17	1-6.5	0.8-12
d_{eff} (pm/V)	17.19	8.8	47.7	75.79	53.82	44.58
Room-temperature bandgap (eV)	3.9	4.9	1.22	1.4	2.08	2.26
Two-photon absorption (cm/Gw)	0.38 @0.532 μm	0.55 @0.532 μm	2.72 @1 μm	10 @1.5 μm	2.6 @1 μm	0.2 @1 μm
Thermal conductivity (W/m.K)	5	8.78	36	52	13.6	110
Knoop hardness (kg/mm^2)	630	766	980	750	930	850

Table 4.1. Properties of some well-known mid-IR QPM and BPM nonlinear crystals [17,18,23,29-40].

Figure 4.2(b) shows the theoretical temperature tuning curves for a 1064-nm-pumped OP-GaP OPO with the grating periods of Λ=15 μm, 20 μm, and 30 μm, calculated using the mentioned temperature-dependent Sellmeier equation [20]. Changing the temperature of the nonlinear crystal from 30°C to 200°C, and using a grating period of Λ=30 μm, the source can cover the mid-IR wavelengths from 8229 nm to 8368 nm.

As mentioned earlier, OP-GaP is a new nonlinear crystal and its growth technology is not yet mature. Therefore, it is important to study the properties of the crystal for different nonlinear optical processes, as well as to investigate its performance across the transparency range in different time-scales. The motivation of conducting this study was to investigate the behaviour of the OP-GaP when it is pumped by high-repetition-rate picosecond near-IR radiations in order to pave the way of improving the quality of the crystal to a suitable level for further development of efficient parametric sources into the deep-IR.

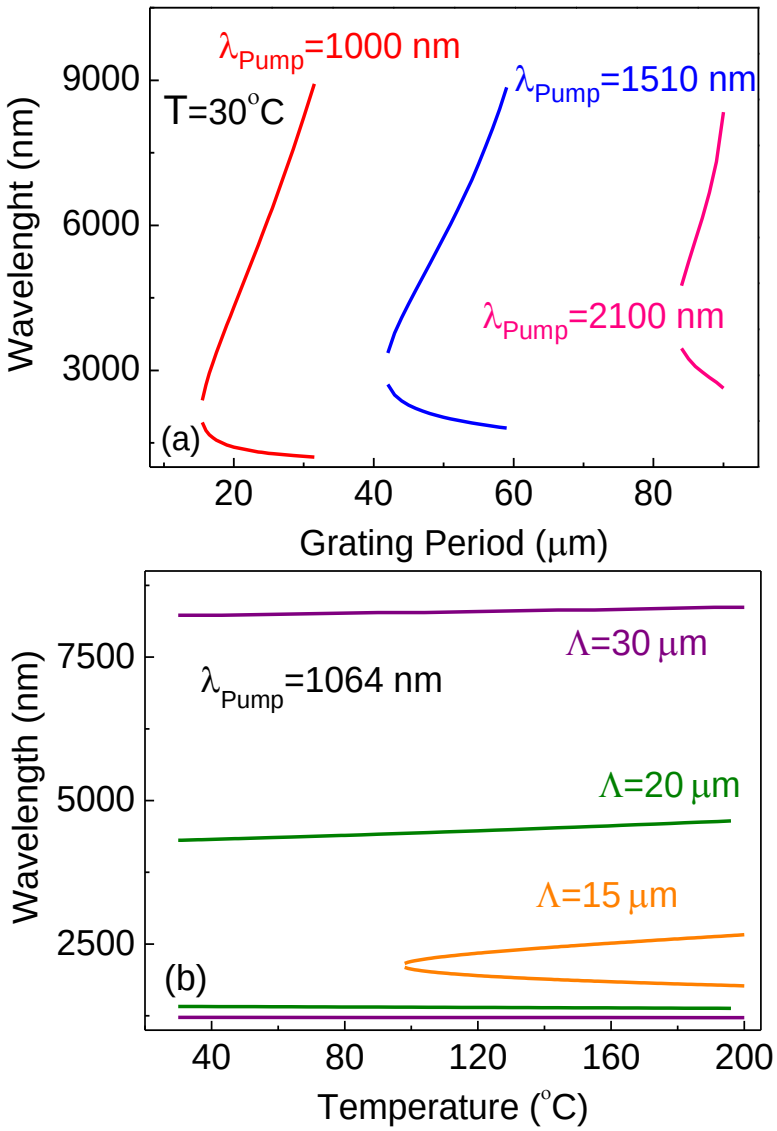

Fig. 4.2. (a) Grating tuning for an OP-GaP OPO pumped at different wavelengths, at room temperature. (b) Temperature tuning for a 1064-nm-pumped OPO based on OP-GaP with different grating periods.

4.3 Experimental setup

The schematic of the experimental setup, together with the picture of the OP-GaP crystal used in this experiment, is shown in Fig. 4.3. The primary pump source is a mode-locked Yb-fiber laser (Fianium, FP1060-20) delivering up to 20 W of average power of ~20 ps pulses at ~80 MHz repetition rate. The laser source operates at a central wavelength of 1064 nm with a full-width at half-maximum (FWHM) spectral bandwidth of 0.8 nm. A

major portion of the output power from the laser is used to synchronously pump a picosecond OPO based on a 30-mm-long MgO:sPPLT nonlinear crystal with six gratings, ranging in period from Λ=29.5 μm to 30.65 μm [10]. However, in the present experiment, we used a single grating period of Λ=30.65 μm. The OPO can provide ~17 ps temperature-tuned signal wavelengths across 1609-1637 nm. The extracted signal power scaling measurements for the OPO at 1636 nm as a function of incoming pump power is shown in Fig. 4.4. Using an output coupler (OC) of ~22% at maximum pump power of 10 W, the OPO generated as much as 1.57 W of signal wavelengths at 1636 nm with maximum pump depletion of 68% and an estimated slope efficiency of 16%. In the inset of Fig. 4.4 is presented the theoretical temperature tuning curves for the grating period of Λ=30.65 um, calculated using the Sellmeier equation from Ref. [38].

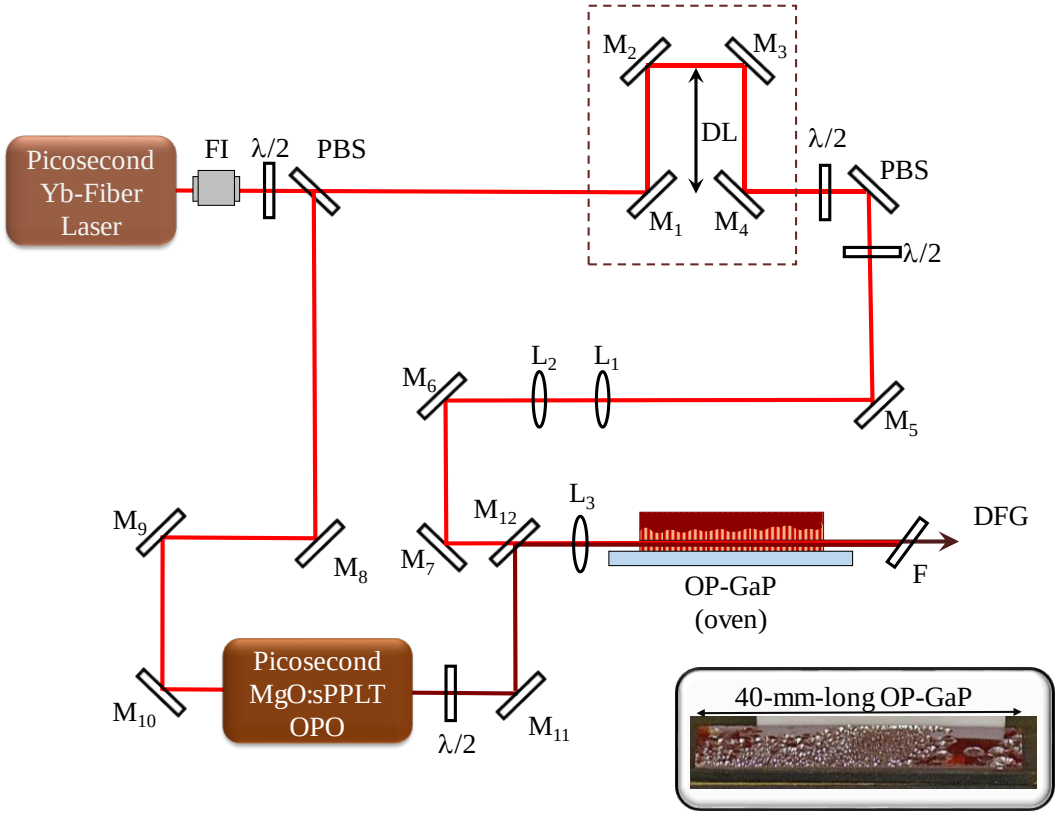

Fig. 4.3. Schematic of the experimental setup for the high-repetition-rate picosecond DFG in OP-GaP. FI, Faraday isolator; DL, variable delay line; λ/2, half-wave plate; PBS, polarizing beam-splitter; L, lens; M, mirror; F, filter. Inset: 40-mm-long OP-GaP crystal used in this experiment.

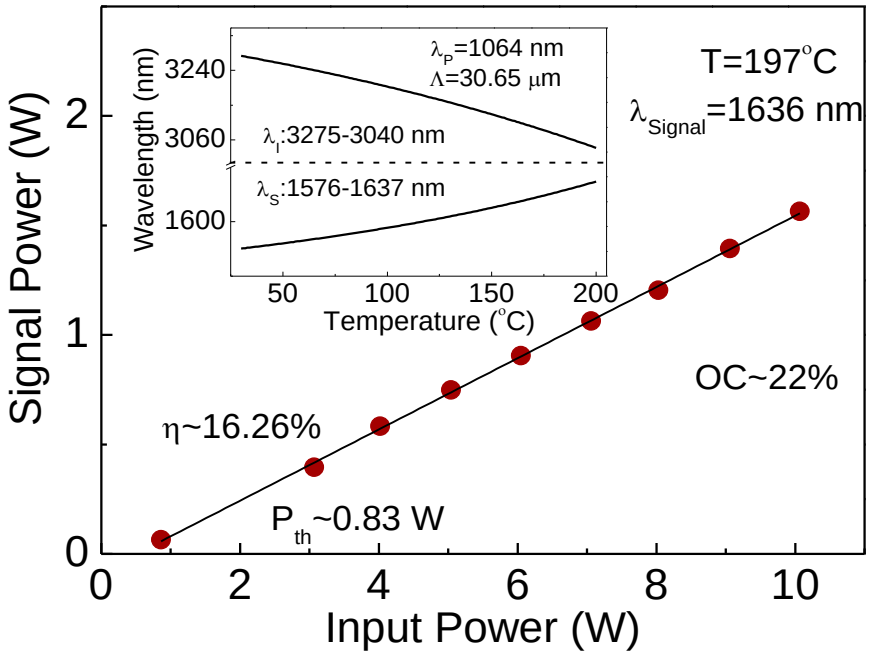

Fig. 4.4. Extracted signal power at 1636 nm as a function of pump power. Inset: Theoretical temperature tuning curves for a 1064-nm-pumped MgO:sPPLT OPO with Λ=30.65 μm. λ_P, λ_S, and λ_I represent pump, signal, and the idler wavelengths, respectively.

The remaining power from the primary Yb-fiber laser is used as a pump source for DFG in the OP-GaP crystal. A variable delay line (DL) comprising mirrors, M_1-M_4, in the pump beam line provides the required path-length for synchronization between the two input pulses in the OP-GaP crystal. The combination of a half-wave plate (λ/2) and polarizing beam-splitter (PBS) is used to adjust the pump power, and a second half-wave plate is used to control the pump polarization for phase-matching in the crystal. The pump and signal polarizations are independently optimized to achieve the maximum DFG output power. The converging lenses, L_1 and L_2, with focal lengths of f=125 mm and 50 mm, respectively, were used to adjust the diameter of the pump beam. The dichroic mirror, M_{12}, which is antireflection (AR)-coated for high reflection (R>99%) over 1300-2000 nm and high transmission (T>90%) at 1064 nm, is used to combine the pump and signal beams. Using a single converging lens, L_3, with f=75 mm, the input beams are focused to a beam waist radius of w_{oP}~20 μm for the pump and w_{oS}~35 μm for the signal inside the crystal, corresponding to the pump focusing parameter of ξ_P~5.4 and the signal focusing parameter of ξ_S~2.77 [40], resulting in an estimated DFG beam waist radius of

w_{oDFG}~17.4 μm. Because of a small difference in the refractive indices of the pump and the signal wavelengths, the focused pump and signal beams are separated slightly inside the crystal, so the position of the crystal has been optimized to achieve the maximum DFG power and for this the crystal was mounted on a three-axis stage.

The OP-GaP crystal used for DFG in this study was produced at BAE system using a combination of molecular beam epitaxy (MBE) and hydride vapor phase epitaxy (HVPE) [29]. The crystal has 40 mm length with a single grating period of Λ=16 μm and the aperture size of 1.7×6 mm^2. However according to our experimental results which will be explained later in this chapter, we estimated the useful aperture of the crystal over which the QPM grating is available to be limited to <500 μm. The crystal is housed in an oven whose temperature can be controlled from room temperature to 200°C with the temperature stability of ±0.1°C. The end-faces of the crystal are AR-coated (R<5%) at 1064 nm and 1500-1900 nm, with high transmission (R<25%) over 3000-3100 nm. The generated mid-IR output DFG is filtered using a Ge long-pass filter (F) with cut-on wavelength of 2.4 μm.

4.4. Results and discussion

When the pump beam was incident on the crystal, the green second-harmonic of the pump could be observed. With both signal and pump together and properly aligned inside the crystal, we also observed non-phase-matched sum-frequency-generation (SFG) between the pump and signal in the red part of the visible spectrum, as shown in Fig. 4.5. We used this SFG signal to optimize the spatial overlap of the input beams as well as finding the most suitable position in the OP-GaP sample, by scanning the position of the crystal in the horizontal and vertical directions. We noticed that although the OP-GaP sample has a large aperture of 1.7×6 mm^2, only a few positions in the crystal resulted in improved SFG output. At this point, with further increase in the input power, we observed DFG together with another visible SFG between the pump and the generated DFG. The DFG signal was very sensitive to the position of the crystal. A small change in the crystal position resulted in a drastic drop in the DFG power, indicating significant grating non-uniformity as well as a notably smaller useful aperture than the nominal aperture over the 40-mm length of the OP-GaP crystal.

4.4.1 Phase-matching properties

Having finally established the conditions for the attainment of maximum DFG power, we proceeded to characterize the picosecond high-repetition-rate DFG source. First, we investigated the wavelength tuning performance by simultaneous variation of the OPO signal wavelengths from 1637 to 1609 nm, by changing both the temperature of the MgO:sPPLT crystal from 200ºC to 148ºC and the phase-matching temperature of the OP-GaP crystal. The DFG temperature tuning results, presented in Fig. 4.6, demonstrate that the source can be tuned over 92 nm across 3040-3132 nm in the mid-IR. The experimental data are shown in solid circles and the theoretical calculations, from the Sellmeier equation of [20], are plotted in dashed curves. The DFG wavelength varies at a rate of 2.46 nm/°C and the small discrepancy between the theoretical calculations and the experimental data is attributed to the difference in the actual temperature of the OP-GaP and the oven temperature. The pump and signal wavelengths from the MgO:sPPLT OPO were measured using an infrared spectrum analyser, while the DFG wavelength was calculated from energy conservation and further was confirmed by the parasitic SFG between the pump and the DFG output, which were measured by using a visible spectrometer (Ocean Optics, HR4000, resolution of 0.5 nm).

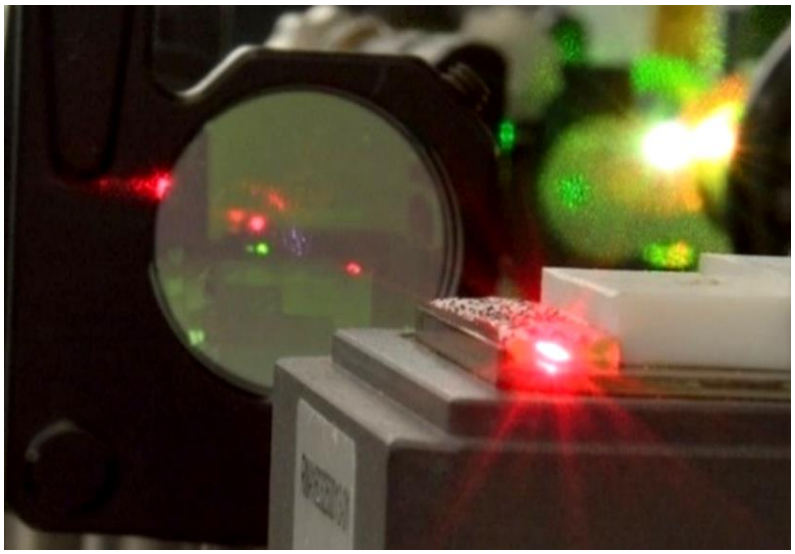

Fig. 4.5. Intense red SFG between the pump and the signal beam.

Courtesy of Junxiong Wei

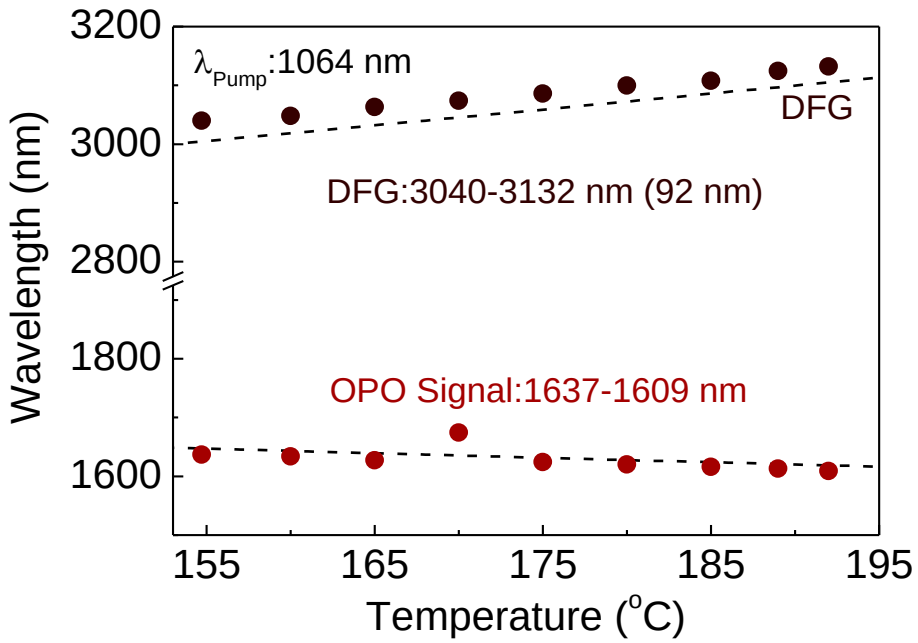

Fig. 4.6. Temperature tuning performance of the picosecond DFG source based on OP-GaP.

In order to study the phase-matching properties of the OP-GaP crystal and to investigate the tolerance of the generated DFG power to temperature, we evaluated the temperature acceptance bandwidth of the 40-mm-long OP-GaP crystal at the signal wavelength of 1636 nm. To avoid any unwanted contribution from thermal effects, the measurements were performed at signal and pump power of 0.8 W and 2 W, respectively. The normalized DFG power as a function of the temperature deviation about the measured phase-matching temperature of 167.5ºC, is shown in Fig. 4.7(a) in solid circles. The $sinc^2$ function, in solid line, shows a FWHM bandwidth of ΔT=6.8ºC, which is much larger than the theoretically estimated of ΔT=0.9ºC for a 40-mm-long OP-GaP crystal, as shown in Fig 4.7(b). The discrepancy between the calculated and the measured temperature acceptance bandwidth values can be ascribed to the presence of non-uniformity and imperfections in the gratings as well as the duty-cycle errors over the 40-mm length of the crystal, which result in a shorter useful interaction length than the physical length of the OP-GaP sample. Using the experimentally measured temperature acceptance bandwidth, we calculated an effective interaction length to be ~5.5 mm, about seven times shorter than the physical length of the crystal, as shown in the inset of Fig.

4.7(a). Another factor can be attributed to the confinement and non-uniformities in the useful aperture of the crystal along its 40-mm length, which results in non-optimum overlap of the pump and signal beams along the propagation direction over the full crystal length, resulting in lower nonlinear conversion efficiency and reduced effective interaction length.

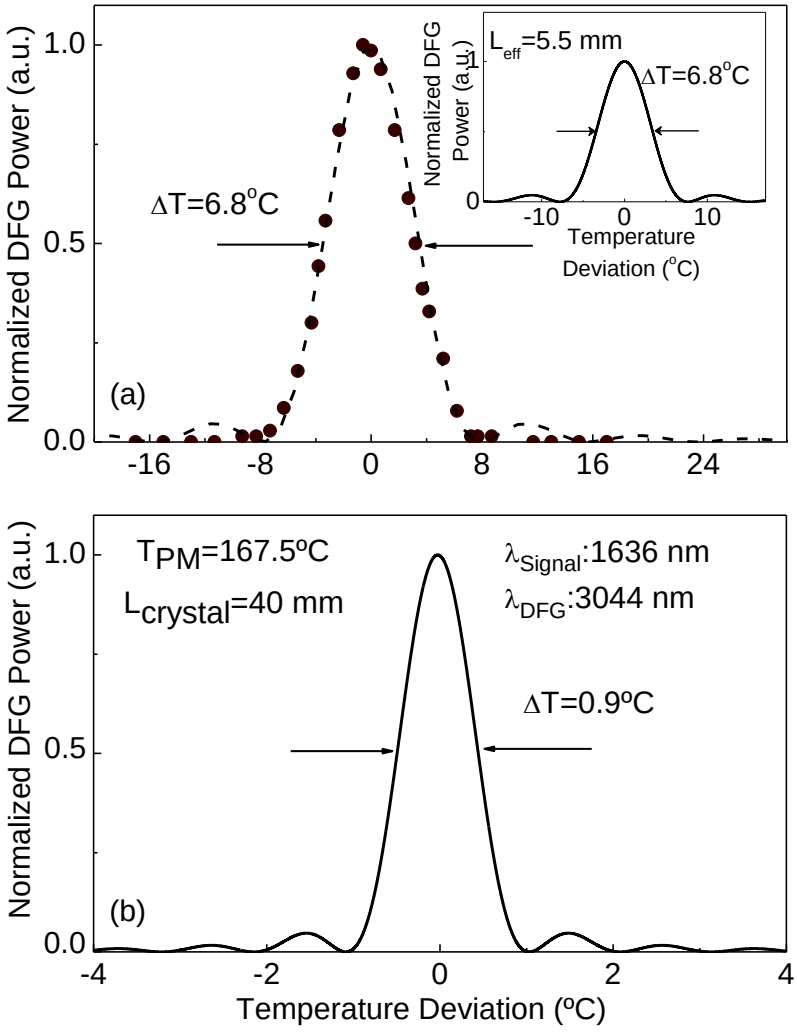

Fig. 4.7. (a) Experimentally measured temperature acceptance bandwidth for the 40-mm-long OP-GaP crystal. Inset: Theoretically calculated temperature acceptance bandwidth for L_{eff}=5.5 mm. (b) Theoretically calculated temperature acceptance bandwidth for a 40-mm-long OP-GaP. T_{PM} represents the phase-matching temperature.

We further studied the output power performance of the DFG source for a maximum pump power of 5 W at 1064 nm and a signal power of 0.9 W across the tuning range of the picosecond DFG sources, as shown in Fig. 4.8. The DFG average power varies from 57 mW at 3044 nm to 8.6 mW at 3132 nm, providing >30 mW over >50% of the entire tuning range. It is worth mentioning that the DFG powers presented here are not corrected for the AR-coating loss (~25%) of the OP-GaP crystal facets. Also shown in inset (a) of Fig. 4.8 is the pump spectrum centered at 1064 nm with a FWHM bandwidth of ~0.8 nm. The measured OPO signal spectrum at 1636 nm, exhibiting a FWHM spectral bandwidth of ~0.8 nm, is presented in inset (b) of Fig. 4.8. These spectral measurements were performed at a maximum DFG power of 57 mW using a spectrum analyser with ~0.1 nm resolution.

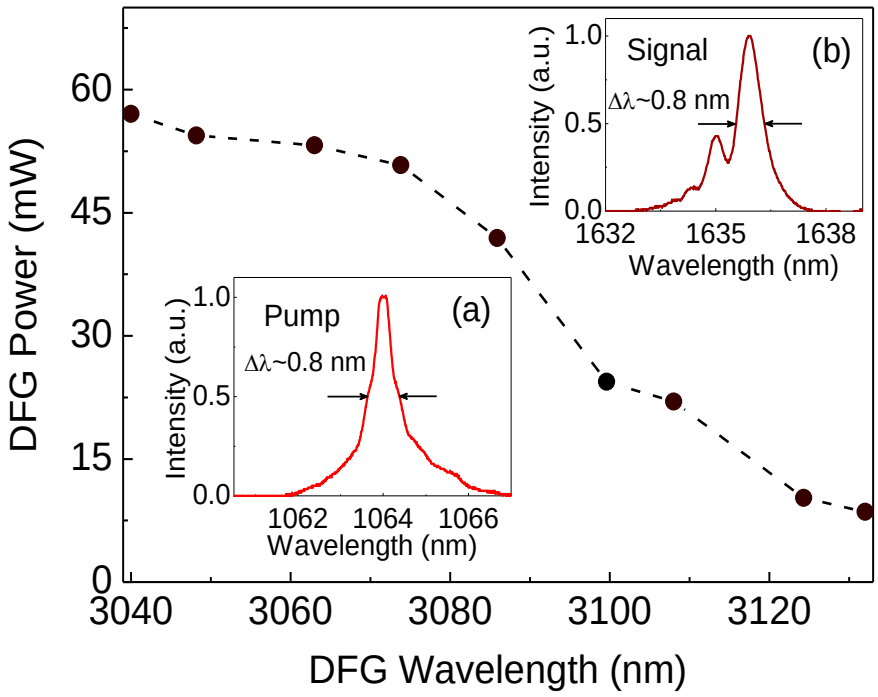

Fig. 4.8. DFG output power across the tuning range. Inset: (a) pump, and (b) signal spectra centred at 1064 nm and 1636 nm, respectively.

4.4.2 Power scaling

Further, we characterized the DFG source by performing the power scaling measurement of the extracted mid-IR power as a function of the input pump power for a fixed signal power of 0.9 W, with the results shown in Fig 4.9. For a maximum pump power of 5 W at 1064 nm and 0.9 W of signal at 1636 nm at the phase-matching temperature of 153.5ºC in the OP-GaP crystal, we were able to extract as much as 57 mW of DFG average power at 3044 nm with a slope efficiency of 1.7%. The presented data show linear trend up to 5 W of pump power, which corresponds to maximum pump to DFG conversion efficiency of ~1%.

While performing the power scaling, we observed a drop in the extracted DFG power by increasing the input pump power. This can be explained as non-negligible absorption of the crystal at the two incoming beams, resulting in heating up the OP-GaP, and thus influencing the quasi-phase-matching condition. Hence, at each input pump power level, we optimized the phase-matching temperature of the crystal to achieve the maximum DFG power. As can be seen from Fig. 4.9, increasing the pump power from 2 W to 5 W was accompanied by decreasing the temperature of the crystal from 167.5ºC to 153.5ºC, in order to achieve the maximum DFG power. This significant temperature rise of ~14ºC, which is more than two times wider than the measured temperature acceptance bandwidth in Fig 4.7(a), confirms strong absorption of the OP-GaP crystal at the interacting beams.

In a separate experiment, we measured the transmission of OP-GaP crystal for the pump at a temperature of 154.5°C, at the same position where we extracted maximum DFG power. The results showed a low transmission of ~52% for the pump. In spite of high transmission for the 1-µm pump reported in the literature [17], we were not able to measure such high transmission through our long OP-GaP crystal. We noticed that the transmission was also inhomogeneous across the aperture of the crystal, which can be attributed to the free-carrier absorption due to the penetrated divergent beam in the lower part of the OP-GaP sample.

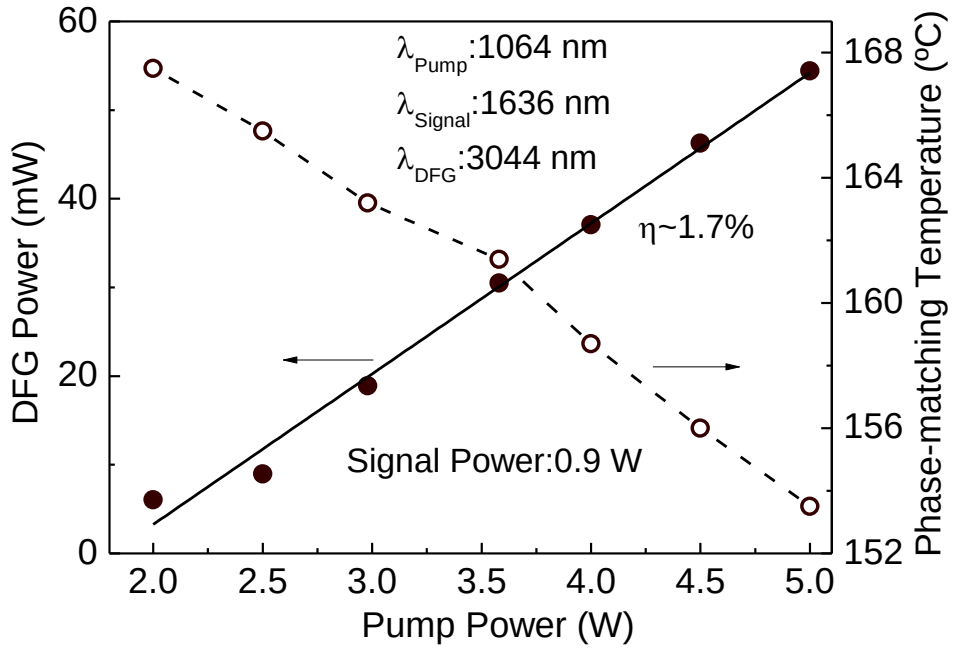

Fig. 4.9. DFG power scaling and OP-GaP phase-matching temperature as a function of the pump power at a fixed signal power.

Further, we estimated the effective nonlinear coefficient, d_{eff}, from the power scaling data for the DFG process in the OP-GaP crystal. In the case of perfect phase-matching, and in the limit of low conversion efficiency, the pump to extracted DFG conversion efficiency, η, can be evaluated as [43]:

$$\eta = \frac{P_{DFG}}{P_P} = \frac{8(\pi d_{eff} L_{crystal})^2 I_S}{\lambda_{DFG}^2 c \varepsilon_o n_P n_S n_{DFG}} \tag{4.2}$$

For all the involved parameters, the subscripts P, S, and DFG, indicate to which beam (pump, signal, or DFG) the parameter is referred to; therefore, P is the average power, I is the intensity, λ is the wavelength, and n is the refractive index. Also, d_{eff}, $L_{crystal}$, c, and ε_o refer to the effective nonlinearity of the medium, the length of the crystal, the speed of light and the vacuum permittivity, respectively. We have calculated the effective nonlinearity of the OP-GaP crystal to be d_{eff}~23 pm/V, corresponding to d_{14}~36.11 pm/V for the 3044 nm mid-IR wavelength. The deviation of the calculated d_{eff} from what is expected from a OP-GaP crystal [28] can be due to the non-uniform propagation

of the gratings and the duty-cycle errors of the QPM grating periods along the crystal resulting in reduced effective length and small output power, non-uniform useful aperture of the crystal which clips the divergent generated beam, as well as the small FWHM spectral acceptance of the 40-mm-long crystal, ~0.094 nm for 1064 nm, compared to the incoming pump linewidths of ~0.8 nm, as shown in Fig 4.10.

According to our observation and the experimental results, we believe that absorption and scattering of the interacting beams inside the crystal, clipping the generated mid-IR beam with the large divergence angle of ~18.34 mrad by the non-uniform and small exit facet of the crystal, non-uniform distribution of the grating periods, and un-optimized focusing of the incoming beams, contribute to the low output DFG power and the small extracted efficiency.

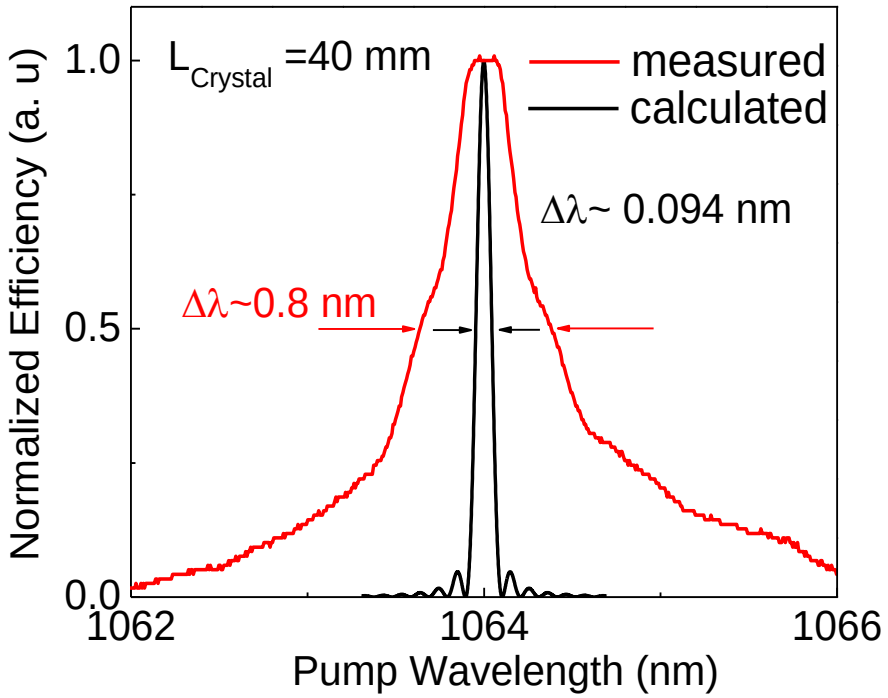

Fig. 4.10. The measured input pump linewidth at 1064 nm together with the calculated pump acceptance bandwidth for the 40-mm-long OP-GaP.

4.4.3 Synchronization and temporal studies

In order to achieve the maximum extraction efficiency from a high-repetition-rate picosecond DFG source, the optimum spatial and temporal overlap between the input beams should be provided. In our experiment, the spatial overlap was obtained by optimizing the combining mirror, M_{12}, Fig. 4.3, and the temporal overlap is attained by varying the pump beam path-length with a delay line (DL), also shown in Fig. 4.3.

While the temporal overlap between the pulses can be achieved by using the delay line, inside the crystal, the interacting beams are affected by dispersion, and are separated in time while propagating inside the medium. Group velocity mismatch (GVM) is a quantity describing the phase-matching bandwidth between the interacting beams, as well as defining the effective temporal walk-off length. In Fig. 4.11(a) is shown the GVM between pump and signal pulses as a function of signal wavelengths, varying from 592 fs/mm to 597.2 fs/mm in the signal wavelengths of interest. At the signal wavelength of 1636 nm, the GVM between the pump and signal is calculated to be ~597 fs/mm, which corresponds to an effective temporal interaction length of ~28.5 mm, and results in a temporal walk-off ~24 ps between the pump and the signal pulses in the 40-mm-long OP-GaP crystal.

Further, we investigated the effect of temporal synchronization on the DFG output power by measuring the extracted DFG power as a function of time delay between the two input interacting beams. As shown in Fig. 4.11(b), the DFG power drops gradually on either side of the zero delay and the maximum DFG power is achieved when both the incoming pulse trains are synchronized. The measured time delay has a FWHM of $\Delta\tau$~10 ps, consistent with the pump and signal pulse durations of ~20 ps and ~17 ps, respectively.

Presented in Fig. 4.12 are the pulse trains of the pump and the signal beams measured by using a fast InGaAs photodetector (5 GHz, t_R <70 ps) and a fast oscilloscope (300 MHz, 2.5 GB/s). The measurements show ~12.5 ns between two pulses in both cases, corresponding to a repetition rate of ~80 MHz. Since the path-length of the pump has been optimized to provide perfect synchronization with the signal, one can be sure that the repetition rate of the generated DFG is also ~80 MHz.

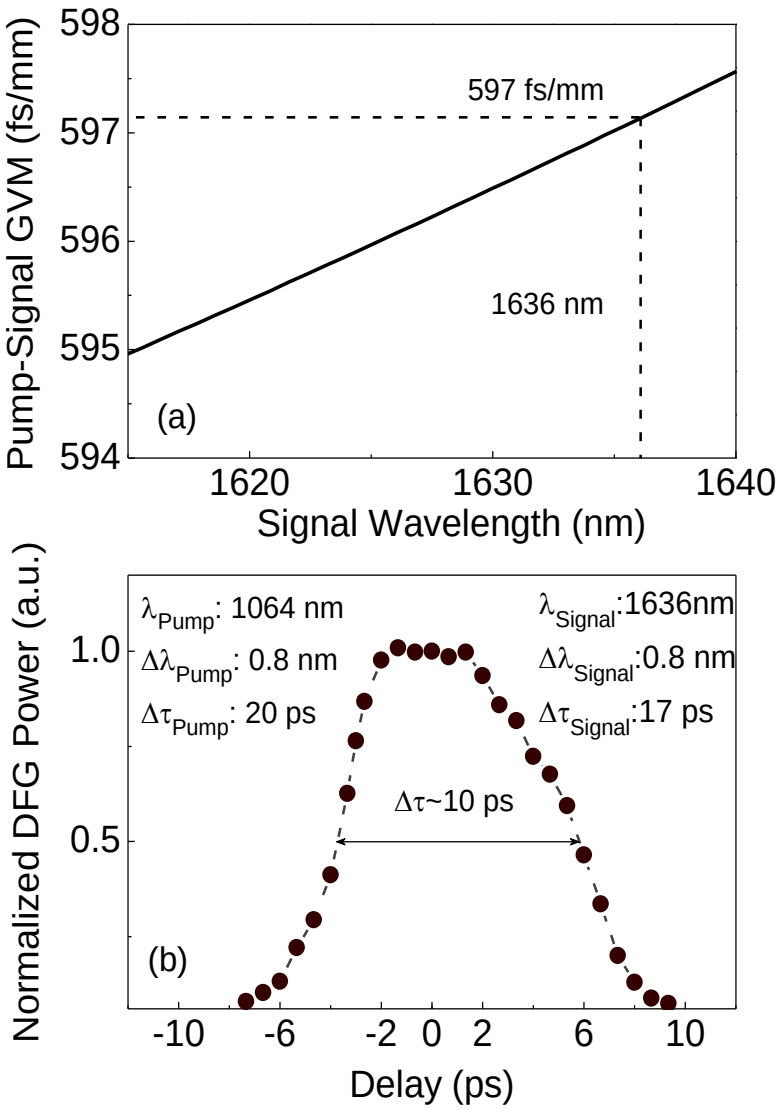

Fig. 4.11. (a) GVM between the pump and signal pulses in the OP-GaP crystal. (b) Normalized DFG power as a function of the pump delay.

4.4.4 Power stability and beam profile

Characterization of the DFG source proceeded with performing the long-term power stability measurement of the pump, signal, and the extracted DFG, with the results shown in Fig. 4.13(a-c). The measurements were performed at the DFG wavelength of 3044 nm, for the pump power of 5.2 W and the signal power of ~0.7 W at 1636 nm. As clear from Fig. 13(a,b), the pump and signal beams exhibit passive power stability better than 0.2%rms and 2.4%rms, respectively, over 1 hour, while the DFG output has power

stability better than 3.2%rms over the same period of time at a DFG average power of 53 mW, as shown in Fig. 13(c).

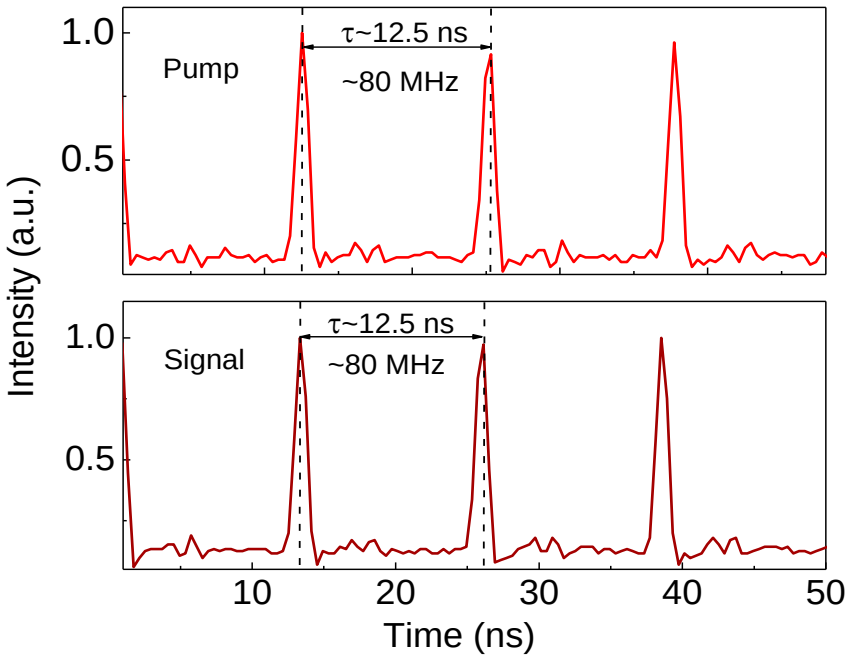

Fig. 4.12. Pump and signal pulse trains, showing pulses with repetition rate of ~80 MHz.

The far-field energy distributions of the interacting beams at 1064 nm and 1636 nm, and the generated mid-IR DFG at 3044 nm, were recorded by using a pyroelectric camera (Spiricon, Pyrocam-III). The results, presented in Fig. 4.14(a-c), confirm TEM_{00} spatial profile with single-peak Gaussian distribution for all the interacting beams. Although the pump and signal beams exhibit circularity of >95%, the ellipticity of ~73% in the DFG was observed, which indicates the spatial confinement of generation to the lower part of beam due to the tapering of the QPM grating, resulting in non-ideal grating period and duty-cycle errors over the 40-mm length of the OP-GaP crystal.

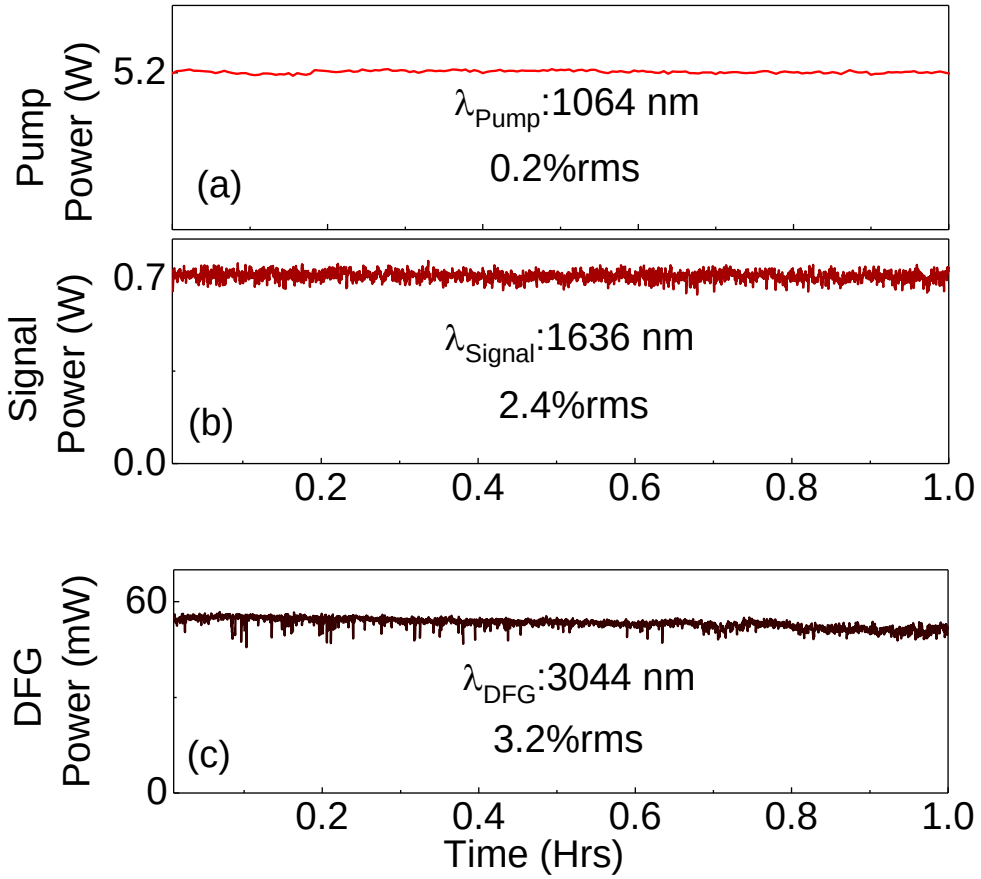

Fig. 4.13. Long-term power stability of the (a) pump at 1064 nm, (b) signal at 1636 nm, and (c) DFG at 3044 nm over 1 hour.

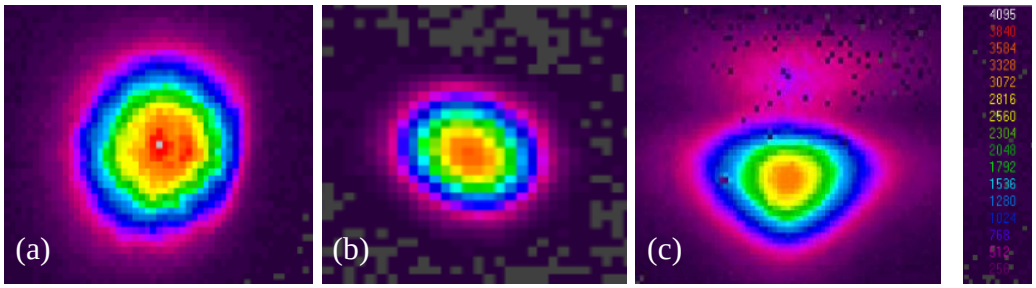

Fig. 4.14. Spatial beam profiles of the (a) pump at 1064 nm, (b) signal at 1636 nm, and (c) the generated mid-IR beam at 3044 nm.

4.5 Conclusion

In this chapter, we have demonstrated the first high-repetition-rate picosecond mid-IR source by using a 40-mm-long OP-GaP crystal with a single grating period of Λ=16 μm,

tunable across 3040-3132 nm. The source was realized as a single-pass DFG of a mode-locked Yb-fiber laser at 1064 nm and a temperature-tuned signal output from a picosecond MgO:sPPLT OPO synchronously pumped by the same laser. The approach has provided >30 mW mid-IR radiations over >50% of the tuning range for an input pump power of 5 W and signal power of ~0.9 W, with a maximum DFG power of 57 mW at 3044 nm in TEM_{00} spatial beam quality with a circularity of ~73%. The power scaling measurements of the extracted DFG at 3044 nm as a function of pump power at signal wavelength of 1636 nm at 0.9 W resulted in a linear trend up to 5 W of pump with a slope efficiency of ~1.7% and maximum mid-IR power of ~57 mW.

The source exhibits a passive power stability better than 3.2%rms at the maximum power of 57 mW at 3044 nm over 1 hour compared to ~0.2%rms and ~2.4%rms for the pump and the signal beam at 1636 nm, respectively, over the same period of measurement.

We have studied the effect of temporal overlap between the input pump and signal beams in the 40-mm-long OP-GaP by varying the delay line in the pump-path and recording the corresponding extracted DFG power. The results show a temporal walk-off of ~24 ps between the interacting pump and signal wavelengths, corresponding to an effective interaction length of ~29 mm. We have also measured the pulse trains of the pump and the signal to be ~80 MHz, which confirm a repetition rate of the generated DFG to be also ~80 MHz.

Our investigations on the phase-matching properties of the OP-GaP have shown a large difference between the measured temperature acceptance bandwidth and the theoretical estimated value, giving a short effective interaction length of ~5.5 mm, which results in low conversion efficiency and small extracted output power. We have also calculated d_{eff} of the crystal in this experiment to be ~23 pm/V, much smaller than what is expected from a bulk GaP crystal.

We attribute the limiting factors in having high-repetition-rate picosecond mid-IR source based on OP-GaP crystal with high efficiency in this experiment to the non-uniform propagation and duty-cycle errors of the QPM grating, small and varied useful aperture along the whole crystal length as well as the small spectral acceptance bandwidth of the 40-mm-long OP-GaP crystal compared to the incoming pump linewidth. By improving

the crystal growth process and enhancing the overall optical quality, as well as the grating period uniformity and useful aperture, one can expect more efficient sources based on nonlinear frequency conversion in OP-GaP, which can be used in many applications demanding high-repetition-rate picosecond tunable coherent beams with the wavelengths beyond ~3 μm into the deep-IR.

References

1. M. Ebrahim-Zadeh, I. T. Sorokina, "Mid-infrared Coherent Sources and Applications," (Springer, 2008).
2. M. R McCurdy, Y. Bakhirkin, G. Wysocki, R. Lewicki1 F. K Tittel, "Recent advances of laser-spectroscopy based techniques for applications in breath analysis," J. Breath Res. 1, 04001-040013 (2007).
3. C. Schumann, R. Groß, M. M. N. Wolf, R. Diller, N. Michael, T. Lampartery, "Subpicosecond Midinfrared Spectroscopy of the P_{fr} Reaction of Phytochrome Agp1 from Agrobacterium tumefaciens," Biophys. J. 94, 3189-3197 (2008).
4. A. Tokmakoff, B. Sauter, M. D. Fayer, "Temperature-dependent vibrational relaxation in polyatomic liquids: Picosecond infrared pump-probe experiments," J. Chem. Phys. 100, 9035-9043 (1994).
5. M. Mathez, P. John Rodrigo, P. Tidemand-Lichtenberg, C. Pedersen, "Upconversion imaging using short-wave infrared picosecond pulses," Opt. Lett. 42, 579-582 (2017).
6. S. Chaitanya Kumar, A. Esteban-Martin, A. Santana, K. T. Zawilski, P. G. Schunemann, M. Ebrahim-Zadeh, "Pump-tuned deep-infrared femtosecond optical parametric oscillator across 6-7μm based on $CdSiP_2$," Opt. Lett. 41, 3355-3358 (2016).
7. K. Devi, P. G. Schunemann, M. Ebrahim-Zadeh, "Continuous-wave, multimilliwatt, mid-infrared source tunable across 6.4-7.5 μm based on orientation-patterned GaAs," Opt. Lett. 39, 6751-6754 (2014).
8. J. Wei, S. Chaitanya Kumar, H. Ye, K. Devi, P. G. Schunemann, M. Ebrahim-Zadeh, "Nanosecond difference-frequency-generation in orientation-patterned gallium phosphide," Opt. Lett. 42, 2193-2196 (2017).
9. S. Chaitanya Kumar, M. Jelínek, M. Baudisch, K. T. Zawilski, P. G. Schunemann, V. Kubeček, J. Biegert, M. Ebrahim-Zadeh, "Tunable, high-energy, mid-infrared, picosecond optical parametric generator based on cadmium silicon phosphide," Opt. Exp. 20, 15703-15709 (2012).

10. S. Chaitanya Kumar, M. Ebrahim-Zadeh, "High-power, continuous-wave, mid-infrared optical parametric oscillator based on MgO:sPPLT," Opt. Lett. 36, 2578-2580 (2011).
11. A. Zukauskas, N. Thilmann, V. Pasiskevicius, F. Laurell, C. Canalias, "5 mm thick periodically poled Rb-doped KTP for high-energy optical parametric frequency conversion," Opt. Mater. Exp. 1, 201-207 (2011).
12. O. Kokabee, A. Esteban-Martin, M. Ebrahim-Zadeh, "Efficient, high-power, ytterbium-fiber-laser-pumped picosecond optical parametric oscillator," Opt. Lett. 35, 3210-3212 (2010).
13. L. Wang, T. Xing, S. Hu, X. Wu, H. Wu, J. Wang, H. Jing, "Mid-infrared ZGP-OPO with a high optical-to-optical conversion efficiency of 75.7%," Opt. Exp. 25, 3373-3380 (2017).
14. A. F. Nieuwenhuis, C. J. Lee, P. J. M. van der Slot, I. D. Lindsay, P. Gross, K. J. Boller, "High-efficiency mid-infrared $ZnGeP_2$ optical parametric oscillator directly pumped by a lamp-pumped, Q-switched CrTmHo:YAG laser," Opt. Lett. 33, 52-54 (2008).
15. A. Hildenbrand, C. Kielecka, E. Lallierb , D. Fayeb, A. Grisardb, B. Gérardc , M. Eichhorna, "Compact efficient mid-infrared laser source: OP-GaAs OPO pumped by Ho^{3+}:YAG laser," Proc of SPIE. 8187, 81870H-1 (2011).
16. K. L. Vodopyanov, I. Makasyuk, P. G. Schunemann, "Grating tunable 4-14 μm GaAs optical parametric oscillator pumped at 3 μm," Opt. Exp. 22, 4131-4136 (2014).
17. P. G. Schunemann, K. T. Zawilski, L. A. Pomeranz, D. J. Creeden, P. A. Budni, "Advances in nonlinear optical crystals for mid-infrared coherent sources," J. Opt. Soc. Am. B 33, D36-D43, (2016).
18. V. Tassev, M. Snure, R. Peterson, K. L. Schepler, R. Bedford , M. Mann, S. Vangala, W. Goodhue, A. Lin, J. Harrisd, M. Fejerd, Peter Schunemann, "Progress in orientation-patterned GaP for next-generation nonlinear optical devices," Proc of SPIE. 8604, 86040V-1 (2013).
19. P. G. Schunemann, L. A. Pomeranz, D. J. Magarrell, "First OPO based on orientation-patterned gallium phosphide (OP-GaP)," Conference on Lasers and Electro-Optics (CLEO) (Optical Society of America, 2015), paper SW3O.1.

20. P. G. Schunemann, L. A. Pomeranz, D. J. Magarrell, J. C. McCarthy, K. T. Zawilski, D. E. Zelmon, "1064-nm-pumped mid-infrared optical parametric oscillator based on orientation-patterned gallium phosphide (OPGaP)," Conference on Lasers and Electro-Optics (CLEO) (Optical Society of America, 2015), paper SW3O.4.
21. H. Ye, S. Chaitanya Kumar, J. Wei, P. G. Schunemann, M. Ebrahim-Zadeh, "Optical parametric generation in orientation-patterned gallium phosphide," Opt. Lett. 42, 3694-3697 (2017).
22. L. Maidment, P. G. Schunemann, D. T. Reid, "Molecular fingerprint-region spectroscopy from 5 to 12 μm using an orientation-patterned gallium phosphide optical parametric oscillator," Opt. Lett. 41, 4261-4264 (2016).
23. S. Guha, J. O. Barnes, P. G. Schunemann, "Mid-wave infrared generation by difference frequency mixing of continuous wave lasers in orientation-patterned Gallium Phosphide," Opt. Mater. Exp. 5, 2911-2923 (2015).
24. G. Insero, C. Clivati, D. D'Ambrosio, P. Natale, G. Santambrogio, P. G. Schunemann, J. J. Zondy, S. Borri, "Difference frequency generation in the mid-infrared with orientation-patterned gallium phosphide crystals," Opt. Lett. 41, 5114-5117 (2016).
25. I. Shoji, T. Kondo, A. Kitamoto, M.i Shirane, R. Ito, "Absolute scale of second-order nonlinear-optical coefficients," J. Opt. Soc. Am. B 14, 2268-2294 (1997).
26. D.A.Yas'kov, A.N.Pikhtin, "Optical properties of gallium phosphide grown by floating zone II. Absorption and luminescence," Mater. Res. Bull. 4, 839-848 (1969).
27. P. S. Kuo, K. L. Vodopyanov, M. M. Fejer, X. Yu, J. S. Harris, D. F. Bliss, D. Weyburne, "GaAs optical parametric oscillator with circularly polarized and depolarized pump," Opt. Lett. 32, 2735-2737 (2007).
28. K. L. Vodopyanov, O. Levi, P. S. Kuo, T. J. Pinguet, J. S. Harris, M. M. Fejer, "Optical parametric oscillation in quasi-phase-matched GaAs," Opt. Lett. 29, 1912-1914 (2004).
29. P. G. Schunemann L. a. Poemranz, D. Fayeb, D. J. Magarrell, "Optical parametric oscillation in quasi-phase-matched GaP," Proc of SPIE. 9347, 93470j-1 (2015).

30. R. DeSalvo, A. A. Said, D. J. Hagan, E. W. Van Strylans, M. Sheik-Bahae, "Infrared to Ultraviolet Measurements of Two-Photon Absorption and n_2 in Wide Bandgap Solids," IEEE J. Quantum Electron. 32, 1324-133 (1996).
31. D. N. Nikogosyan, "Nonlinear Optical Crystals: A Complete Survey," (Springer 2005).
32. K. T. Zawilski a,n , P. G. Schunemann , T. C. Pollak , D.E. Zelmon , N. C. Fernelius, F. K. Hopkins, "Growth and characterization of large $CdSiP_2$ single crystals," J. Cryst. Growth. 312, 1127-1132 (2010).
33. S. Chaitanya Kumar, P. G. Schunemann, K. T. Zawilski, M. Ebrahim-Zadeh, "Advances in ultrafast optical parametric sources for the mid-infrared based on $CdSiP_2$," J. Opt. Soc. Am. B 33, D44-D56 (2016).
34. G. Marchev, F. Pirzio, R. Piccoli, A. Agnesi, G. Reali, P. G. Schunemann, K. T. Zawilski, A. Tyazhev, V. Petrov, "Narrow-bandwidth, ~100 ps seeded optical parametric generation in $CdSiP_2$ pumped by Raman-shifted pulses at 1198 nm," Opt. Lett. 38, 3344-3346 (2013).
35. A. C. Lin, "All-eppitaxial orientation-pattered III-V semiconductors for nonlinear optics," PhD dissertation, (Stanford university 2012).
36. A. Grisard, E. Lallier, B. Gérard, "Quasi-phase-matched gallium arsenide for versatile mid-infrared frequency conversion," Opt. Mater. Exp. 2, 1020-1025 (2012).
37. S. Manjooran, H. Zhao, I. T. Lima Jr, A. Major, "Phase-matching properties of PPKTP, MgO:PPSLT and MgO:PPcLN for ultrafast optical parametric oscillation in the visible and near infrared ranges with green pump," Laser. Phys. 22, 1325-1330 (2012).
38. A. Bruner, D. Eger, M. B. Oron, P. Blau, M. Katz, "Temperature-dependent Sellmeier equation for the refractive index of stoichiometric lithium tantalite," Opt. Lett. 28, 194-196 (2003).
39. D. Humm, "Frequency conversion in near-stoichiometric lithium tantalite fabricated by vapour transport equilibration" PhD dissertation, (Stanford university 2007).
40. G. D. Boyd, D. A. Kleiman, "Parametric interaction of focused Gaussian light beams," J. Appl. Phys. 39, 3597-3639 (1968).

41. G. Insero, C. Clivati, D. D'Ambrosio, P. De Natale, G. Santambrogio, P. G. Schunemann, J. J. Zondy, S. Borri, "Continuous-wave difference frequency generation in the mid-infrared with orientation-patterned gallium phosphide (OP-GaP) crystals," Proc of SPIE. 10088, 100880W-1 (2017).
42. V. Tassev, D. Bliss, M. Snure, G. Bryant, R. Peterson, R. Bedford, C. Yapp, W. Goodhue, K. Termkoa, "HVPE growth and characterization of GaP on different substrates and patterned templates for frequency conversion devices," J. Eur. Opt. Soc: Rapid. Publ. 6, 11017 1-7 (2001).
43. R. L. Sutherland, "Handbook of nonlinear optics," (CRS press, 2003).

Chapter 5

High-beam-quality idler-resonant mid-infrared optical parametric oscillator

This chapter constitutes the following publication:

Picosecond idler-resonant mid-infrared optical parametric oscillator based on MgO:PPLN

S. Parsa, S. Chaitanya Kumar, M. Ebrahim-Zadeh

Optics Letters. (2018)-In preparation ……**…**

5.1 Motivation

Coherent mid-infrared (mid-IR) sources with good output beam quality are of great interest for a variety of applications such as remote sensing, telemetry, imaging, and biomedicine [1-4]. One of the most attractive and efficient ways of realizing such sources is frequency conversion through optical parametric oscillators (OPOs), which offers wide tunability, stability, and power scalability. Using OPO sources based on readily available quasi-phase-matched (QPM) nonlinear crystals such as MgO-doped periodically-poled $LiNbO_3$ (MgO:PPLN), MgO-doped stoichiometric periodically-poled $LiTaO_3$ (MgO:sPPLT), and periodically-poled $KTiOPO_4$ (PPKTP), mid-IR spectral coverage up to ~4 μm can be readily achieved, beyond which these materials show strong absorption [5-7]. To extend the wavelength coverage in the mid-IR region beyond 4 μm, nonlinear

optical materials such as $ZnGeP_2$ (ZGP) and orientation-patterned GaAs (OP-GaAs) with broader transparency range have been developed. However, the unavailability of matured pump laser technology near 2 μm prevents the direct pumping of OPOs based on these nonlinear optical materials, since they show strong two-photon absorption below 2 μm [8-10]. Orientation-patterned GaP (OP-GaP), introduced recently, has the advantage of being pumped by well-stablished 1-μm pump lasers, but it still has a developing growth technology [11-14]. An attractive alternative to extend the tunability of mid-IR OPOs is to deploy external cascaded schemes [15,16]. Realizing such a scheme, in which a primary OPO is used as a pump source for another OPO in a cascaded scheme, can provide wider tunability and enables parametric oscillation with other nonlinear optical crystals which can neither be directly pumped nor be phase-matched with conventional 1-μm lasers. Therefore, it is worthwhile to establish a system providing coherent radiation with high beam quality, which can be used either directly for different applications, or as a pump source for a subsequent OPO in tandem to extend the spectral coverage deep into the mid-IR.

To improve the output beam quality in the mid-IR, one can provide resonance for the OPO at the idler wavelength. However, given the high thresholds in such OPOs due to the longer resonating wavelengths [17] and the difficulty in fabrication of highly reflective (HR) dielectric multilayer mirror coatings with high damage threshold in the mid-IR region, realization of such OPOs has been challenging.

Earlier reports on ultrafast idler-resonant OPOs include femtosecond OPO synchronously pumped by Ti:sapphire laser at 106 MHz repetition rate, providing spectral coverage in idler wavelengths from 2.1-4.2 μm by using dual-grating designed MgO:PPLN crystal [18]. In the nanosecond regime, idler-resonant OPO pumped by a Nd:YAG laser operating at 40 KHz based on X-cut birefringent $KTiOAsO_4$ (KTA) crystal has been demonstrated, generating up to 105 mW of average power at 3.46 μm in the mid-IR with M^2 ~1.2 in both horizontal and vertical directions [19]. A nanosecond idler-resonant OPO using MgO-doped periodically-poled congruent $LiNbO_3$ (MgO:PPCLN) crystal is also reported [20]. Pumped by a 1.064-μm laser with an elliptical beam at 104 W, the OPO generated up to 16.7 W average power of mid-IR radiation at 3.84 μm at the repetition

rate of 7 kHz with M^2 to be ~2.03 and ~5.89 in parallel and perpendicular directions, respectively. Recently, an intracavity idler-resonant OPO based on type-II noncritical phase-matched KTA pumped by a dual-loss modulated Q-switched laser is reported, providing 228 mW idler beams at ~3.5 μm [21].

In this chapter, we present what we believe to be the first high-repetition-rate picosecond idler-resonant OPO based on a multi-grating MgO:PPLN crystal tunable across 2.1-4 μm in the mid-IR. Our source generates as much as 1 W of average power at 3.3 μm with passive power stability better than 0.31%rms over 1 hour in good beam quality, with M_x^2~1.1 and M_y^2~1.02. We also investigated the effect of the OPO cavity length detuning on the output power about the zero-crossing point of the intracavtiy group velocity mismatch (GVM).

5.2 Experimental setup

A schematic of the experimental setup together with the laboratory picture of the MgO:PPLN idler-resonant OPO is shown in Fig. 5.1. The pump source is a passively mode-locked picosecond Yb-fiber laser (Fianium, FemtoPower FP1060-20), delivering up to 20 W of average power at ~80 MHz at 1064 nm. The pump pulses are measured to have a duration of 20 ps and a double-peak spectrum with a full-width half-maximum (FWHM) bandwidth of 1.38 nm, resulting in a time-bandwidth product of $\Delta\tau\Delta\vartheta$~7.6. A Faraday isolator at the output end of the fiber protects the laser from any back-reflections. The output power from the laser is adjusted by using a combination of a half-wave plate and a polarizing beam-splitter cube. A second half-wave plate is used to obtain the required polarization for phase-matching during the frequency conversion process in the nonlinear crystal.

The nonlinear crystal used in the present experiments is a 42-mm-long and 1-mm-thick 5%MgO:PPLN crystal (HC Photonics, Taiwan) with seven gratings, ranging in period from Λ=28.5 to 31.5 μm. The crystal faces are antireflection (AR)-coated for idler wavelengths (R<7% over the range of 2.5-4 μm), for pump (R<1%) and for signal wavelengths (R<0.5% over 1.4-2 μm). The nonlinear crystal is housed in an oven with the adjustable temperature from room temperature to 200°C with the stability of ± 0.1°C.

The OPO is formed in a four-mirror standing-wave X-cavity, comprising two concave mirrors (M_1 and M_2, r=150 mm) and a plane mirror, all highly reflecting for idler (R>99.9% over 2.1-4 μm) and highly transmitting for pump (T~92%) and signal (T>80% over 1.3-2 μm). The output idler beam is extracted through a plane output coupler (OC) with variable transmission, while the signal and the undepleted pump are measured after M_2. The total optical length of the OPO cavity is ~3.75 m, which corresponds to a repetition rate of ~80 MHz, ensuring synchronization the resonant idler pulses with the pump laser repetition rate.

In Fig. 5.1(b) is shown the photograph of the laboratory setup of the experiment. Non-phase-matched wavelengths through SFG between the pump and the generated idler, together with SFG of the pump and the corresponding signal in the visible part of the electromagnetic spectrum, confirm the operation of the OPO, as it is clear in Fig. 5.1(b).

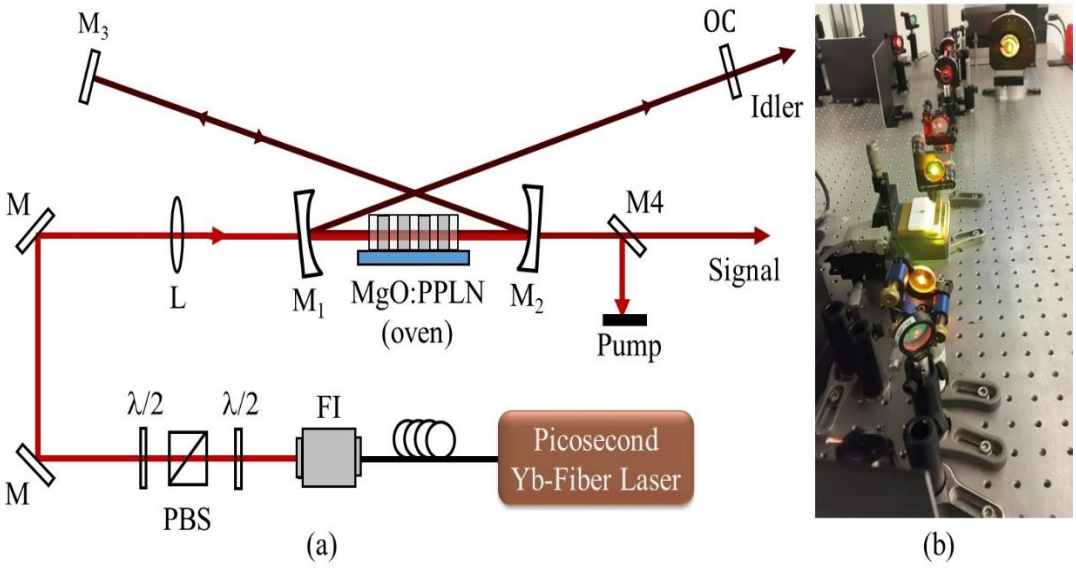

Fig. 5.1. (a) Experimental configuration of the synchronously-pumped idler-resonant OPO. FI, Faraday isolator; λ/2, half-wave plate; PBS, polarizing beam-splitter; L, lens; M, mirror; F, filter; OC, output coupler. (b) Practical X-cavity idler-resonant OPO setup in the lab.

5.3 Design and optimization of the cavity

Considering an unaltered Gaussian idler beam propagating inside the cavity and by using the ABCD transfer matrix analysis [22], we traced the beam waist of the idler wavelength at 3340 nm at different positions inside the standing X-cavity, with the results presented in Fig. 5.2, showing the minimum idler beam radius of ~109 μm.

On the other hand, in order to optimize the performance of the OPO, we used a focusing parameter [23],

$$\xi = \frac{l_{crystal}}{b_P} \tag{5.1}$$

where $l_{crystal}$ is the length of the nonlinear medium, and b_P is the confocal parameter of the pump, defined as

$$b_P = k_P w_{oP}^2 \tag{5.2}$$

with k_p, the pump wave-vector,

$$k_P = \frac{2\pi n_P}{\lambda_P} \tag{5.4}$$

in which n_P is the refractive index of the material at the pump wavelength, λ_P is a wavelength of the pump source, and w_{oP} is the beam waist radius of the pump at the centre of the crystal. In this experiment, by using a 200 mm focal length CaF_2 lens we confocally focused the pump beam to a waist radius of w_{oP}~60 μm, corresponding to a focusing parameter of ξ~0.91 at the centre of the nonlinear crystal. The cavity design ensures optimum overlap of pump and the resonant idler (b_P=b_I), resulting in an idler waist radius of w_{oI}~109 μm at 3340 nm.

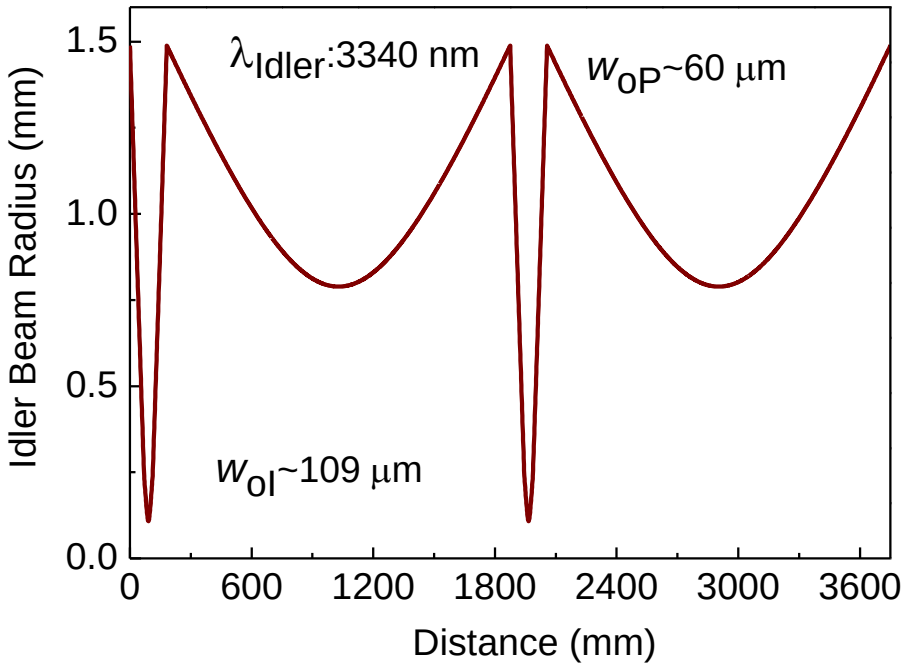

Fig. 5.2. ~80 MHz idler beam radius along the standing wave X-cavity. w_{oP}, and w_{oI} are the minimum waist radius of the pump and the idler beam, respectively.

5.3 Results and discussion

5.3.1 Wavelength tuning

I. Temperature and grating tuning

In order to characterize the idler-resonant OPO, we initially investigated the wavelength tuning performance of the source by changing the temperature as well as the grating periods of the nonlinear optical crystal at low input pump power.

For a fixed grating period of Λ=29 μm, changing the temperature of the MgO:PPLN crystal from 30°C to 200°C resulted in continuously tunable idler wavelengths from 3773 nm to 4028 nm, together the signal beams tunable from 1446 nm to 1481 nm, as it is shown in Fig. 5.3(a). Also presented in Fig. 5.3(a) is the temperature tuning for a grating period of Λ=31.5 μm. In this case, by changing the temperature of the crystal from 30°C to 200°C, the OPO generated idler wavelengths across 2198-2966 nm, with the corresponding signal wavelengths from 1659 nm to 2062 nm.

The grating tuning of the OPO was performed by translating the MgO:PPLN crystal across the pump beam while operating at the fixed temperature. Working at temperature of 40°C, we were able to tune the OPO over 2940-4018 nm in the idler, with the corresponding signal wavelengths across 1447-1668 nm. Also at 200°C, tunable idler wavelengths from 2198 nm to 3772 nm with the corresponding signal wavelengths over 1482-2062 were achieved, as shown in Fig. 5.3(b). In Fig 5.3(a,b), the solid circles are the experimental data, while the dashed curves correspond to the theoretical calculations using the relevant Sellemier equation, presented below [24] , where excellent agreement with the experimental data is evident.

$$n^2(\lambda,T) = a_1 + b_1 f(T) + \frac{a_2 + b_2 f(T)}{\lambda^2 - a_3^2} + \frac{a_4 + b_3 f(T)}{\lambda^2 - a_5^2} - a_6\lambda^2 \qquad (5.5)$$

with the coefficients as below

a_1	5.319725
a_2	0.09147285 (μm^2)
a_3	0.3165008 (μm)
a_4	100.2028 (μm^2)
a_5	11.37639 (μm)
a_6	0.01497046 (μm^{-2})
b_1	4.753469×10^{-7} (^{o}C^{-1})
b_2	3.310965×10^{-8} (μm^2.^{o}C^{-1})
b_3	2.760513×10^{-5} (μm^2.^{o}C^{-1})
f	(T-24.50)×(T+570.82) (^{o}C)

The signal wavelengths were measured using a spectrum analyser with ~0.2 nm resolution, while the idler wavelengths were calculated from energy conservation. Typical idler spectrum at ~3539 nm, together with the corresponding signal spectrum centred at 1521 nm, is shown in Fig. 5.4. The idler spectrum was measured by using a

mid-IR spectrum analyser with a resolution of 2 GHz. The signal and idler spectral bandwidths were measured to be ~0.32 nm and ~1 nm, respectively.

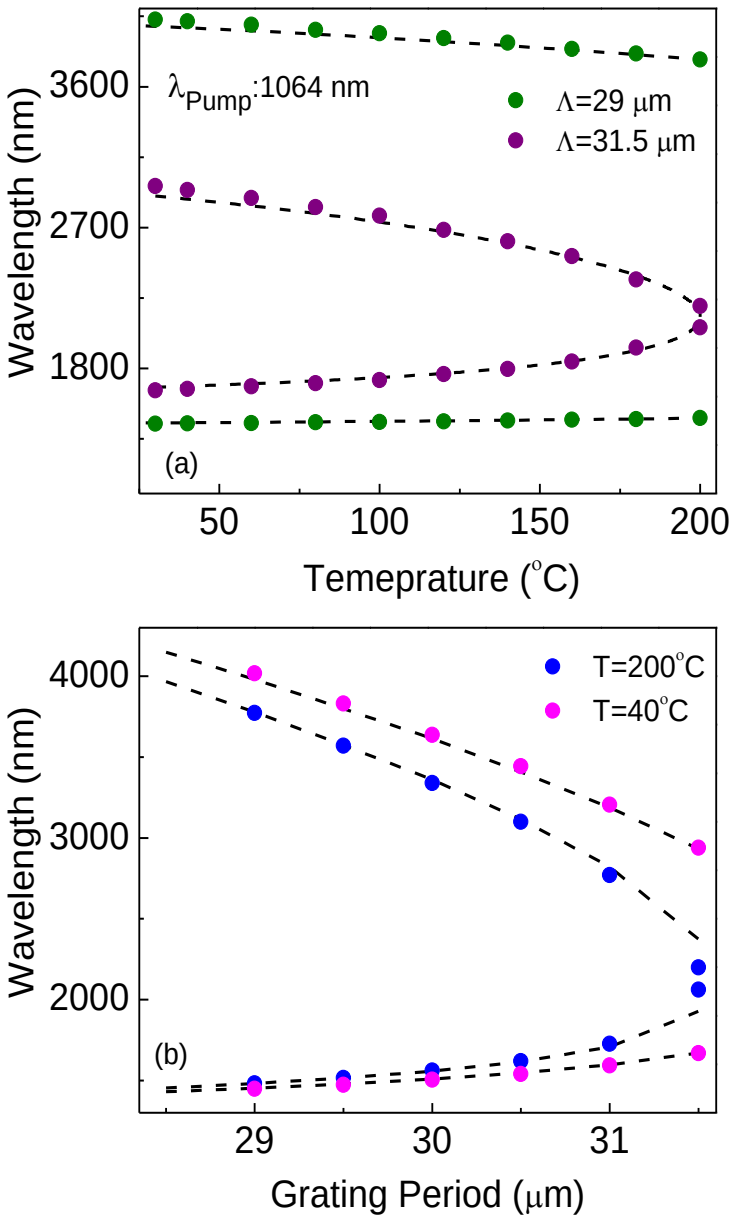

Fig. 5.3. Signal and idler wavelength tuning curves from the MgO:PPLN-based idler-resonant OPO as a function of (a)) temperature for a grating periods of Λ=29 μm and Λ=31.5 μm, and (b) grating period at the temperature of 40°C and 200°C.

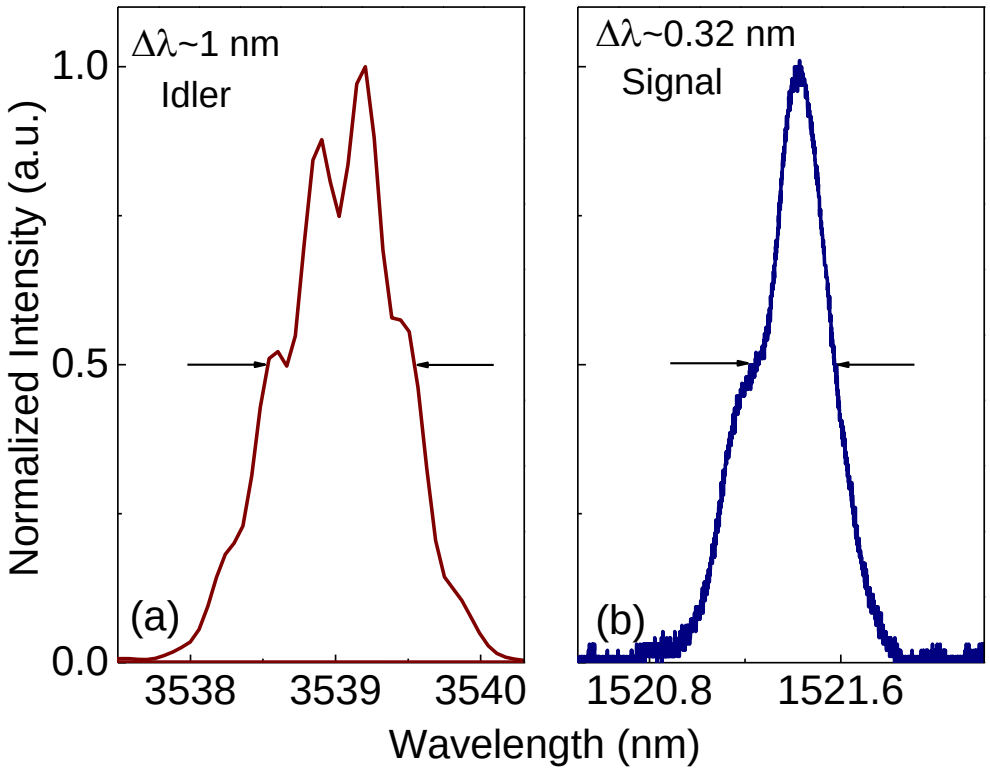

Fig. 5.4. (a) Idler spectrum at 3539 nm, and (b) the corresponding signal spectrum from the picosecond idler-resonant MgO:PPLN OPO.

II. Cavity-length tuning

In addition to the temperature and grating period tuning, we also studied the cavity-length tuning of the OPO at the maximum input pump power. However, the results from our experiment did not show significant wavelength tuning, although the OPO oscillation was maintained over a large cavity-length detuning of ~6 mm. This is attributed to the large intracavity group delay dispersion (GDD)[1] of ~-3.4×10^4±3 fs^2 over 2198-4070 nm for the generated idler inside the 42-mm-long MgO:PPLN crystal, as shown in Fig 5.5(a).

[1] GDD is a variation of group delay with the frequency, which is defined as $GDD = (\lambda^2/2\pi c^2).(d\lambda/dL)^{-1}$ where λ is the central wavelength, c is the speed of light, and $d\lambda/dL$ shows the variation of wavelength with cavity-length detuning.
The tuning rate can be calculated as $d\lambda/dL = -(1/l_{crystal}).(dn/d\lambda)^{-1}$, where *n* is the refractive index of the nonlinear optical medium and $l_{crystal}$ is the crystal length.

It is to be noted that the GVM between the pump and the resonant idler reaches a minimum with zero-GVM-crossing at ~3450 nm, as shown in Fig 5.5(b). Hence, it is interesting to study the effect of cavity-length tuning and thereby the change of GVM sign on the output power on either side of the zero-GVM-crossing point.

The simultaneously recorded signal and idler output power as a function of the cavity-length detuning for the idler wavelength at 3550 nm is shown in Fig. 5.6(a). The idler output coupling in this wavelength range is ~60%. Under perfect synchronization, we extracted as much as 0.78 W of idler and ~4.25 W of signal, corresponding to an overall extraction efficiency of 46%. As the cavity length is adjusted from -2.4 mm to zero detuning, the idler power increases from 0.123 W to a maximum of ~0.77 W at -0.45 mm, after which it remains almost constant over ~3.5 mm of detuning, beyond which it decreases to ~0.189 W at 4.2 mm of detuning. The behaviour of the extracted power with respect to the cavity-length detuning is mainly attributed to the temporal overlap of the resonant beam, which in this case is the idler, and the pump pulses inside the MgO:PPLN crystal, which is essentially determined by the group velocities of the pump and the resonant idler. At the temperature of 100°C, the group velocities of the pump and the idler beam at 3550 nm in the MgO:PPLN crystal are calculated to be v_{gP}~c/2.209 and v_{gI}~c/2.212, respectively, where c is the speed of light. The small difference between the pump and idler group velocities of ~-0.014 ps/mm makes the OPO to be minimally sensitive to cavity-delay tuning, and to show almost a symmetric idler power variation with respect to the zero detuning. This small pump-idler GVM results in a small temporal walk-off of ~0.6 ps between the pump and resonant idler pulses while traveling along the 42-mm-long crystal. The FWHM of the tuning tolerance is ~6 mm, which corresponds to ~40 ps round-trip time delay in the standing X-cavity. A large dispersion of ~3×10^7 fs^2, which is resulted from the resonator mirrors together with the air and the single-pass dispersion contributed by the crystal itself gives an idler wavelength tunability with the small rate of ~0.8 nm/mm, as shown in Fig. 5.6(b), and limits the tuning range from 3548 nm to 3556 nm in the idler corresponding to the signal wavelengths tuning from 1519 to 1520 nm. It is to be noted that the extracted signal power follows the same trend as the idler power with respect to the cavity-length tuning, as obvious from Fig. 5.6(a).

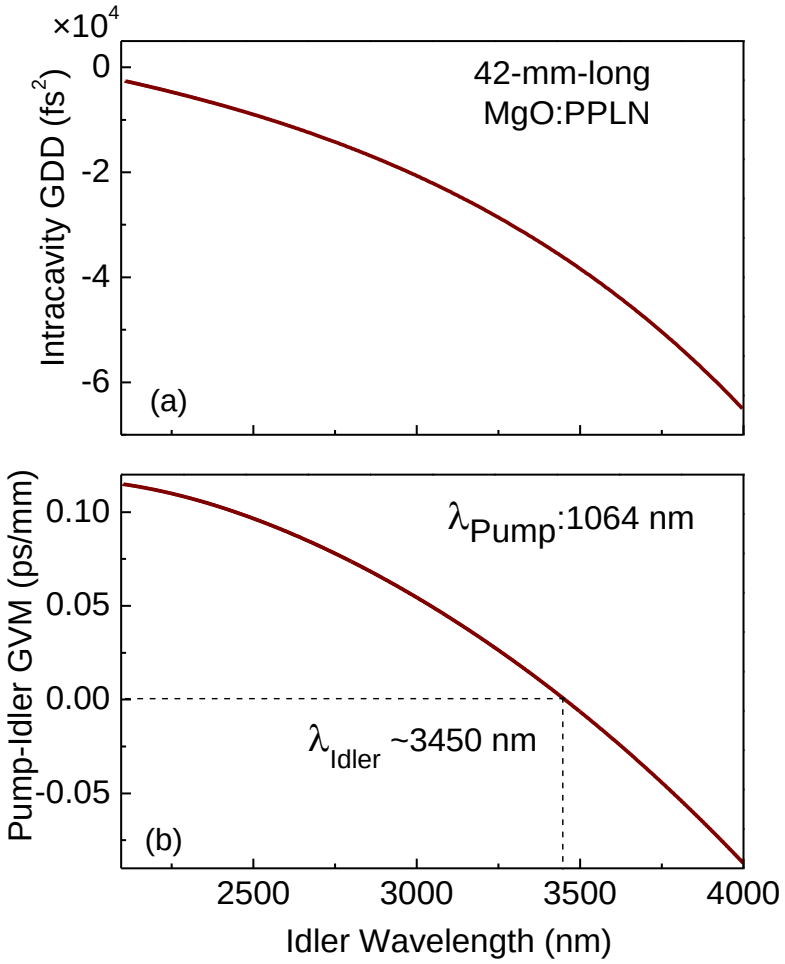

Fig. 5.5. (a) Intracavity group delay dispersion for a 42-mm-long MgO:PPLN crystal, and (b) pump-idler GVM, across the generated idler tuning range.

At the temperature of 40°C, we recorded the idler power together with the variation of the idler wavelengths as a function of cavity-length detuning for the OPO while operating at 3950 nm, with the results shown in Fig. 5.7(a). The calculated GVM between the resonated idler and the pump was ~-0.08 ps/mm resulting in the temporal walk-off to be ~3.36 ps while travelling along the crystal length. As clear from Fig. 5.7(a), the OPO output power varies asymmetrically with respect to the zero detuning and it is more sensitive to the negative detuning, since the pump pulses at 1064 nm travel faster than the idler pulses. The inset of Fig. 5.7(a) shows that the extracted idler wavelength is almost constant across the ~5 mm of detuning, which is related to the large dispersion of ~2.1×10^8 fs^2 resulting in a negligible idler tuning rate of ~ 0.13 nm/mm.

Our study on the cavity-length detuning of the OPO at 100°C while generating idler wavelengths of 3350 nm indicates that for the faster idler wavelengths than the pump pulses, v_{gI}~c/2.203 and v_{gP}~c/2.209, the output power from the source shows more sensitivity towards the positive detuning, as shown in Fig. 5.7(b). A similar behaviour is also observed in a typical signal-resonant MgO:PPLN OPO pumped at 1064 nm, for which pump pulses always travel slower than the signal pulses [25]. This is also the case in green-pumped MgO:sPPLT OPOs [26]. Due to the small temporal walk-off between the pump and the idler of ~0.57 ps, the OPO maintains oscillation over ~7 mm of cavity-length detuning and the large group delay dispersion of ~2×10^7 fs^2 results in a limited tunability of ~7 nm, from 3347 to 3354 nm.

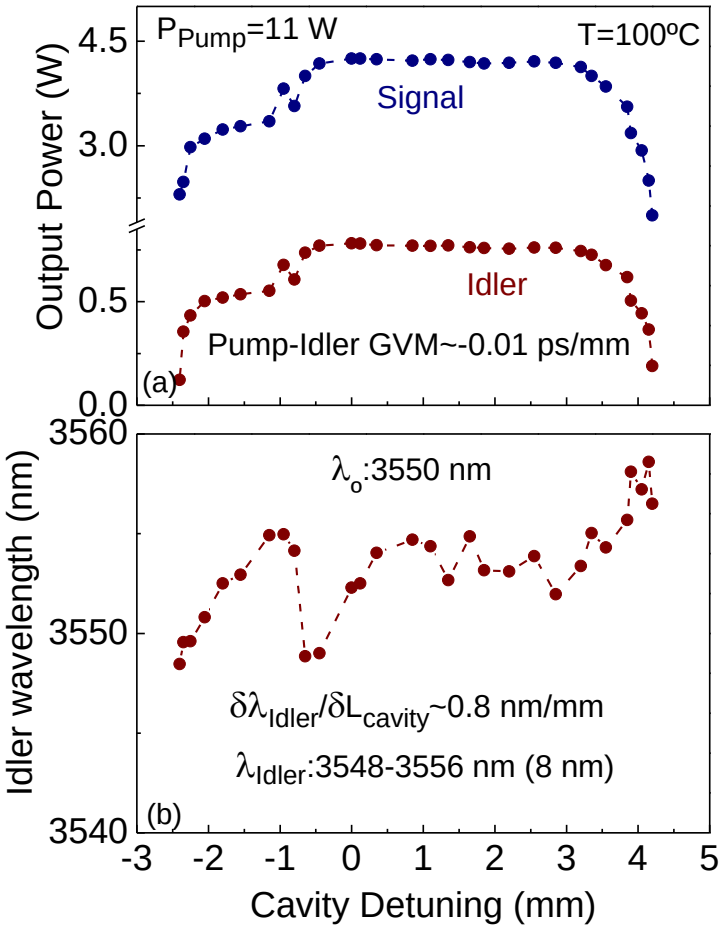

Fig. 5.6. (a) Variation of the signal and idler power, and (b) the extracted idler wavelengths as a function of the cavity-length detuning for the central wavelength of 3550 nm.

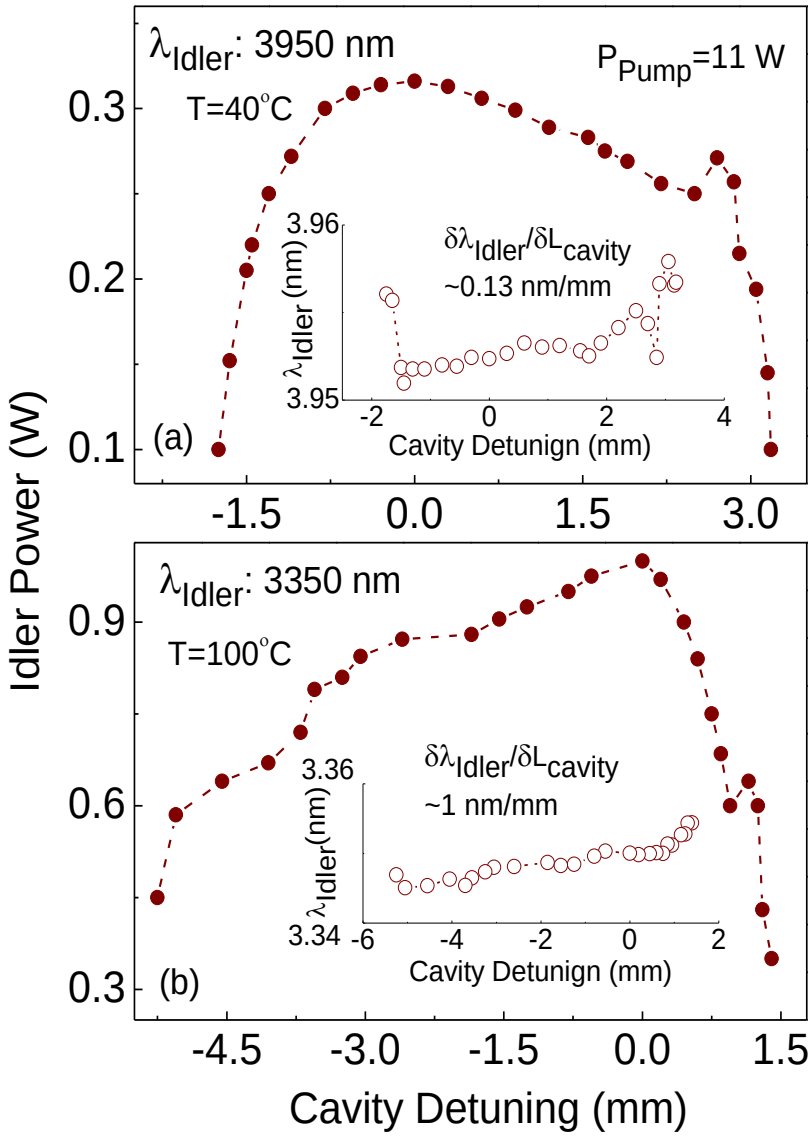

Fig. 5.7. Variation of the extracted idler power at (a) 3950 nm, and (b) 3350 nm as a function of the cavity-length detuning. Inset: idler wavelength tuning at (a) 3950 nm and (b) at 3350 nm with respect to the cavity-length detuning.

As obvious from Figs.5.6 and 5.7, the OPO maintains the operation over a long detuning range of ~6 mm, and in the case of 3550 nm the idler power remains almost constant while the cavity length was detuned for ~4 mm. To the best of our knowledge, this is the first report on detailed investigation on output power sensitivity to cavity-delay detuning about the zero-GVM-crossing point in a synchronously-pumped OPO.

5.3.2 Idler and signal power across the tuning range

We have also characterized the output power of the idler-resonant OPO across the full tuning range by translating the MgO:PPLN crystal across the pump beam and varying its temperature. The simultaneously measured signal and idler average power across the entire tuning range is shown in Fig. 5.8. For a fixed input pump power of ~11 W, we extracted average idler power ranging from 3.5 W at 2198 nm to ~0.3 W at 4028 nm, as shown in Fig. 5.8(a). The OPO provided maximum idler power of 3.5 W at 2198 nm with >0.4 W over almost the entire tuning range, expect for a drop in an idler power around 2800 nm due to the OH-absorption in MgO:PPLN crystal. Also shown in the inset of Fig. 5.8(a) is the transmission of the OC in the idler wavelength range varying from 90% at 2198 nm to 37.8% at 4018 nm. The corresponding signal power varied from 4 W at 1446 nm to ~0.6 W at 2062 nm, with a maximum of 4.3 W at 1561 nm, as shown in Fig. 5.8(b). It is to be noted that the data presented here are not corrected for any AR-coating or transmission losses of the crystal and mirror coatings. Although there is a 7% additional AR-coating loss per round-trip, the extracted idler power still follows the same trend as the OC transmission, which implies that the extracted power can be further improved by minimizing the residual intracavity losses. Further, it also indicates that the high-repetition-rate idler-resonant picosecond OPO is very robust and can afford very high output coupling, and so optimizing the output coupling can improve the performance of the source, similar to that of the signal-resonant configuration [27].

5.3.3 Signal and idler power scaling and power stability

Further, we characterized the OPO by performing power scaling measurements for the extracted idler and signal beams. At a fixed temperature of 200°C and with the grating period of Λ= 30 µm, using the output coupler of 67.4%, we extracted as much as 1 W of average idler power at 3340 nm together with 4.3 W of signal power at 1561 nm, for an input pump power of ~11 W, as shown in Fig. 5.9(a). The threshold for the OPO was measured to be ~5 W and a maximum pump depletion of 63% was recorded. The linear fit to the data results in an estimated slope efficiency of 67.5% and 17.5%, corresponding

to a maximum extraction efficiency of 38.2% and 9.5% for signal and idler beams, respectively.

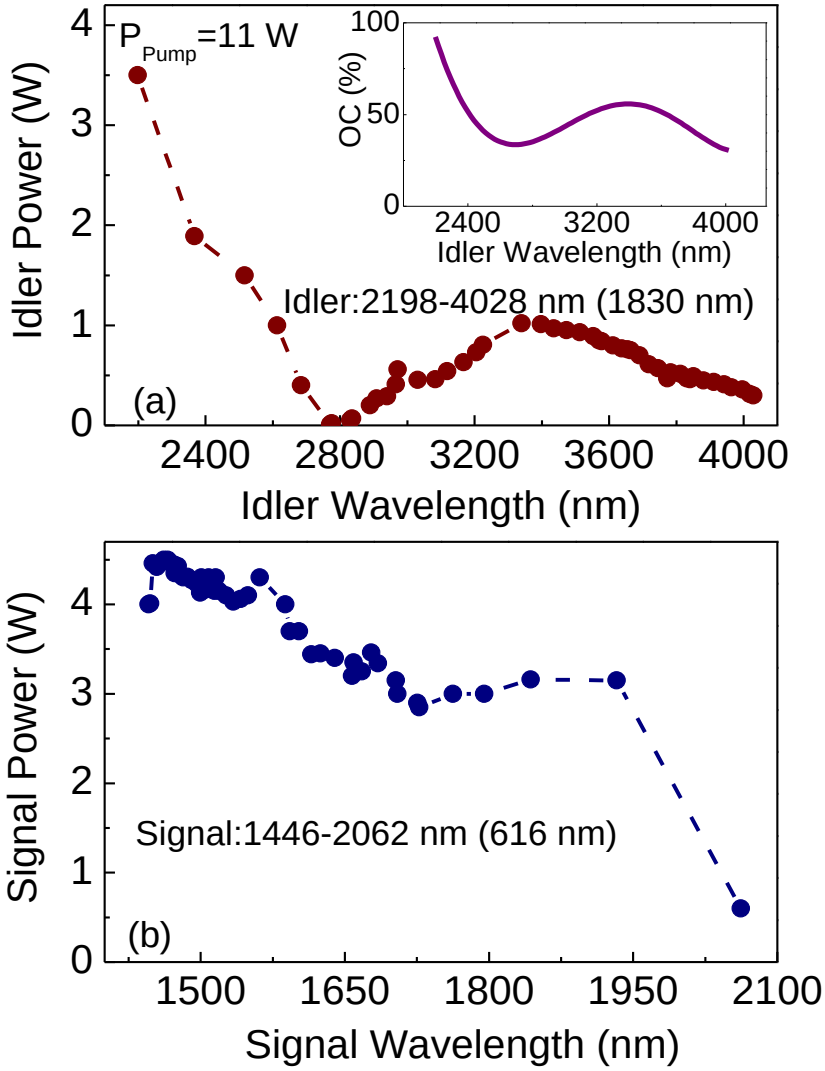

Fig. 5.8. Extracted (a) idler and (b) signal average power across the tuning range. Inset (a) transmission of the OC across the idler wavelength range.

Close to degeneracy, at the wavelength of 2198 nm, we scaled the extracted power from a ~90% output coupler as a function of incoming pump power, with the results shown in the inset of Fig. 5.9(a). The OPO shows the threshold of 4.5 W and produces as much as 3.5 W of average power. Operating close to degeneracy, together with the high nonlinearity of the MgO:PPLN crystal and the long interaction length in combination

with high peak pump power, makes the OPO afford such a high output coupling. The slope and the maximum extraction efficiencies were calculated to be ~55.7% and ~30%, respectively, and a maximum pump depletion of ~60.5% was recorded.

We performed the similar measurement for idler wavelength at 4000 nm. As Fig. 5.9(b) shows, with ~38% output coupling the OPO generated idler average power of 0.344 W together with signal power of 4.2 W at 1450 nm, representing an overall maximum extraction efficiency of ~41.3%. The threshold of the OPO in this case was measured to be ~6 W with a maximum pump depletion of ~63.6%.

Further, we characterized the OPO with regard to output power stability by performing measurements of long-term average power fluctuations with the results shown in Fig. 5.10(a,b). The simultaneously measured long-term passive power stability of the idler (3340 nm) and signal (1561nm) power, recorded over a period of 1 hour while generating maximum output power, is better than 0.31%rms and 0.9%rms, respectively. The same measurement was performed for longer idler wavelength of 4000 nm and the corresponding signal of 1450 nm, showing a good passive power stability better than 0.36%rms for the idler beam and 0.97%rms for the signal. Our investigation on the power stability of the source at 2198 nm, close to degeneracy, shows output power stability better than 0.46%rms over 1 hour, as compared to 0.15%rms pump power stability over the same measurement time.

5.3.4. Output beam quality

In order to study the quality of the extracted beams from the idler-resonant OPO, we have measured the M^2 values of the generated signal and idler beams at maximum output power by scanning a beam profiler (Nanoscan, PHOTON Inc., USA) across the Rayleigh range of the focused beam. As shown in Fig. 5.11(a), the idler wavelength at 3340 nm has M^2 values of 1.1 and 1.02 in the parallel (x) and perpendicular (y) direction with respect to the beam propagation direction inside the crystal, respectively. Such a good beam quality at the idler beam is due to the approximately TEM_{00} Gaussian profile at the pump laser and the good mode-matching between the pump and the resonant idler beam.

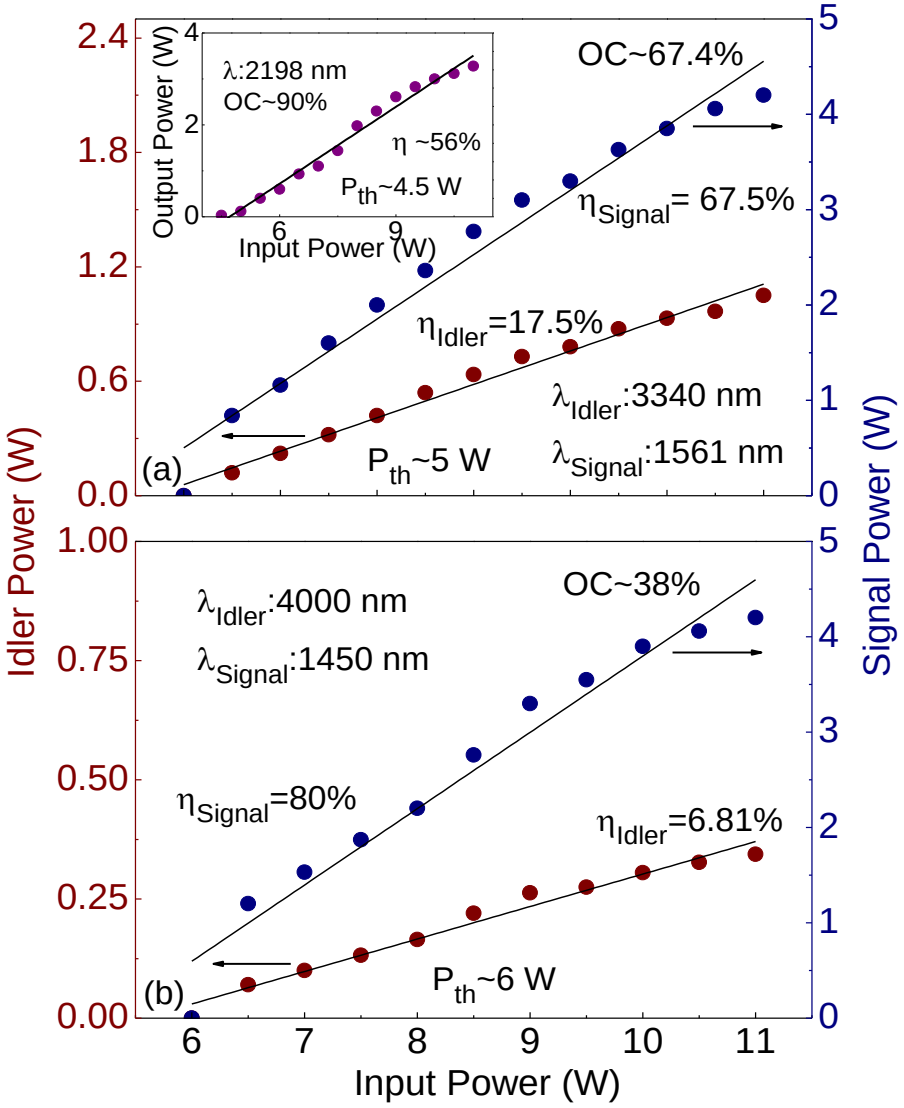

Fig. 5.9. Power scaling measurement at idler wavelengths of (a) 3340 nm, and (b) 4000 nm and their corresponding signal wavelengths. Inset (a) output power scaling at 2198 nm.

The measured M^2 values for the corresponding signal beam at 1561 nm, with the values of 1.02 in the parallel and 1.2 perpendicular directions, are presented in Fig. 5.11(b). The recorded idler and signal beam profiles, which are presented in the inset of Fig. 5.11(a) and (b), respectively, confirm TEM_{00} spatial profiles with single-peak Gaussian distributions at maximum output power.

The results for M^2 measurements of three more idler wavelengths at 2510 nm, 3560 nm, and 4000 nm, together with the corresponding signals, presented in Table 5.1.

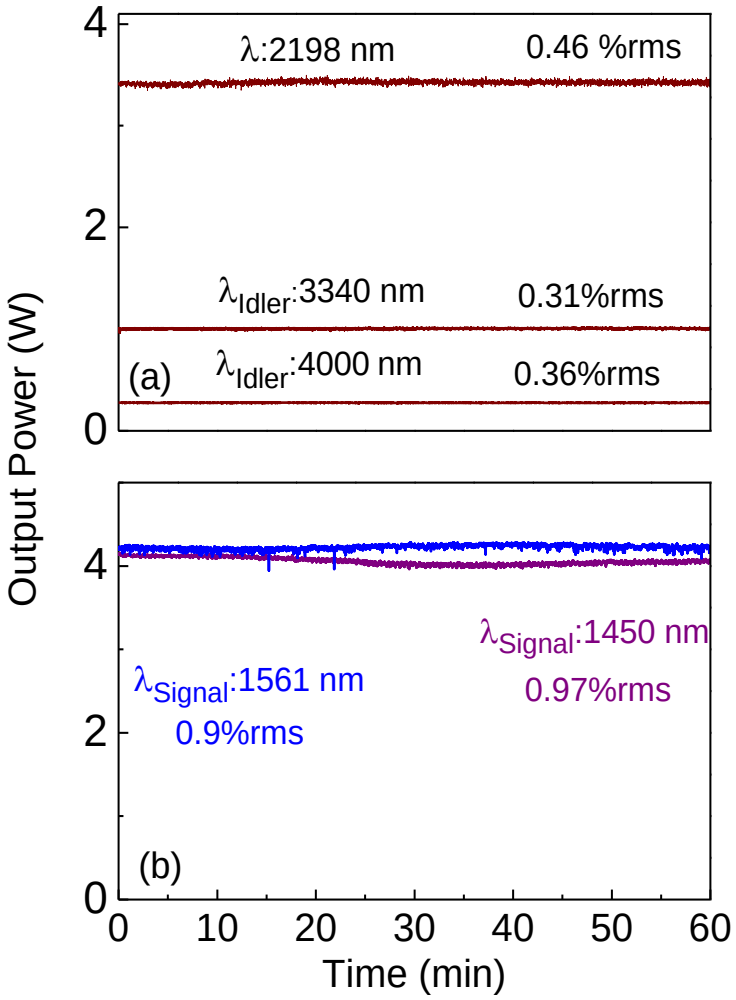

Fig. 5.10. Long-term passive power stability of the (a) extracted idler wavelengths of 2198 nm, 3340 nm, and 4000 nm, and (b) signal wavelengths of 1561 nm, and 1450 nm over 1 hour of measurement.

Since in the present OPO the idler beam is resonating inside the cavity, the idler beam is expected to be more sensitive to small changes in mode-matching with the pump, as well as changes in the cavity stability conditions caused by thermal effects. However, the results from the beam quality measurements together with the output power stability analysis, Fig. 5.10, show that thermal effects, at least up to this level of pumping and at least for 1 hour of operation, do not have significant impact on the performance of the extracted idler beam. These effects are expected to be even less detrimental for the signal beam quality, for it is generated in a single-pass through the crystal as a result of mixing

the single-pass pump and the resonant idler beam. All these confirm that our picosecond idler-resonant OPO is a practical source of emitting high beam quality across the entire tuning range in both signal and idler radiation.

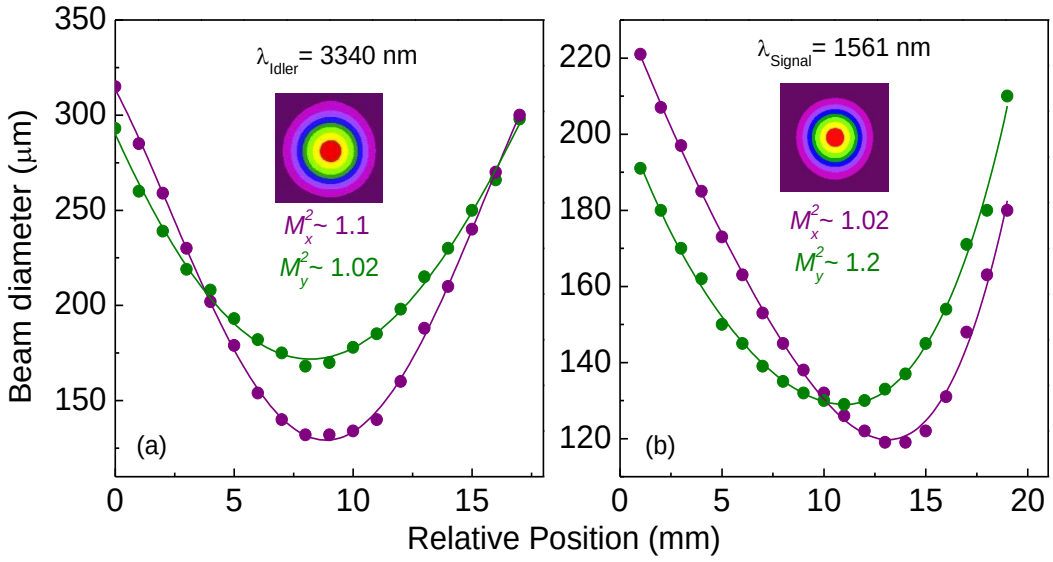

Fig. 5.11. Beam quality measurement for the generated (a) idler at 3340 nm and, (b) the corresponding signal. Inset (a) generated idler, and (b) signal beam profile at maximum output power.

λ_{Idler} (nm)	M_x^2	M_y^2	λ_{Signal} (nm)	M_x^2	M_y^2
2510	1.78	1.38	1849	1.23	1.17
3560	1.13	1.68	1518	1.37	1.34
4000	1.14	1.5	1450	1.2	1.09

Table 5.1. Output beam quality.

5.4. Conclusion

In this chapter, we have demonstrated a stable picosecond idler-resonant OPO at ~80 MHz repetition rate based on MgO:PPLN nonlinear crystal. Pumped at 1064 nm by a Yb-fiber laser, the OPO generates continuously tunable idler wavelengths from 2198-4028 nm with the tunable corresponding signal wavelength across 1446 nm to 2062 nm, by changing the temperature as well as the grating periods of the nonlinear crystal. In our experiment, the tunability of the OPO is only limited by the reflectivity of the mirrors at idler wavelengths and the crystal coatings. We also studied the wavelength tunability of the OPO with respect to the cavity-length detuning. But, a large intracavity GDD, results in a negligible idler wavelength tuning rate of the order ~1nm/mm. The small differences between the pump and the resonant idler group velocities makes the OPO to be minimally sensitive to the cavity-length detuning and to maintain the operation over a long detuning rang of ~6 mm.

Using an output coupler with variable transmission from ~37.8% to ~90% across the extracted idler tuning range, and with the maximum available pump power of ~11 W, the OPO produces >0.4 W of idler average power together with >4 W of signal average power over almost the entire tuning range. It is to be noted that the OC values were not optimized at each wavelength and still higher output powers and better performance from the source across the tuning range are expected.

The OPO generates maximum extracted idler average power of 3.5 W at 2198 nm, close to the degeneracy, showing passive power stability better than 0.46%rms over 1 hour of measurement. Operating at 3044 nm with the output coupler of 67.4%, the source provides as much as 1 W of idler average power together with ~4 W of the corresponding signal radiation at 1561 nm, with overall maximum extracted efficiency of ~45.5%. The extracted idler and signal beams show passive power stability better than 0.31%rms and 0.9%rms, respectively, over 1 hour of measurement compared to ~0.15%rms power stability of the pump over the same measurement time.

Our studies on the extracted idler beam quality prove that our idler-resonant source is capable of generating high-repetition-rate picosecond mid-IR pulses with high beam

quality, as it can generate idler wavelengths at 3340 nm with M^2 values of 1.1 and 1.02 in horizontal and vertical direction, respectively. Also at longer wavelength of 4000 nm, the source provides coherent output beams of high spatial quality as it is confirmed by the measured M^2 values of 1.14 in horizontal and 1.5 in vertical direction.

The results of our experiment confirm that our mid-IR idler-resonant OPO is a robust and reliable source of generating stable high power beam with high beam quality, from which many fields in science and industry, from biomedicine to remote sensing, can benefit. It also can be used as a pump source to pump mid-IR nonlinear optical crystals to extend the wavelength coverage into the deep mid-IR.

References

1. K. L. Vodopyanov, "Pulsed Mid-IR optical parametric oscillators," in Solid-State Mid-Infrared Laser Sources, Topics Appl. Phys, I. T. Sorokina, K. L. Vodopyanov, eds. (Springer, 2003).
2. M. Skorczakowski, J. Swiderski, W. Pichola, P. Nyga, A. Zajac, M. Maciejewska, L. Galecki, J. Kasprzak, S. Gross, A. Heinrich, T. Bragagna, "Mid-infrared Q-switched Er:YAG laser for medical applications," Laser Phys. Lett. 7, 498-504 (2010).
3. A. Godard, M. Raybaut, M. Lefebvre, A. M. Michel, M. Péalat, "Tunable mid-infrared optical parametric oscillator with intracavity parametric amplification based on a dual grating PPLN crystal," Appl. Phys. B 109, 567-571 (2012).
4. K. P. Petrov, L. Goldberg, W. K. Burns, R. F. Curl, F. K. Tittel, "Detection of CO in air by diode-pumped 4.6-μm difference-frequency generation in quasi-phase-matched $LiNbO_3$," Opt. Lett. 21, 86-88 (1996).
5. S. Chaitanya Kumar, M. Ebrahim-Zadeh, "High-power, fiber-laser-pumped, picosecond optical parametric oscillator based on MgO:sPPLT," Opt. Express. 19, 26660-26665 (2011).
6. O. Kokabee, A. Esteban-Martin, M. Ebrahim-Zadeh, "Efficient, high-power, ytterbium-fiber-laser-pumped picosecond optical parametric oscillator," Opt. Lett. 35, 3210-3212 (2010).
7. H. Chu, J. Zhao, T. Li, S. Zhao, K. Yang, D. Li, G. Li, W. Qiao, Y. Sang, H. Liu, "KTP OPO with signal wave at 1630 nm intracavity pumped by an efficient σ-polarized Nd,MgO:$LiNbO_3$ laser," Opt. Mater. Express. 5, 684-689 (2015).
8. B. Q. Yao,Y. J. Shen, X. M. Duan, T. Y. Dai, Y. L. Ju, Y. Z. Wang, "A 41-W $ZnGeP_2$ optical parametric oscillator pumped by a Q-switched Ho:YAG laser," Opt. Lett. 39, 6589-6592 (2014).
9. L. Wang, X. Zhang, H. Xu, "Mid-infrared $ZnGeP_2$ optical parametric oscillator pumped by Tm:$YAIO_3$ laser," Int. J. Nanotech. 12, 802-810 (2015).
10. T. H. Allik, S. Chandra, D. M. Rines, P. G. Schunemann, J. A. Hutchinson, R. Utano, "Tunable 7-12 um optical parametric oscillator using a Cr,Er:YSGG laser to pump CdSe and $ZnGeP_2$ crystals," Opt. Lett. 22, 597-599 (1997).

11. J. Canals Casals, S. Parsa, S. Chaitanya Kumar, K. Devi, P. G. Schunemann, M. Ebrahim-Zadeh, "Picosecond difference-frequency-generation in orientation-patterned gallium phosphide," Opt. Exp. 25, 19595-19602 (2017)
12. J. Wei, S. Chaitanya Kumar, H. Ye, K. Devi, P. G. Schunemann, M. Ebrahim-Zadeh, "Nanosecond difference-frequency generation in orientation-patterned gallium phosphide," Opt. Lett. 42, 2193-2196 (2017).
13. G. Insero, C. Clivati, D. D'Ambrosio, P. Natale, G. Santambrogio, P. G. Schunemann, J. J. Zondy, S. Borri, "Difference frequency generation in the mid-infrared with orientation-patterned gallium phosphide crystals," Opt. Lett. , 41, 5114-5117 (2016).
14. L. Maidment, P. G. Schunemann, D. T. Reid, "Molecular fingerprint-region spectroscopy from 5 to 12 μm using an orientation-patterned gallium phosphide optical parametric oscillator," Opt. Lett. 41, 4261-4264 (2016).
15. L. Wang, T. Xing, S. Hu, X. Wu, H. Wu, J. Wang, H. Jiang, "Mid-infrared ZGP OPO with a high optical-to-optical conversion efficiency of 75.7%," Opt. Exp. 25, 3373-3380 (2017).
16. M. Henrikssona, L.Sjöqvista, G. Strömqvistb, V. Pasiskeviciusb, F. Laurellb, "Tandem PPKTP and ZGP OPO for mid-infrared generation," Proc. of SPIE. 7115, 71150O-1 (2008).
17. S. Brosnan, R. Byer, "Optical Parametric Oscillator Threshold and Linewidth Studies," IEEE J. Quantum Electron, 15, 415-431 (1979).
18. K. A. Tillman, D. T. Reid, D. Artigas, T. Y. Jiang, "Idler-resonant femtosecond tandem optical parametric oscillator tuning from 2.1 μm to 4.2 μm," J. Opt. Soc. Am. B 21, 1551-1558 (2004).
19. F. Bai, Q. Wang, Z. Liu, X. Zang, W. Lan, X. Tao , Y. Sun, "Idler-resonant optical parametric oscillator based on $KTiOAsO_4$," Appl. Opt. B 112, 83-87 (2013).
20. Y. Peng, W. Wang, X. Wei, D. Li, "High-efficiency mid-infrared optical parametric oscillator based on PPMgO:CLN," Opt. Lett. 34, 2897-2899 (2009).
21. J. Qiao, S. Zhao, K. Yang, J. Zhao, G. Li, D. Li, T. Li W. Qiao, "Idler-resonant intracavity KTA-based OPO pumped by a dual-loss modulated-Q-switched-laser with AOM and Cr^{4+} :YAG," Appl. Phys. B 123, 1841-8 (2017).

22. J. T. Verdeyen, "Lasers Electronics," 3rd ed, (Prentice Hall, Englewood Cliffs, New Jersey, 1995).
23. G. D. Boyd, D. A. Kleinman, "Parametric Interaction of Focused Gaussian Light Beams," J. Appl. Phys. 39, 3597-3639 (1968).
24. O. Paul, A. Quaosig, T. Bauer, M. Nittmann, J. Bartschke, G. Anstett, J. A. L'Huillier, "Temperature-dependant Sellmeier equation in the MIR for the extraordinary refractive index of 5% MgO doped congruent $LiNbO_3$," Appl. Phys. B, 86, 111-115 (2007).
25. M. E. Klein, A. Robertson, M. A. Tremont, R. Wallenstein, K. J. Boller,"Rapid infrared wavelength access with a picosecond PPLN OPO synchronously pumped by a mode-locked diode laser," Appl. Phys. B 73, 1-10 (2001).
26. S. Chaitanya Kumar, M. Ebrahim-Zadeh, "Fiber-laser-based green-pumped picosecond MgO:sPPLT optical parametric oscillator," Opt. Lett. 38, 5349-5352 (2013).
27. S. Chaitanya Kumar, A. Esteban-Martin, M. Ebrahim-Zadeh, "Interferometric output coupling of ring optical oscillators," Opt. Lett. 36, 1068-1070 (2011).

Chapter 6

Summary and outlook

In this thesis, we have demonstrated the development of ultrafast singly-resonant optical parametric oscillators (OPOs) and a nonlinear frequency conversion source through single-pass difference-frequency-generation (DFG) process in picosecond time-scale, covering the near- to mid-infrared (IR) spectral regions. An 80-MHz Yb-fiber laser emitting at 1064 nm with a pulse duration of 20 ps has been used as the fundamental pump source for all the presented nonlinear optical devices. We demonstrated two different OPOs based on PPKTP and MgO:PPLN nonlinear crystals, while we used an OP-GaP crystal as a nonlinear optical medium for the DFG process.

The main outcomes of this work include:

- Demonstration of the first picosecond, green-pumped, synchronously-pumped OPO based on a fan-out designed grating period in PPKTP nonlinear crystal. The OPO is continuously tunable across 726-955 nm in the signal and 1201-1998 nm in the idler, resulting in a total signal plus idler wavelength coverage of 1026 nm by grating tuning at a fixed temperature. The device generates up to 580 mW of average power in the signal at 765 nm and 300 mW in the idler at 1338 nm, with an overall extraction efficiency of up to 52% and a pump depletion >76%. The extracted signal at 765 nm and idler at 1746 nm exhibit excellent passive power stability better than 0.5%rms and 0.8%rms, respectively, over 1 hour with good beam quality in a TEM_{00} mode profile. The output signal pulses have a Gaussian

temporal duration of 13.2 ps with a FWHM spectral bandwidth of 3.4 nm at 79.5 MHz repetition rate.

- The first report on successful generation of tunable high-repetition-rate picosecond radiation in the mid-IR region by using a new QPM nonlinear optical material, OP-GaP. The source is realized by using a single-pass DFG between input pump pulses at 1064 nm with the output signal from a MgO:sPPLT picosecond OPO synchronously pumped by the same laser in a 40-mm-long OP-GaP crystal with a single grating period of Λ=16 μm. Using signal wavelengths tunable across 1609-1637 nm, the source is capable of generating tunable radiation across 3040-3132 nm in the mid-IR, with DFG average power up to 57 mW at ~80 MHz repetition rate for a pump power of ~5 W and signal power of ~0.9 W. The power of the generated mid-IR radiation remain >30 mW over >50% of the tuning range and exhibits passive power stability better than 3.2%rms over 1 hour with good spatial beam-quality.

- The successful demonstration of a stable, high-repetition-rate picosecond idler-resonant OPO based on MgO:PPLN crystal with good beam quality. The source is continuously tunable across 1446-2062 nm in the signal and 2189-4028 nm in the idler and can generate >500 mW of idler power over >54% of the tuning range, with more than 4 W of signal power over >60% of the entire tuning range. The extracted idler at 3340 nm exhibits excellent passive power stability better than 0.31%rms, over 1 hour with M_x^2~1.1 and M_y^2~1.02. The corresponding signal wavelength shows TEM_{00} beam profile with M_x^2~1.02 and M_y^2~1.2.

The successful generation of mid-IR radiation through DFG process in the OP-GaP crystal paves the way of better understanding the performance of this new nonlinear crystal in picosecond time-scale when pumped by a 1-μm laser source. As a direction for the future work, the result from the presented experiment can be used to demonstrate the first picosecond high-repetition-rate OPO based on the OP-GaP crystal, with different

grating periods. The theoretical studies in this direction have been performed, already together with the first attempts of implementing such a device.

The reported idler-resonant OPO with high spatial beam quality tunable in the mid-IR can be further used as a pump source for the first picosecond high-repetition-rate OPO based on $ZnGaP_2$ (ZGP) nonlinear crystal in tandem. The basic studies and the theoretical calculations for this experiment have been accomplished. The successful demonstration of such a device will address a very important problem of unavailability of matured pump laser technology for mid-IR OPOs beyond 5 μm, thereby enabling the first demonstration of a broadly tunable mid-IR picosecond OPO based on ZGP, providing spectral coverage from 5.7 μm to 12 μm.